

---

# **Self-assembly, dynamics, and reactions of organic molecules on metal surfaces:**

*A scanning tunneling microscopy study*

---

SIGRID WEIGELT

Interdisciplinary Nanoscience Center (iNANO) and  
Department of Physics and Astronomy  
University of Aarhus, Denmark

**PhD thesis**

July 2007

This thesis has been submitted to the Faculty of Science at the University of Aarhus in order to fulfil the requirements for obtaining a PhD degree in physics. The work has been carried out under the supervision of Professor Flemming Besenbacher and Associate Professor Trolle R. Linderøth at the Interdisciplinary Nanoscience Center (iNANO) and the Department of Physics and Astronomy.

---

# Contents

---

<b>List of Publications</b>	<b>vii</b>
<b>List of abbreviations</b>	<b>ix</b>
<b>1 Introduction</b>	<b>1</b>
1.1 Motivation . . . . .	2
1.2 Outline of the thesis . . . . .	3
1.3 Literature survey . . . . .	4
1.3.1 Molecular self-assembly . . . . .	4
1.3.2 Stereochemistry in adsorption systems . . . . .	6
1.3.3 Chemical reactions on solid surfaces . . . . .	8
1.3.4 Dynamical processes . . . . .	9
<b>2 Methods</b>	<b>13</b>
2.1 Scanning tunneling microscopy . . . . .	14
2.1.1 Theory of STM . . . . .	14
2.1.2 Imaging of adsorbates . . . . .	15
2.1.3 The Aarhus STM . . . . .	17
2.2 Synchrotron studies . . . . .	18
2.2.1 X-ray photoelectron spectroscopy . . . . .	18
2.2.2 X-ray absorption spectroscopy . . . . .	18
2.3 Density functional theory . . . . .	20
2.4 Experiments . . . . .	21
<b>3 Diffusion of azobenzene</b>	<b>23</b>
3.1 Introduction . . . . .	24
3.1.1 Azobenzene . . . . .	24
3.1.2 Methods . . . . .	25
3.1.3 Diffusion in one dimension . . . . .	25
3.2 Adsorption geometries . . . . .	26
3.2.1 Room-temperature deposition . . . . .	26

3.2.2	Low-temperature deposition . . . . .	28
3.3	Diffusion . . . . .	29
3.4	Clustering . . . . .	30
3.5	Discussion . . . . .	30
<b>4</b>	<b>Conformational switching for a class of oligo-phenylene-ethynylenes</b>	<b>33</b>
4.1	Introduction . . . . .	34
4.1.1	The molecular system . . . . .	34
4.1.2	Au(111)-( $22 \times \sqrt{3}$ ) . . . . .	36
4.1.3	Molecular imaging modes . . . . .	37
4.1.4	Data analysis . . . . .	38
4.2	Para-compound . . . . .	39
4.2.1	Brick-wall structure . . . . .	40
	Interactions . . . . .	40
	Chiral switching . . . . .	41
4.2.2	Grid structure . . . . .	45
	Interactions . . . . .	46
	Accommodation . . . . .	47
4.2.3	DFT calculations . . . . .	47
4.2.4	Discussion . . . . .	49
4.3	Meta and threespoke-compound . . . . .	50
4.3.1	Meta-compound . . . . .	50
4.3.2	Threespoke-compound . . . . .	51
4.3.3	Interactions . . . . .	54
4.3.4	Molecular dynamics . . . . .	55
4.4	Conclusion . . . . .	56
<b>5</b>	<b>An upright-standing oligo-phenylene-ethynylene</b>	<b>59</b>
5.1	Introduction . . . . .	60
5.2	Adsorption structures . . . . .	61
5.2.1	Hexagonal structure . . . . .	61
5.2.2	Rhombic structure . . . . .	63
5.3	Adsorption orientation . . . . .	63
5.4	Discussion . . . . .	64
<b>6</b>	<b>Amines on Au(111)</b>	<b>65</b>
6.1	Introduction . . . . .	66
6.1.1	Amine adsorption studies . . . . .	66
6.2	Octylamine . . . . .	67
6.2.1	STM results . . . . .	67
6.2.2	Spectroscopy results . . . . .	71
6.3	Trioctylamine . . . . .	76
6.4	1,6-diaminohexane . . . . .	77
6.5	Summary . . . . .	78



<b>7</b>	<b>Imineformation on Au(111)</b>	<b>79</b>
7.1	Introduction . . . . .	80
7.1.1	Imineformation . . . . .	80
7.1.2	Model systems . . . . .	81
7.2	Para-compound and octylamine . . . . .	82
7.2.1	STM results . . . . .	82
7.2.2	Spectroscopy results . . . . .	85
7.2.3	DFT calculations . . . . .	87
7.2.4	Discussion . . . . .	90
7.3	Threespoke-compound and octylamine . . . . .	90
7.3.1	In-situ reaction . . . . .	91
7.3.2	Ex-situ reaction . . . . .	99
7.3.3	Discussion . . . . .	100
7.4	Conclusion . . . . .	101
<b>8</b>	<b>Polycondensation on Au(111)</b>	<b>103</b>
8.1	Introduction . . . . .	104
8.1.1	Investigation of polymers . . . . .	104
8.1.2	Model system . . . . .	105
8.2	Threespoke-compound and 1,6-diaminohexane . . . . .	106
8.2.1	Bonding pattern . . . . .	106
8.2.2	Connectivity . . . . .	107
8.2.3	Ring and chain formation . . . . .	110
8.2.4	Conclusion . . . . .	113
<b>9</b>	<b>Summary and outlook</b>	<b>115</b>
<b>10</b>	<b>Dansk resumé</b>	<b>119</b>
	<b>Bibliography</b>	<b>123</b>
	<b>Acknowledgements</b>	<b>137</b>



---

## List of Publications

---

- [I] *Azobenzene on Cu(110): Adsorption Site-Dependent Diffusion*, J. A. Miwa, S. Weigelt, H. Gersen, F. Besenbacher, F. Rosei, and T. R. Linderoth, *Journal of the American Chemical Society* **128**, 3164-3165 (2006).
- [II] *Chiral switching by spontaneous conformational change in adsorbed organic molecules*, S. Weigelt, C. Busse, L. Petersen, E. Rauls, B. Hammer, K. V. Gothelf, F. Besenbacher, and T. R. Linderoth, *Nature Materials* **5**, 112-117 (2006).
- [III] *Chiral Ordering and Conformational Dynamics for a Class of Oligo-phenylene-ethynylenes on Au(111)*, C. Busse, S. Weigelt, L. Petersen, A. H. Thomsen, M. Nielsen K. V. Gothelf, E. Lægsgaard, F. Besenbacher, and T. R. Linderoth, *Journal of Physical Chemistry B* **111**, 5850-5860 (2007).
- [IV] *Influence of Molecular Geometry on Adsorption Orientation for Oligo-phenylene-ethynylenes on Au(111)*, S. Weigelt, C. Busse, M. M. Knudsen, K. V. Gothelf, E. Lægsgaard, F. Besenbacher, and T. R. Linderoth, *Journal of Physical Chemistry B*, DOI: 10.1021/jp0751231.
- [V] *Covalent Interlinking of Aldehydes and Amines on Au(111) under Ultrahigh Vacuum Conditions*, S. Weigelt, C. Busse, Ch. Bombis, M. M. Knudsen, K. V. Gothelf, T. Strunskus, C. Wöll, M. Dahlbom, B. Hammer, E. Lægsgaard, F. Besenbacher, and T. R. Linderoth, submitted.
- [VI] *Synthesis of polymeric nanostructures on surfaces imaged by UHV-STM*, S. Weigelt, Ch. Bombis, C. Busse, M. M. Knudsen, K. V. Gothelf, E. Lægsgaard, F. Besenbacher, and T. R. Linderoth, in manuscript.
- [VII] *Formation of dioctylamine and trioctylamine from octylamines on Au(111)*, S. Weigelt, Ch. Bombis, A. K. Tuxen, F. Masini, C. Busse, Ch. Isvoranu, E. Ataman, J. Schnadt, E. Lægsgaard, F. Besenbacher, and T. R. Linderoth, in manuscript.

- [VIII] *A new route to surface self-assembly: synthesis of building blocks from vacuum-deposited precursors*,  
S. Weigelt, Ch. Bombis, C. Busse, M. M. Knudsen, K. V. Gothelf, E. Lægsgaard, F. Besenbacher, and T. R. Linderoth, in manuscript.
- [IX] *Molecular nanostructures formed by a class of oligo-phenylene-ethynylenes with systematic variation of chemical endgroups*,  
Ch. Bombis, S. Weigelt, C. Busse, M. Nørgaard, M. M. Knudsen, K. V. Gothelf, E. Rauls, B. Hammer, E. Lægsgaard, F. Besenbacher, and T. R. Linderoth, in preparation.

---

## List of abbreviations

---

<b>2D</b>	Two dimensional
<b>3D</b>	Three dimensional
<b>CuPc</b>	Copper phthalocyanine
<b>DC</b>	Decacyclene
<b>DFT</b>	Density functional theory
<b>DNA</b>	Desoxyribonucleic acid
<b>DPDI</b>	4,9-diaminoperylene-quinone-3,10-diimine
<b>HtBDC</b>	Hexa- <i>t</i> -butyl-decacyclene
<b>NEXAFS</b>	Near-edge x-ray absorption spectroscopy
<b>ODA</b>	Oxydianiline
<b>OEP</b>	Zinc-octaethylporphyrins
<b>Ortho-molecule</b>	1,2-bis[(5- <i>t</i> -butyl-3-formyl-4-hydroxyphenyl)ethynyl]benzene
<b>Para-molecule</b>	1,4-bis[(5- <i>t</i> -butyl-3-formyl-4-hydroxyphenyl)ethynyl]benzene
<b>PMDA</b>	Pyromellitic dianhydride
<b>PTCDA</b>	Tetracarboxylic dianhydride
<b>PTCDI</b>	Perylene tetracarboxylic diimide
<b>PVBA</b>	4-trans-2-(pyrid-4-yl-vinyl)benzoic acid
<b>SPM</b>	Scanning probe microscopy
<b>STM</b>	Scanning tunneling microscopy
<b>SubPc</b>	Chloro[subphthalocyaninato]boron
<b>TAB</b>	Tetraaminobenzene
<b>Threespoke-molecule</b>	1,3,5-tris[(5- <i>t</i> -butyl-3-formyl-4-hydroxyphenyl)ethynyl]benzene
<b>TMA</b>	Trimesic acid
<b>UHV</b>	Ultrahigh vacuum
<b>UV</b>	Ultra violet
<b>VdW</b>	Van der Waals
<b>XPS</b>	X-ray photoelectron spectroscopy



# CHAPTER 1

---

## Introduction

---

The aim of this introductory chapter is to motivate the work presented in the thesis. First, a general introduction to the field is given. This introduction is followed by a short outline of the topics dealt with in the thesis. At the end of the chapter, a short review of the literature on adsorption of organic molecules with the focus on STM investigations of molecular self-assembly, dynamical processes, chirality and chemical reactions is given.

## 1.1 Motivation

Nanoscience deals with physical, chemical and biological processes at the atomic and molecular length scales (0.1-100 nm), and the ultimate goal of the discipline is to investigate, control and develop new nanomaterials and devices applicable for future nanotechnologies. At the single molecular level the border line between physics and chemistry is diffuse, and nanoscale research thus gains tremendously through interdisciplinary collaborations, which bring both new understanding and challenges to the field.

With the invention of the scanning tunneling microscope (STM) in the early 1980's investigations of surface phenomena at the atomic and sub-molecular level became possible. The major break through was found in 1983 with the atomically resolved images of the silicon(111)-(7 × 7) surface reconstruction obtained with STM in real space [1]. Since then STM has proven invaluable in the investigation and understanding of complex physical, chemical and biological systems at the nanoscale with studies ranging from direct observations of standing electron waves [2], single-molecule conduction measurements [3], capturing of time-resolved diffusion processes [4], investigations of double-stranded DNA [5], to the imaging and manipulation of all the steps in a chemical reaction [6].

A highly-ranked discipline within nanoscience is the study of self-assembly. Self-assembly may be defined as 'the autonomous organization of components into patterns or structures without human intervention' [7]. Nature is the all-scale master of self-assembly with astonishing examples ranging from galaxy formation to protein folding. Insight into self-assembly is therefore essential in order to get a better understanding of the both beautiful and complex world around us. Supramolecular chemists take advantage of molecular self-assembly to go beyond the single molecular bond and create polymolecular structures.

Molecular self-assembly is more specifically defined as the 'spontaneous association of molecules under equilibrium conditions into stable, structurally well-defined aggregates joined by noncovalent bonds' [8], and the basic idea is to synthesize molecular building blocks with predetermined intermolecular binding properties. Assuming that the building blocks are designed properly, the system will form the desired structure by itself upon intermixing of the substituents. If we are to control, and ultimately exploit molecular self-assembly in more detail, we need a higher understanding of intermolecular interactions and molecular dynamical processes. The local resolving powers of STM allows for such detailed investigations, and self-assembly performed on conducting templates has thus been given tremendous interest in the past decades. Among the most significant recent achievements in the field are the formation of highly regular molecular patterns mediated by hydrogen bonding [9] or dipole-dipole interactions [10] as well as demonstrations of chiral recognition [11, 12] and amplification processes [13].

Beside an inherent interest in gaining a more fundamental understanding of molecular recognition processes, the field of template assisted molecular self-assembly has been highly motivated by the urge of designing ever smaller components for the micro-electronic industries [14]. Sofar device miniaturization has been based on "top-down" approaches realized mainly by lithographic techniques. Structures formed by these techniques are however approaching the lower physical size limit [15], and it is therefore



important to investigate new paths to create functional nanodevices on surfaces; otherwise the rate of technological developments seen at present and in the past will decrease dramatically. Functional self-assembled nanostructures on surfaces has, due to the large-scale organization combined with the ability to produce high-density structures in a fast and parallel fashion, consequently been pronounced promising "bottom-up" candidates [16]. Other future applications of self-assembled systems are foreseen in the fields of biocompatibility [17], bio sensors [18], and heterogenous asymmetric catalysis [19].

Since molecular self-assembly is based on noncovalent intermolecular interactions the stabilizing binding energies are low. Self-assembled networks are consequently often unstable even at moderate temperatures. Instability is a decisive disadvantage in e.g. electronic applications since errors will occur over time and cause a wipe out of memory. A path to reduce the instability of the organic networks could rely on covalent reaction between the molecular substituents. In this case truly two-dimensionally covalently interlinked networks will be formed. Despite the high impact such investigations have, however, been very scarce, which is surprising since the field of polymerization in solution has been investigated much more extensively and far longer than the field of supramolecular chemistry. Given the detailed knowledge on polymerization from in-solution chemistry, the synthesis of polymeric networks on metal surfaces could therefore be a great future challenge for surface and nanoscience. Especially new attempts combining supramolecular chemistry and covalent reaction to form ordered covalently interlinked structures might hold tremendous potential [20].

The work presented in this thesis is comprised of several molecular adsorption studies. The main topics covered are self-assembly, diffusion of adsorbates, spontaneous intramolecular conformational changes, chiral recognition, organic reactions between co-adsorbed molecules, and formation of 2D polymeric networks investigated with high-resolution STM under ultrahigh vacuum (UHV) conditions. Some of the STM results are further supported by x-ray photoelectron spectroscopy (XPS), near-edge x-ray absorption spectroscopy (NEXAFS) measurements, and density functional theory (DFT) calculations.

## 1.2 Outline of the thesis

In Chapter 1 the field is motivated, and a short literature survey on molecular adsorption systems is given with focus on self-assembly, stereochemistry, organic reactions, and dynamical processes. A short introduction to the experimental techniques is found in Chapter 2. Chapter 3 treats the adsorption site-dependent diffusion observed for azobenzene molecules on the Cu(110) surface [21]. The topic of both Chapter 4 and 5 is the self-assembly of a family of oligo-phenylene-ethynylenes with different geometries [22–24]. In Chapter 4 the adsorption structures formed by the family members with *para*, *meta* and *threespoke* configurations<sup>1</sup> of the molecular backbone are investigated with focus on chiral effects observed both in the molecular conformation and the

<sup>1</sup>*Para*, *meta*, *ortho*, and *threespoke* refer to the attachment positions of the ethynylene spokes to a central benzene ring.

molecular tiling patterns. The molecules are found to undergo thermally induced conformational changes after adsorption. The kinetics of the conformational switching is investigated by time-resolved STM, and mechanistic insight is obtained from DFT calculations. In Chapter 5 the upright-standing adsorption configuration found for the last family member with an *ortho* configuration is discussed. Chapter 6 deals with the adsorption structures formed by aliphatic amines on Au(111). It is found that trioctylamine is formed on the surface upon thermal activation of octylamine. Chapters 7 and 8 are devoted to imineformation between aldehydes and amines co-adsorbed on the Au(111) surface [24]. As aldehyde reactants, the oligo-phenylene-ethynylenes with either *para* or *threespoke* configuration are used, whereas octylamine or 1, 6-diaminohexane are used as amine linkers. In Chapter 7 it is evidenced that the reaction proceeds by comparison between the STM signature of reaction products formed *in-situ* on the surface and *ex-situ* by conventional in-solution chemistry. Furthermore, the influence of the preparation procedure on the conformation of the products is investigated. Chapter 8 deals with two-dimensional polymeric networks formed by polycondensation. The networks are characterized with focus on connectivity, bonding patterns, and formation of porous or chain-dominated areas.

## 1.3 Literature survey

### 1.3.1 Molecular self-assembly

Molecular self-assembly is the spontaneous association of molecules under equilibrium conditions into stable, structurally well-defined aggregates joined by non-covalent bonds [8]. The aim of the discipline is to construct desired functional nanoarchitectures by the synthesis of molecular building blocks with predetermined intermolecular binding properties [7, 16, 25]. Self-assembly on metal surfaces is of special interest because the confinement in two dimensions reduces the number of possible interaction motifs, and the local probe character of the STM allows for real space investigations of the assembled networks. The formation of surface structures is central to future nanotechnology and is foreseen to have applications in areas such as surface functionalization [17], biosensors [18], molecular electronics [26], and heterogeneous asymmetric catalysis [19].

The outcome of a molecular self-assembly process on a metal surface depends in general on both the molecule-molecule and the molecule-substrate interactions. In order to design and form desired supramolecular structures<sup>2</sup> a better understanding of the interactions underlying self-assembly is required, and a broad range of self-assembled systems of increasing size and complexity have therefore been investigated over the past years, some of which will be discussed here.

In general, planar aromatic molecules tend to adsorb flat-lying due to a strong interaction between the aromatic  $\pi$ -system and the underlying metal surface and are therefore widely used in the investigation of intermolecular interactions [16, 27]. If the interaction to the surface is strong, the mobility of the adsorbed molecules can be reduced and the

---

<sup>2</sup>Supramolecular chemistry is the study of structures mediated by non-covalent interactions.

growth of well-ordered structures can be hindered. This was observed for 4-trans-2-(pyrid-4yl-vinyl) benzoic acid (PVBA) that formed well-ordered structures most easily on inert surfaces [28–30].

Molecules that contain a functional group with a high surface affinity are often found to adopt upright-standing adsorption configurations. In those cases a denser packing of the molecular backbones allows for a higher density of interacting affinity groups, which compensates for the loss in backbone-surface interactions. Examples thereof are thiols known to form self-assembled monolayers on the Au(111) surface [31, 32], pyridines on Cu(110) [33], and deprotonated carboxylic acids, such as trimesic acid (TMA) on Cu(100) [34].

To control the outcome of a self-assembly process it is important to synthesize molecular building blocks with functional groups that direct the formation of the desired architecture [10]. An often applied pathway is to implement functional groups designed to form strong, directional intermolecular hydrogen bonds. Simple mono-component systems have been studied extensively. Among the abundant examples are chiral twin-lines formed by PVBA on Ag(111) [29] or phenylglycine on Cu(110) [35], honeycomb patterns assembled by either TMA on Cu(100) [34], 4, 9-diaminoperylene-quinone-3, 10-diimine (DPDI) on Cu(111) [36] or anthraquinone on Cu(111) [37] and the quartet structure formed by the natural occurring DNA base guanine on Au(111) [38]. In the latter case, a cooperative resonance effect within the quartets was shown to strengthen the hydrogen bonded system further.

Heteromolecular hydrogen bonded systems often take advantage of donor-acceptor interactions to gain a strong intermolecular binding. Examples thereof are the intermixed phase of melamine with perylene tetracarboxylic di-imide (PTCDI) [9] and tetracarboxylic dianhydride (PTCDA) with tetraaminobenzene (TAB) [39] on the Ag/Si(111)- $\sqrt{3} \times \sqrt{3}R30^\circ$ . New attempts use biological cognitive interactions such as the DNA-base pairing [40] to direct the assembly process.

Besides hydrogen bonding, dipole-dipole interactions and Van der Waals forces have been applied to direct the ordering of organic molecules. Here a prominent systematic study demonstrated that dipole-dipole interactions between cyano-functionalized porphyrin molecules adsorbed on Au(111) can be used to guide the assembly process [10]. Van der Waals forces are in general less directional, and the resulting patterns depend consequently often on factors such as molecular geometry [41] or stoichiometry [42], as observed in the self-intermixed structures consisting of subphthalocyanine and  $C_{60}$  on Ag(111) [42]. Furthermore, molecules interacting via Van der Waals interactions are often found to close-pack [41–43] and form a number of competing (meta-stable) molecular phases deviating only slightly in energy [44, 45]. In this thesis a class of oligo-phenylene-ethynylenes with varying geometry is investigated. Some of the members are observed to form a number of co-existing structural domains on the Au(111) surface [22, 23].

Recently, metal-ligand complexation has been applied to form more strongly bound self-assembled structures on surfaces. Different metal-organic networks have been demonstrated such as rectangular grids [46], template directed chains [47], and honeycomb structures [48]. In the studies it has often been found that the formed architectures depend on the ratio between molecules and metal ions [46, 49]. In some instances metal-

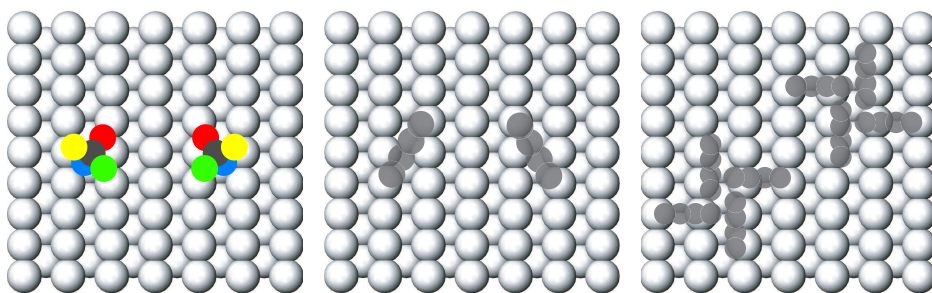


Figure 1.1: Adsorption induced chiral motifs.

organic complexes were observed to form between organic adsorbates and free surface ad-atoms, as was the case for, e.g. TMA on the Cu(110) surface [47].

### 1.3.2 Stereochemistry in adsorption systems

Stereochemistry is the branch of chemistry concerned with the spatial geometry of molecules, and stereochemical effects have consequently high impact on self-assembly processes. In general, any structure which does not contain a mirror plane of symmetry is said to be chiral<sup>3</sup>. A molecule which contains a carbon atom carrying four different groups is non-superimposable on its mirror-image and is therefore chiral. Chiral structures can exist in two mirroring forms, called enantiomers. In contrast, achiral structures contain a mirror plane and are thus superimposable on their mirror images. An achiral molecule is often referred to as a meso-compound.

In nature many chiral molecules, such as amino acids, are only present as single enantiomers. Many life processes are consequently enantioselective, implying that living systems often respond positively to only one chiral form of a curing pharmaceutical [50]. Since most synthetic compounds are formed as racemic mixtures<sup>4</sup>, large effort is spent on separation of enantiomers. Tremendous interest is therefore given to the understanding of chiral recognition processes. Specifically, enantioselective synthetic pathways have been studied widely among which chiral catalysis [51, 52] is expected to hold particular potential. To follow this goal and perhaps even get a more fundamental understanding of the symmetry break observed in nature, increasing attention has been given to molecular adsorption systems displaying stereochemical effects [27, 53].

If a chiral molecule is deposited onto a surface, the chirality of the adsorbate is transferred to the adsorption system provided the chiral center of the molecule stays intact upon adsorption. STM has been widely used to identify and investigate molecular chirality in several such cases, including simple hydrocarbons [54–56], amino-acids [12, 35, 57, 58], tartaric acid [59–61], and twisted molecules such as rubrene [62] and heptahelicene [13].

<sup>3</sup>The term "chiral" stems from the greek word for hands.

<sup>4</sup>A racemix mixture is a 50 to 50 mixture of the two chiral enantiomers.

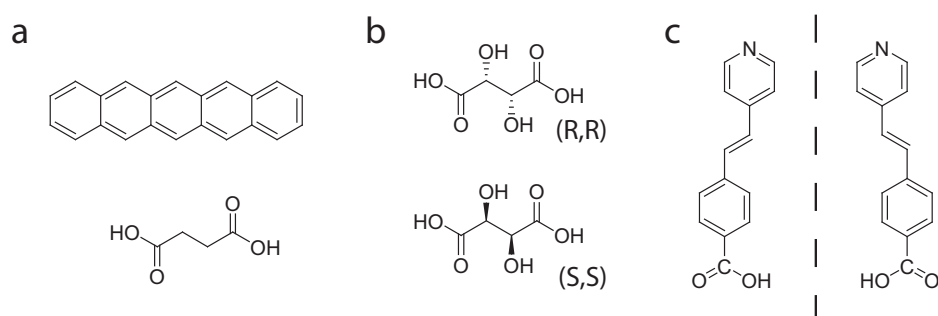


Figure 1.2: Chirality of molecules (a) The achiral molecules pentacene and succinic acid. (b) The chiral enantiomers of tartaric acid. (c) The prochiral molecule PVBA.

Surface chirality can arise even for highly symmetric adsorbates, provided they adsorb in such a way that the molecule-surface system in combination does not have any mirror symmetry elements. In the simplest case this is realized if the molecules adsorb so that the molecular reflection planes do not align with the surface mirror planes. This has been observed in an extended number of systems [63] with succinic acid on Cu(110) [61] being a prominent example. Another possibility is organizational chirality where the mutual arrangement of the molecules destroys the reflection symmetry planes of the underlying substrate. Among the abundant examples are alkylated phthalocyanines and porphyrins [64] and the intermixed structure of  $C_{60}$  and chloro[subphthalocyaninato]boron (SubPc) [42].

Another type of adsorption-induced chirality occurs for molecules that are achiral in the gas phase, but become chiral once adsorbed because the confinement in two dimensions removes the mirror symmetry in the plane of the substrate. Such compounds are said to be prochiral, and their adsorption will always lead to equal amounts of mirror-image surface enantiomers. Important examples of prochiral molecules are 1-nitronaphthalene [65, 66], methyl pyruvate [67], naphtho[2,3-a]pyrene [68], PVBA [11], and adenine [35].

Chiral recognition [35, 54, 69] is an often observed phenomenon in molecular adsorption structures. Both chiral and prochiral molecules often display phase-separation into homo-chiral domains [68, 70–72], and several homo-chiral motifs such as molecular wires [11, 35, 57, 73], molecular rings [62] and nanoclusters [74] have been observed. Domains formed by opposite enantiomers are in these cases mirror-images of each other. This implies that if the tiling pattern of such structures displays organizational chirality, it will correlate with the chiral form of the embedded molecules. In some cases, racemic domains [66, 75, 76] or hetero-chiral structures with an enantiomeric excess [65, 66] are observed. These structures often display organizational chirality [13, 65, 66, 76]. The chiral recognition observed in all these studies is based on directional forces, such as molecule-surface interactions, dipole-dipole interactions, or hydrogen bonding.

Chiral amplification has recently been demonstrated in molecular adsorption systems. By applying the "sergeant and soldier" principle, homochiral domains of succinic

acid were globally induced by seeding with small amounts of either (S,S)- or (R,R)-tartaric acid [61]. Similarly, deposition of heptahelicene in just a small enantiomeric excess has been demonstrated to cause global organizational symmetry breakage [13].

It has in general been believed that the confinement on the surface is sufficiently strong to render the chiral sense of an individual prochiral molecule irreversibly fixed upon adsorption. Phase separation has therefore been ascribed to lateral mass transport in combination with chiral recognition at domain boundaries [11]. In this thesis it will be shown that a family of prochiral molecules can switch between the chiral and achiral forms. Such chiral switching allows accommodating molecules to dynamically adjust their chiral form to the surroundings [22, 23, 77].

### 1.3.3 Chemical reactions on solid surfaces

Beside self-assembly another pathway for the design of two-dimensional molecular nanostructures takes advantage of polymerization of adsorbed organic molecules. In this case the molecules are linked together via covalent bonds. In contrast to self-assembly the formation of covalently bound polymeric structures has primarily been a discipline for conventional in-solution chemistry [78], and studies into the creation of truly two-dimensional surface structures by covalent synthesis between large adsorbed organic molecules directly on surfaces under UHV conditions have been very scarce [79].

The major differences between on-surface and in-solution chemistry are the confinement of the molecules in two dimensions, the absence of a solution phase, the presence of a conducting substrate near the reactants, the packing of molecular islands and the topography of the underlying surface. These conditions seem to influence the reaction outcome, and in several instances compounds anticipated to react under normal solution conditions have been shown to form non-covalently bound structures instead. On the Cu(111) surface chemical dissociation of *p*-diodobenzene resulted in the formation of protopolyphenylene chains that were not covalently bound, but instead held together by molecule-molecule and surface mediated interactions [80]. Formation of porous networks stabilized by strong hydrogen bonds instead of expected covalent bonds was observed for DPDI, which upon thermal activation underwent a dehydrogenation process on the Cu(111) surface [36]. PTCDA and TAB were found to form an intermixed structure on the Ag/Si(111)- $\sqrt{3} \times \sqrt{3}R30^\circ$  which instead of expected covalent imide bonds was mediated by hydrogen bonding [39]. On the contrary, thin organic polyimine- and polyimide-films synthesized by vapour deposition polymerization in the multilayer regime have been studied extensively [81–84].

At the other extreme unwanted surface catalyzed reactions have been observed. It was found that pure methyl pyruvate poisons the catalyzing Pt(111) surface with organic oligomers formed by self-condensation on the surface [67, 85].

At the single-molecule level chemical reactions have been induced in UHV with electrons from the STM tip. These investigations range from dissociation of single  $O_2$  molecules on Pt(111) [86] and chlorobenzene on Si(111)- $7 \times 7$  [87] over oxidation of  $CO$  to  $CO_2$  on Ag(110) [88] to the complete synthesis of biphenyl out of iodobenzene on Cu(111) [6] and the formation of  $CH_3S$  chains from  $(CH_3S)_2$  molecules adsorbed on Cu(111) [89].

A model system for forming polymerized chains on a surface is the mono-component chain polymerization of diacetylene [90]. Prior to reaction the diacetylene molecules are preorganized into a self-assembled monolayer, and the polymerization is subsequently induced by UV light [79, 91–93] or electrons from the STM tip [92, 94–96], resulting in covalent bond formation by an electron redistribution. Polymerization of diacetylene on solid surfaces has been investigated under both UHV [79, 93], ambient [92, 94–96], and liquid conditions [91]. Since molecular preorganization is required, the reaction is referred to as topochemically controlled [90]. Recently, polydiacetylene chains have been investigated as model systems for molecular wires [97, 98].

Studies of other topochemical reactions exist, such as the photodimerization of cinnamate derivatives [99] and the electron- or light-induced polymerization of fullerenes adsorbed on different substrates [100–102]. Besides the studies of photo- or electron-induced topochemical reactions, high interest has been given to the formation and investigation of single isolated conducting homo- and heteropolythiophene wires synthesized by the technique of electrochemical epitaxial polymerization performed at the liquid-solid interface [103, 104].

In this thesis a two-component condensation reaction is demonstrated by which aldehydes and amines are interlinked covalently after co-adsorption in the sub-monolayer regime on the inert Au(111) surface under UHV conditions. Sub-molecular resolution STM reveals both the conformation of monomeric reaction products and the bonding pattern of porous two-dimensional (2D) polymeric networks. Covalent interlinking of the reactants is confirmed by comparison to the STM signature of the reaction product formed ex-situ as well as by near-edge x-ray absorption spectroscopy (NEXAFS), and a solvent-free reaction path is proposed based on ab-initio Density Functional Theory calculations.

### 1.3.4 Dynamical processes

Dynamical phenomena [16, 26] such as rotations [105, 106], diffusion [107], and conformational changes [77] are crucial in the growth and nucleation processes of molecular structures on solid surfaces. Controlling the kinetics and thermodynamics of a system can lead to avoidance of by-products, control of size and shape, and even trapping of desired metastable structures. Rotational and conformational degrees of freedom are especially important in chemical reactions where geometric constraints can hinder the required collisions between the reactive groups. Extensive observations of dynamical processes underlying island growth [108] and surface reactivity have been reported in the past.

To a good approximation most dynamical processes can be described by the reaction rate theories conventionally used for chemical reactions. Transition state theory predicts [109] that such rates follow an Arrhenius [110] dependence,  $\Gamma = \nu_o \exp(-\frac{E_a}{k_B T})$ , given by the temperature,  $T$ , the activation energy,  $E_a$ , Boltzmanns constant,  $k_B$ , and an entropy dependent prefactor  $\nu_o = \frac{k_B T}{h} e^{\Delta S/k_B}$ .

Using time-resolved STM, the rates for dynamical events can be measured at the single molecule level. If such rate measurements are performed at different temperatures, the activation energy and prefactor can be determined by an Arrhenius plot. The



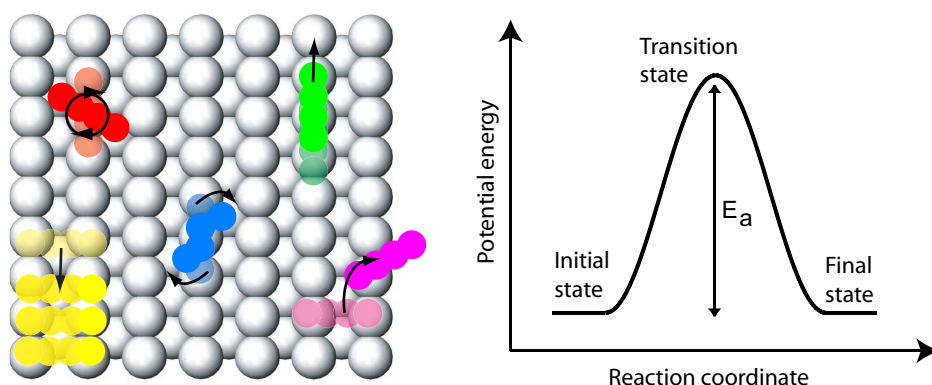


Figure 1.3: Dynamical processes: Growth (yellow), diffusion (green), desorption (purple), rotations (red), and conformational changes (blue). The graph indicates a reaction profile for a process with similar initial and final states.

Aarhus SPM group has a long tradition for that type of investigations performed by fast-scanning STM, with studies ranging from diffusion of single adatoms [111] or metal clusters [112] to large organic molecules [113, 114]. This survey will focus on STM investigations of dynamical processes observed for large organic molecules.

In principle any investigation of self-organization on surfaces is a growth study [9, 10]. However, studies exist that focus more directly on the growth mechanism. Important examples thereof are the investigations of the molecule exchange between the lattice gas and the condensed molecular aggregates [115, 116] and the build-up of molecule-metal complexes [49].

Diffusion of molecules is by far the dynamical process studied in most detail. Among the early studies of diffusion of larger molecules investigated with time-resolved STM are acetylene on Pd(111) [117] and Cu(001) [106], PVBA on Pd(110) [118],  $C_{60}$  on Pd(110) [119], and the similar large aromatic molecules decacyclene (DC) and hexa-*tert*-butyl decacyclene (HtBDC) on Cu(110) [113]. It was demonstrated [113] that long jumps are important in the diffusion of DC and HtBDC and that a reduction in the molecule-surface interaction caused by six *tert*-butyl groups lifting HtBDC from the surface compared to DC leads to a significant increase in the diffusion constant<sup>5</sup>. Recently, more complex systems have been studied such as the lock-and-key effect for the violet lander on Cu(110) [114] and the wheel-like directional rolling motion for single molecule nanocars [120]. In this thesis the adsorption-site dependent diffusion of azobenzene Cu(110) will be discussed [21].

In contrast to diffusion only a few quantitative investigations of thermally activated molecular rotations exist [121]. In an early study the rotation and diffusion of single acetylene molecules on Cu(001) [106] was determined, and very recently, the rotation of large molecules trapped in molecular networks has been investigated for copper phthalate-

<sup>5</sup>The diffusion constant,  $D = \langle (\Delta x)^2 \rangle / 2t$ , is often used to describe diffusion processes.



cyanine (CuPc) trapped in the pores of a  $C_{60}$  network on Au(111) [122, 123] and zinc-octaethylporphyrins (OEP) trapped in the pores of DPDI networks on Cu(111) [124]. Rotations induced by the field or electrons from the STM tip have been given more attention [114, 125]. A pioneering study showed that the vibrational modes coupled with the hindered rotation of acetylene on Cu(100) [126]. Recently, a STM-tip induced "rack-and-pinion" rotational motion of a molecular wheel along an island edge was demonstrated [127].

Intramolecular conformational degrees of freedom are also of high importance in self-assembly processes. Previous studies herein have however mainly focused on the identification [128, 129] or STM-tip induced manipulation [130–136] of the molecular conformation with a recent example demonstrating that intramolecular rotations can drive a molecular wheel at the nanoscale [136]. In contrast, only minor focus has been on elucidating the dynamics of spontaneous conformational changes [120, 137, 138]. In this thesis thermal induced conformational changes will be investigated dynamically by time-resolved STM [22, 23].



## CHAPTER 2

---

### Methods

---

In this chapter the experimental and theoretical methods underlying the work presented in this thesis are introduced. The emphasis is placed on scanning tunneling microscopy, whereas the supplementary methods x-ray photoemission spectroscopy, x-ray adsorption spectroscopy, and density functional theory calculations are only touched upon. In addition a short introduction to the experimental setup and sample preparation will be given.

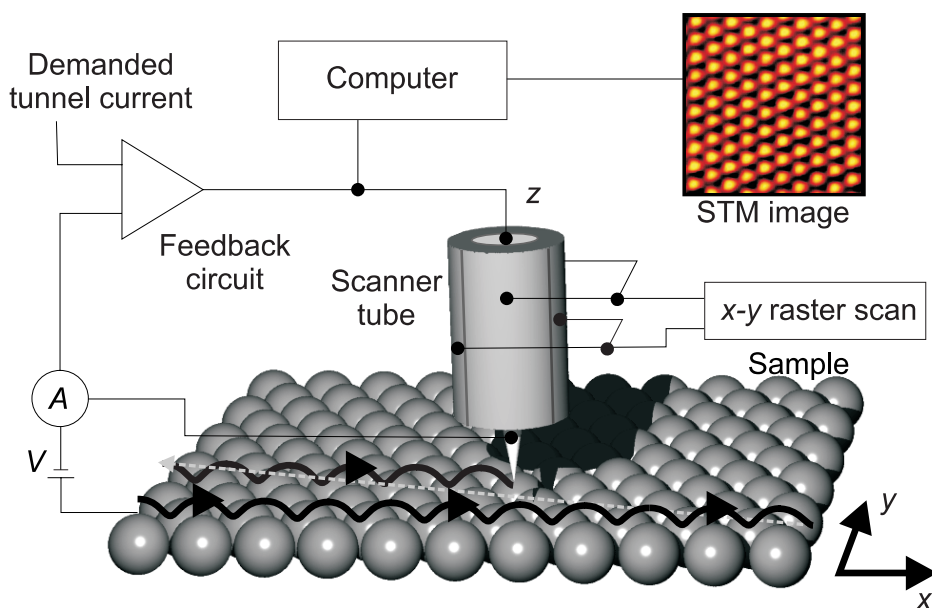


Figure 2.1: Principle behind STM

## 2.1 Scanning tunneling microscopy

The scanning tunneling microscope (STM) invented in 1982 by Binnig and Rohrer [139] has proven a powerful local surface science technique [140, 141]. It relies on the basic principle of controlled quantum mechanical electron tunneling between a metal tip and a conducting surface placed in close proximity. At distances of  $5-50\text{\AA}$  the wave functions of the tip and surface overlap sufficiently to allow the flow of a distance dependent tunneling current if a bias voltage is applied.

The basic operation principle is sketched in Fig. 2.1. Topographic images are acquired by raster-scanning the STM tip laterally over the conducting substrate while measuring the tunnel current. Image acquisition with atomic resolution is normally realized by mounting the STM on a piezo electric ceramic rod whose dimensions can be controlled by external applied voltages. Normally a constant-current mode is used where a feedback loop adjusts the tip-substrate distance in order to maintain a fixed current. In the constant-current mode large-scale images can be obtained without tip damages and soft material such as organic molecules can be imaged without destruction.

### 2.1.1 Theory of STM

The tip and surface constitute a complex many-body system with a Schrödinger equation which so far has not been solved exactly. Fortunately, typical tip-sample separations of  $9\text{\AA}$  result in a weak coupling between tip and surface states, and electron tunneling can

therefore be treated by first order perturbation theory [142, 143]. By Fermi's "golden rule" the tunneling current is given by the Fermi function,  $f(E)$ , the bias voltage,  $V$ , and the tunneling matrix element,  $M_{\mu\nu}$ , between the tip states,  $\psi_\mu$ , and surface states,  $\psi_\nu$ :

$$I = \frac{2\pi e}{\hbar} \sum_{\mu\nu} f(E_\mu)[1 - f(E_\nu + eV)] \times |M_{\mu\nu}|^2 \delta(E_\mu - E_\nu). \quad (2.1)$$

For a positive bias voltage applied to the sample, the electrons consequently tunnel from filled tip states into empty surface states.

The essential problem, in the determination of the tunneling current, is to calculate the matrix element. Bardeen [144] showed that the matrix element could be reduced to

$$M_{\mu\nu} = \int \mathbf{j}_{\mu\nu} \cdot d\mathbf{S} \quad (2.2)$$

where the current density,  $\mathbf{j}_{\mu\nu}$  is integrated over any surface lying entirely within the barrier region separating the two electrodes.

Assuming only s-wave tip states, Tersoff and Hamann [142, 143] found that the tunneling current for small bias voltages and temperatures represents the local charge density of states at the Fermi level,  $E_F$ , for the surface at the position of the tip,  $r_t$ :

$$I \propto V \sum_{\nu} |\psi_\nu(\mathbf{r}_t)|^2 \delta(E_\nu - E_F) = V \rho(\mathbf{r}_t, E_F). \quad (2.3)$$

The STM-tip, when scanned in the constant-current mode, thus follows contours with a constant local density of electron states.

If the potential barrier,  $U$ , is equal to the vacuum level, the surface states at the Fermi level decay into the vacuum gap with an effective energy barrier given by the work function,  $\phi$ :

$$\psi_\nu(z) = \psi_\nu(0)e^{-\kappa z}, \quad \kappa^2 = 2m(U - E_F)/\hbar^2 = 2m\phi/\hbar^2. \quad (2.4)$$

The tunneling current is therefore exponentially dependent on the distance,  $d$ , between the tip and the surface:

$$I \propto V e^{-\frac{1}{\hbar}\sqrt{8m\phi}r_t} \sum_{\nu} |\psi_\nu(0)|^2 \delta(E_\nu - E_F) \propto e^{-\frac{1}{\hbar}\sqrt{8m\phi}d}. \quad (2.5)$$

The atomic resolution achieved with STM is based on this exponential dependence. For a standard work function of 4 eV a decrease in tip-surface distance of 1 Å results in an increase in the tunneling current of around an order of magnitude. This furthermore implies that the tip apex atom carries by far the largest current, explaining why even non-sharp tips can achieve atomic resolution.

### 2.1.2 Imaging of adsorbates

Since STM maps contours of local density of states (LDOS) at the Fermi level, the atomic corrugation of a metal surface can be resolved and understood directly. In contrast it is less straight forward to obtain insight about the chemical state of the system [140].

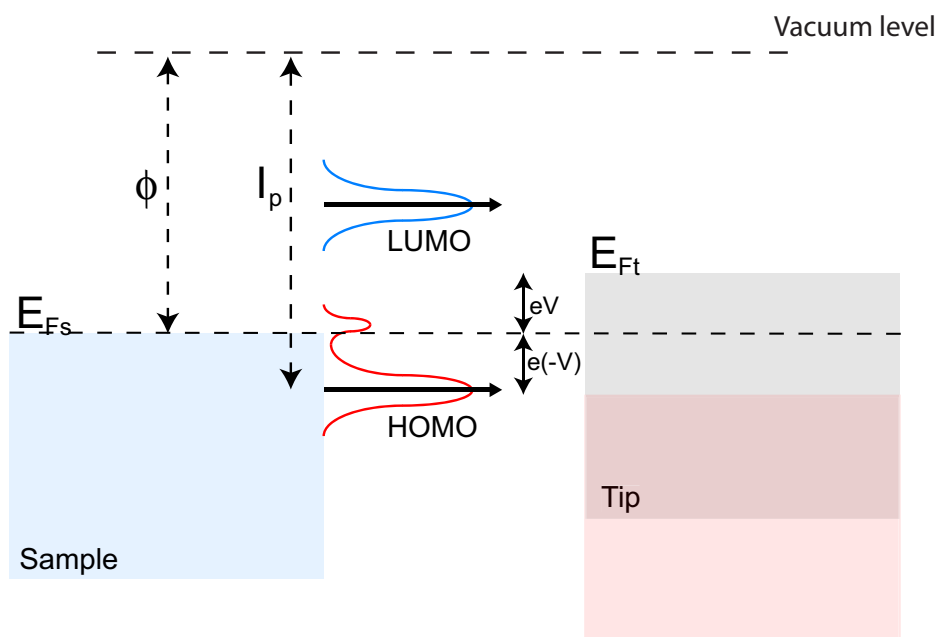


Figure 2.2: Imaging of adsorbed molecules.

In the simple case of a single-atom adsorbate, Lang showed that the contrast in the STM image could be attributed to the change in local density of state near the Fermi level induced by the adsorbate [145]. This means that depending on the distribution of atomic levels and the substrate some adsorbates are imaged as protrusions whereas others are imaged as depressions.

Adsorbed organic molecules normally distribute the highest occupied molecular orbital (HOMO) and lowest unoccupied molecular orbital (LUMO) around the Fermi level. Due to the coupling with the states of the underlying metal, especially the d-band [146], the orbitals are broadened. In a simplified model, as sketched in Fig. 2.2, the orbital with an energy closest to the Fermi level of the substrate is expected to have the dominant contribution to the change in tunneling current [147, 148]. Whether the HOMO or LUMO is imaged thus depends on the size of the ionization potential and electron affinity of the adsorbed molecule in combination with the size of the work function of the substrate. If the HOMO and the LUMO are both close to the Fermi level, the STM signature can be bias dependent [149].

In reality different orbitals often add to the contrast in the images [150], and the overlap between the tip wave functions and the molecular orbitals contribute to the tunneling current. Ou-Yang et al. modelled the STM tip by a semi-infinite chain of atoms and found that the overall brightness depends on the effective density of states of the sample at the adsorbate, whereas the intramolecular contrast primarily arises from the overlap between the tip and molecular states [151].

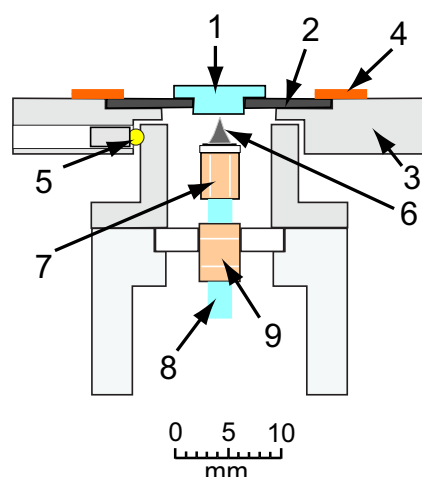


Figure 2.3: The Aarhus STM [154]

For a more quantitative interpretation of the obtained STM images, extended calculations should be performed, such as density functional theory calculations [12] determining the local density-of-states based on the Bardeen-Tersoff-Hamann approximation, or electron scattering quantum chemical calculations (ESQC) [152, 153] in which the tunneling gap is treated as a defect to the periodic electronic structure in the tip and surface. Another possibility is to decouple the substrate and molecular system by a thin layer of insulation material, such as sodium chloride, in which case the orbitals of the free molecule can be imaged directly [153].

### 2.1.3 The Aarhus STM

The STM data presented in this thesis have all been obtained with the home-built Aarhus STMs developed by Lægsgaard et al. [155]. A schematic model of the latest version is shown in Fig. 2.3.

The sample (1) is mounted on a tantalum holder (2) fastened to the top plate (3) by two copper springs (4) to ensure thermal and electrical contact. The top plate is isolated from the STM body by three quartz balls (5). The top plate is mounted on an Al block which can be cooled to  $\sim 115$  K before scanning via a contact to a dewar cooled with liquid nitrogen. During scanning the contact must be broken which results in a slow heat up of the STM and thereby a drift in the sample temperature.

The scanning is performed by a tungsten tip (6) mounted on a piezoelectric cylindrical 4-fold segmented scanner tube (7). The scanning in the x,y direction is achieved by applying antisymmetrical voltages to opposite electrodes on the scanner tube compared to an inner electrode. The tip-sample distance is maintained by a feedback system with the tunneling current as input. The scanner tube is mounted on a ceramic rod (8). The design of the scanner tube and feedback system allow a fast scanning where  $128 \times 128$

pixel images are acquired within a few seconds or even faster. Furthermore a software based drift compensation system exists leading to the possibility of time resolved image collection of several hundred images (STM movies) on the same spot on the surface.

The coarse approach of the tip towards the surface is realized by a linear motor (9), called the inchworm, consisting of a second piezoelectric tube fitted around the ceramic rod by two bearings. The inchworm consists of three sections with electrodes attached. The middle section controls the elongation of the tube while the upper and lower sections clamp/unclamp the piezo tube to the rod. By applying a sequence of voltages to the 3 electrodes, the rod can be pushed upwards/downwards in a worm-like fashion. To prevent tip collisions the motor stops at a preset value of the tunnel current.

The compact design of the Aarhus STM makes it resistant towards low frequency vibrations while high frequency vibrations are damped out by suspending the STM by four soft springs.

## 2.2 Synchrotron studies

X-ray photoelectron spectroscopy and x-ray absorption spectroscopy can give valuable information on the chemical composition of the surface and even of the chemical state of the adsorbates. Both techniques gain their surface sensitivity from the fact that electrons (with kinetic energy between 20 eV and 500 eV), in a solid have a low mean free path,  $\lambda$  ( $\sim 5 - 10$  Å), which implies that only electrons emitted from atoms close to the surface can escape the solid before undergoing inelastic scattering. The spectroscopic data presented in this thesis have been obtained at the synchrotron radiation beamlines HE-SGM at Bessy II (Berlin) and I311 at MAX-lab (Lund).

### 2.2.1 X-ray photoelectron spectroscopy

X-ray photoelectron spectroscopy (XPS) [156–158] is based on the photoelectric effect. In a simple picture, a photon of energy,  $h\nu$ , excites core electrons into the vacuum by an ionization process, as sketched in Fig. 2.4. The kinetic energy of the emitted electron is given by

$$E_{kin} = h\nu - E_b - \phi \quad (2.6)$$

where  $\phi$  is the work function of the metal substrate and  $E_b$  is the binding energy of the electron. The binding energy of the electron is element-specific and sensitive to the chemical state of the emitting atom. In an XPS spectrum a constant photon energy is used, and the intensity of released electrons is normally plotted versus the binding energy. The detection limit is  $\sim 1\%$  of a monolayer and the technique is thus also used to judge the cleanliness of the sample.

### 2.2.2 X-ray absorption spectroscopy

Near-edge x-ray absorption fine-structure spectroscopy (NEXAFS) [158, 159] relies on the promotion of core electrons to unoccupied states in the vicinity of the absorption



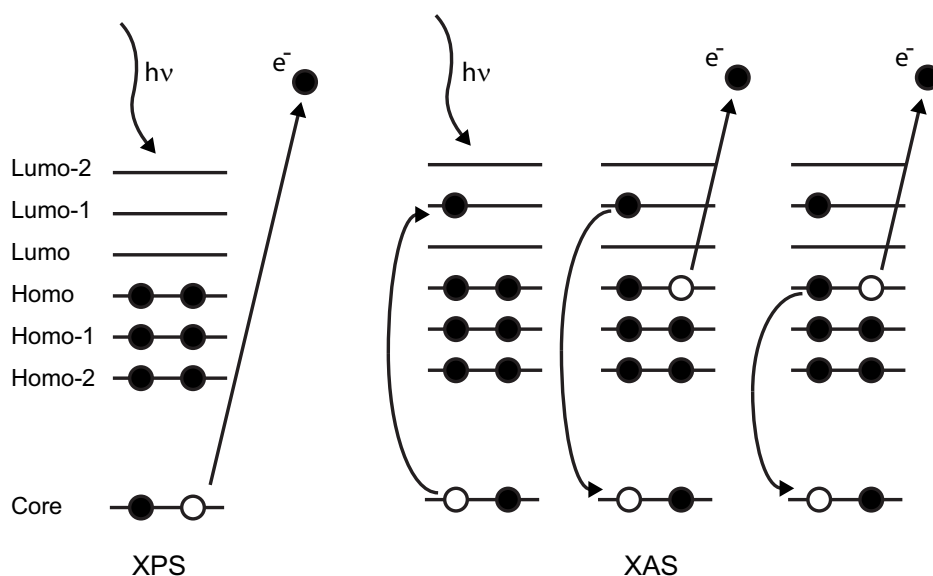


Figure 2.4: Principle behind XPS and XAS

edge by photons of well-defined energy,  $h\nu$ , followed by Auger decays (see Fig. 2.4). This implies that NEXAFS is an excellent tool for mapping the chemical bonding properties of low-Z molecules, such as O, N and C, forming characteristic intramolecular  $\pi$  and  $\sigma$  bonds.

The cross section,  $\sigma$  for the adsorption process given by the electric field of the light,  $\mathbf{E}$ , the transition matrix element,  $\langle f|\mathbf{p}|i \rangle$  and the density of final states,  $\rho_f(E)$  can be derived from Fermi's golden rule. The initial state is the localized core state and the final state is the extended state of the outgoing electron wave.

$$\sigma = \frac{4\pi^2 e^2}{m^2 c \omega} \left| \frac{\mathbf{E}}{|\mathbf{E}|} \langle f|\mathbf{p}|i \rangle \right|^2 \rho_f(E) \delta(h\nu + E_i - E_f) \quad (2.7)$$

The characteristics of NEXAFS are revealed in the cross section: (i) The necessity of overlap between initial and final states expressed in the transition matrix element,  $\langle f|\mathbf{p}|i \rangle$ , implies that NEXAFS probes intramolecular transitions. (ii) The proportionality to the local energy density of final states,  $\rho_f(E)$ , implies that the technique is sensitive to the local chemical bonding scheme. (iii) The scalar product between  $\mathbf{E}$  and  $\mathbf{p}$  gives rise to an angular dependence of the cross section which makes the technique sensitive to molecular adsorption geometries. (iv) Only transitions from  $1s$  core states to final states with  $p$ -character are mapped since the incident x-rays fulfill the dipole approximation.

In a NEXAFS spectrum the intensity is normally plotted versus the photon energy, and the resonances show up as characteristic peaks below and above the adsorption edge.

## 2.3 Density functional theory

Density functional theory (DFT) is a powerful approach for description of the ground state properties of complex many-body systems such as molecules and solids. In this thesis DFT has been applied to determine adsorption geometries, energy barriers and even reaction pathways. All the calculations presented were performed by theoreticians in the group of B. Hammer, University of Aarhus, and my own contribution thus lie entirely in the discussion of interesting model systems and the results obtained.

In principle, any system of interacting electrons and atoms can be described by the time-independent Schrödinger equation

$$\hat{H}\Psi(\mathbf{r}_1, \mathbf{r}_2, \dots, \mathbf{r}_n) = E\Psi(\mathbf{r}_1, \mathbf{r}_2, \dots, \mathbf{r}_n) \quad (2.8)$$

where  $\hat{H}$  is the Hamilton operator,  $E$  the total energy of the system, and  $\Psi(\mathbf{r}_1, \mathbf{r}_2, \dots, \mathbf{r}_n)$  the many-body wave function containing all the information about the physical state of the system. However, if the problem involves more than a few particles the Schrödinger equation becomes computationally difficult to solve and approximations are required. The first approximation used for most systems is the Born-Oppenheimer approximation where the nuclei are fixed at their equilibrium position and only the electrons are free to move.

The basic idea in DFT is to reduce the computational cost further by replacing the many-body wave-function,  $\Psi$ , by the electron density,  $n(\mathbf{r})$ . Hohenberg and Kohn [160] demonstrated that the total external potential,  $v(\mathbf{r})$  (to within a constant) is a unique functional of  $n(\mathbf{r})$ . This implies that the hamiltonian and thereby the total ground state energy,  $E$ , of the many-electron system can be expressed by the electron density and the sum of external fields,  $v(\mathbf{r})$

$$E[n] = \int n(\mathbf{r})v_{ext}(\mathbf{r})d\mathbf{r} + \frac{1}{2} \int \int \frac{n(\mathbf{r})n(\mathbf{r}')}{|\mathbf{r} - \mathbf{r}'|} d\mathbf{r}d\mathbf{r}' + G[n]. \quad (2.9)$$

where the functional  $G[n]$  does not depend on  $v(\mathbf{r})$ .

Kohn and Sham [161] split the functional  $G[n]$  into two terms, a kinetic contribution from the non-interacting electron gas,  $T_s[n]$ , and the exchange and correlation energy,  $E_{xc}[n]$ , containing the contributions from the interacting electron gas. By applying the Rayleigh-Ritz variation principle they derived a set of single-electron Schrödinger equations referred to as the Kohn-Sham equations

$$\left(-\frac{1}{2}\nabla^2 + v_{eff}(\mathbf{r})\right)\phi_i(\mathbf{r}) = \epsilon_i\phi_i(\mathbf{r}). \quad (2.10)$$

Here the single electron wavefunctions,  $\phi_i$ , determine the electron density

$$\sum_i |\phi_i(\mathbf{r})|^2 = n(\mathbf{r}) \quad (2.11)$$

and the effective potential,  $v_{eff}(\mathbf{r})$ , is comprised of the total electrostatic potential and the derivative of  $E_{xc}$

$$v_{eff}(\mathbf{r}) = v(\mathbf{r}) + \int \frac{n(\mathbf{r}')}{|\mathbf{r} - \mathbf{r}'|} d\mathbf{r}' + \frac{\delta E_{xc}[n(\mathbf{r})]}{\delta n(\mathbf{r})}. \quad (2.12)$$

In a DFT calculation the Kohn-Sham equations are solved repeatedly from a trial density,  $n(\mathbf{r})$ , until self-consistency is obtained. When convergence is reached the total energy of the system can be found by

$$E = \sum_i \epsilon_i - \frac{1}{2} \iint \frac{n(\mathbf{r})n(\mathbf{r}')}{|\mathbf{r} - \mathbf{r}'|} d\mathbf{r}d\mathbf{r}' + E_{xc}[n] - \int \frac{\delta E_{xc}[n(\mathbf{r})]}{\delta n(\mathbf{r})} n(\mathbf{r}) d\mathbf{r}. \quad (2.13)$$

The only approximations which have to be made are in the exchange and correlation energy,  $E_{xc}$ . Kohn and Sham used the local density approximation (LDA) in which the exchange and correlation energy is solely a function of the density

$$E_{xc}[n] = \int n(\mathbf{r}) \epsilon(n(\mathbf{r})) d\mathbf{r}. \quad (2.14)$$

The LDA approximation gives reasonable results if the electron density varies slowly. In the more improved, generalized gradient approximation (GGA), the exchange correlation energy is normally a function of both the density and the gradient of the density

$$E_{xc}[n] = \int f(n(\mathbf{r}), \nabla n(\mathbf{r})) d\mathbf{r}. \quad (2.15)$$

However also the GGAs fail when the electron density varies too fast. This means in particular that Van der Waals interactions are not taken into account in a DFT calculation. The generalized gradient approximation used in most of the calculations presented in this thesis is the Perdew-Wang 91 (PW91) functional [162, 163].

## 2.4 Experiments

The experiments described in this thesis were performed in two different UHV chambers, an old system<sup>1</sup> and a new-built system<sup>2</sup>, designed especially for molecular studies.

The single crystal surfaces were prepared in the main chambers by sputtering with  $Ar^+$  ions and radiative heating by an Osram filament mounted on the manipulator holding the sample. In the new setup the sputtering and annealing cycles were computer controlled, allowing for over-night sample preparations.

Deposition of large organic molecules<sup>3</sup>, forming powders at room temperature, was carried out in the main chambers by resistive heating from a glass crucible surrounded by a metal wire. The molecular powder was prior to evaporation purified by long-term outgassing (several days) at the deposition temperature and a short-time outgassing at a slightly higher temperature. Deposition from a well-outgassed molecular sample normally did not affect the chamber pressure. (In both systems a base pressure below  $5 \times 10^{-10}$  mBar could be achieved.) The temperature of the molecular powder was

<sup>1</sup>Referred to as the 'Orange' system

<sup>2</sup>Referred to as the 'Black' system

<sup>3</sup>This was the case for all molecules with a phenylene-ethynylene backbone.

during deposition measured by a Chromel and Alumel thermocouple pair melted into the glass.

All experiments with volatile molecules<sup>4</sup> were carried out in the new system. Besides the main chamber, the new system contains a small preparation chamber equipped with a separate turbo pump and a Penning gauge. The preparation chamber can be isolated from the main chamber by a gate valve allowing for high pressures ( $\sim 10^{-5}$  mBar) of molecules during the deposition process without affection of the pressure in the main chamber. The sample can easily be transferred between the main and side chamber by a second manipulator with a built-in linear motion. This furthermore implies that the side chamber can be used as a load-lock. The volatile molecules were dosed directly into the preparation chamber through a leak valve. Prior to evaporation impurities with higher vapour pressures were removed by successive cool/pump/thaw cycles.

A further advantage of the new system compared to the old system is the possibility during preparation to maintain the sample at any desired temperature above  $\sim 100$  K. This is realized by liquid nitrogen cooling systems combined with radiative heating. The sample can furthermore easily be transferred between the manipulators and the STM by a wobble stick causing only a minor temperature increase ( $< 10$  K) during the movement.

---

<sup>4</sup>This includes azobenzene and the amine compounds.

## CHAPTER 3

---

### Diffusion of azobenzene

---

The diffusivity of molecules adsorbed on solid surfaces depends on the molecule-substrate interaction. In this chapter the adsorption geometries of azobenzene on Cu(110) are investigated at low coverage and saturation limits and correlated with the diffusion behavior of azobenzene in both preferred and energetically metastable adsorption states.

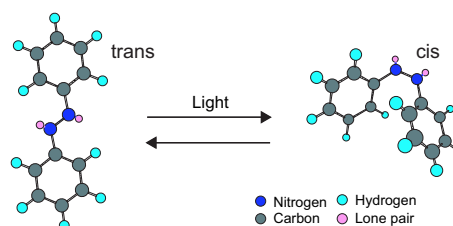


Figure 3.1: The photochemical cis-trans isomerization of azobenzene.

## 3.1 Introduction

### 3.1.1 Azobenzene

Azobenzene (Fig 3.1) is one of the most well-known members of the photoactive azo family, and consists of two benzene rings joined by an azo group (two double-bonded nitrogen atoms). In the ground electronic state azobenzene has two isomeric forms, a nearly planar trans conformation and a three-dimensional cis conformation (Fig. 3.1<sup>1</sup>). The trans isomer is approximately 0.6 eV lower in energy than the cis isomer, and they are separated by an energy barrier of around 1.6 eV (measured from trans to cis) [164]. In thermal equilibrium the fraction of cis isomers at room temperature should thus be negligible. The switching between the two isomeric forms can be induced by photoradiation [165]. Consequently azobenzene and derivatives thereof are often found in dyestuffs [166] and used for optically active materials and devices [167–169]. The cis and trans isomer absorb light at the same wave lengths, but due to the steric hindrance present in the cis isomer, the maximum adsorbance of the cis isomer occurs at a higher wave length than the maximum absorbance of the trans isomer. The portion of cis isomers in the sample can therefore be regulated by the wave length of the irradiating light. For a sample of azobenzenes held in visible light  $\sim 10\%$  of the cis isomer is expected [170].

The reversible photochemical cis-trans isomerization makes azobenzene compounds promising as model systems for molecular switches applicable in molecular electronics and sensor functionalizations [164, 171–174]. Adsorption of azobenzene on HOPG has been studied by STM in air [175]. The switching of azobenzene derivatives at the liquid-solid interface has been demonstrated both by UV light [91, 176–180] and by electrons from the STM-tip [180]. Recently the adsorption of azobenzene derivatives on Au(111) under ultrahigh vacuum (UHV) conditions has been studied extensively, and the adsorption structure at different coverages [181, 182] as well as STM tip induced dynamical phenomena such as rotations [182], lateral movements [182], clustering [182], and conformational cis-trans switching [133–135, 182] have been demonstrated. On Au(111) azobenzene is highly diffusive at sample temperature above 50 K and can only be trapped at defect sites [182].

<sup>1</sup>The minimum energy conformations shown were estimated by chem office using the MM2 routine with a minimum RMS gradient of 0.100.

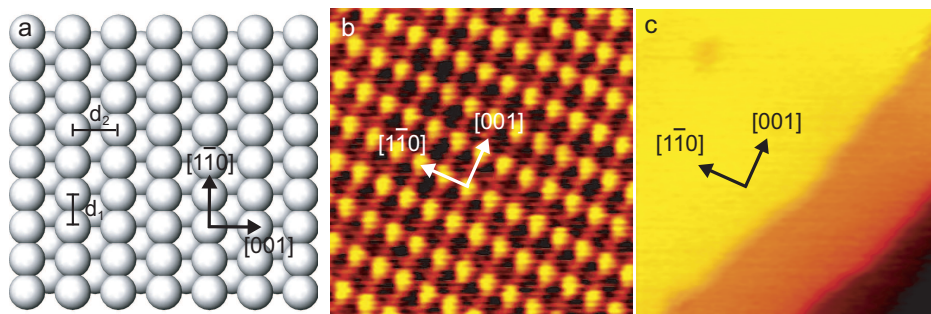


Figure 3.2: The Cu(110) surface. (a) Ball model. (b) Small scale STM image (size  $30 \times 30 \text{ \AA}^2$ ,  $I_t = 1.71 \text{ nA}$ ,  $V_t = 11.9 \text{ mV}$ ). (c) Large-scale STM image (size  $700 \times 700 \text{ \AA}^2$ ,  $I_t = 1.68 \text{ nA}$ ,  $V_t = 2.7 \text{ mV}$ ).

In this chapter UHV-STM is applied to investigate both the adsorption geometries of azobenzene on Cu(110) at different coverages and the diffusion behavior in preferred and metastable adsorption states [21].

### 3.1.2 Methods

The Cu(110) surface was cleaned by repeated cycles of  $1.5 \text{ keV Ar}^+$  ion bombardment followed by annealing to  $820 \text{ K}$ . The cleanliness of the surface was checked by STM images obtained at room temperature showing large flat terraces of sizes up to  $500 \times 500 \text{ \AA}^2$  (Fig. 3.2c). On small-scale images the parallel copper rows running along the  $[1\bar{1}0]$  direction could be resolved with atomic resolution (Fig. 3.2b). Atomic-scale resolution images with a minimum drift were applied for calibration using  $d_1 = 2.56 \text{ \AA}$  and  $d_2 = 3.62 \text{ \AA}$  (Fig. 3.2a).

Azobenzene (Sigma-Aldrich, 99.5% purity), visualized as reddish crystals, was held in a transparent glass vial at room temperature and admitted into the UHV chamber via a leak valve resulting in a subsaturation coverage. All STM measurements were obtained with an STM cooled down to temperatures in the range of  $120 - 170 \text{ K}$ . The molecules were best imaged with tunneling parameters of  $V_t = -2.0 \text{ V}$  and  $I_t \sim 0.35 \text{ nA}$  which were used unless stated otherwise.

### 3.1.3 Diffusion in one dimension

Adsorbed molecules can migrate between the different stable sites on a surface by successive jumps [109, 183] (Fig. 3.3). The jumps are thermally activated [110, 184] and transition state theory therefore predicts the hopping rate,  $h$ , to follow an Arrhenius dependence on the temperature given by an entropy dependent attempt frequency,  $h_o$ , Boltzmanns constant,  $k_B$ , and the energy barrier,  $E_D$ , between the stable state and the transition state

$$h = h_o e^{(-E_D/k_B T)}. \quad (3.1)$$

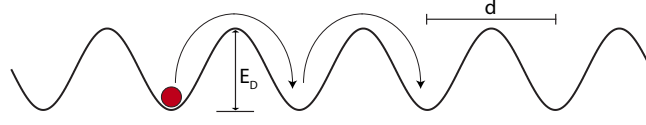


Figure 3.3: Diffusion in one dimension.

If the hopping rate,  $\frac{1}{\tau}$ , is considerably longer than the duration of a jump,  $\tau$ , the single jump events can be considered independent. Furthermore, if the energy landscape is symmetric and periodic<sup>2</sup>, the diffusion process can be described as a simple random walk with the mean-squared displacement,  $\langle (\Delta x)^2 \rangle$ , given by the mean-square jump length,  $\lambda^2$ , the hopping rate and the time interval,  $t$ ,

$$\langle (\Delta x)^2 \rangle = \lambda^2 h t. \quad (3.2)$$

As seen from Eq. (3.2) the mean-squared displacement scales linearly with time. The time-independent tracer diffusion coefficient can therefore be defined as<sup>3</sup>,

$$D = \lim_{t \rightarrow \infty} \frac{\langle (\Delta x)^2 \rangle}{2t} \quad (3.3)$$

which by Eq. (3.2) and Eq. (3.1) reduces to

$$D = \frac{1}{2} \lambda^2 h = \frac{h_o \lambda^2}{2} e^{(-E_D/k_B T)}. \quad (3.4)$$

If the molecules are restricted to jumps between nearest neighbor sites<sup>4</sup>, the root mean-square jump length,  $\lambda$ , is equal to the lattice distance,  $d$ , and the diffusion constant,  $D$ , is then related to the diffusion barrier by

$$D = \frac{h_o d^2}{2} e^{(-E_D/k_B T)}. \quad (3.5)$$

## 3.2 Adsorption geometries

### 3.2.1 Room-temperature deposition

When azobenzene is deposited onto a Cu(110) surface held at room temperature, individual molecules appear as two bright protrusions, attributed to flat-lying phenyl rings, separated by a darker line associated with the N=N bond (Fig. 3.4a). This molecular signature is qualitatively as expected for the trans isomer. The molecules adsorb with

<sup>2</sup>This is the case for diffusion along an atomic row as in this study

<sup>3</sup>In the analysis of STM movies we average over a large number of jumping events and use the finite time ( $\sim 10$  s) between two consecutive images.

<sup>4</sup>In this approximation long jumps [113] are neglected.



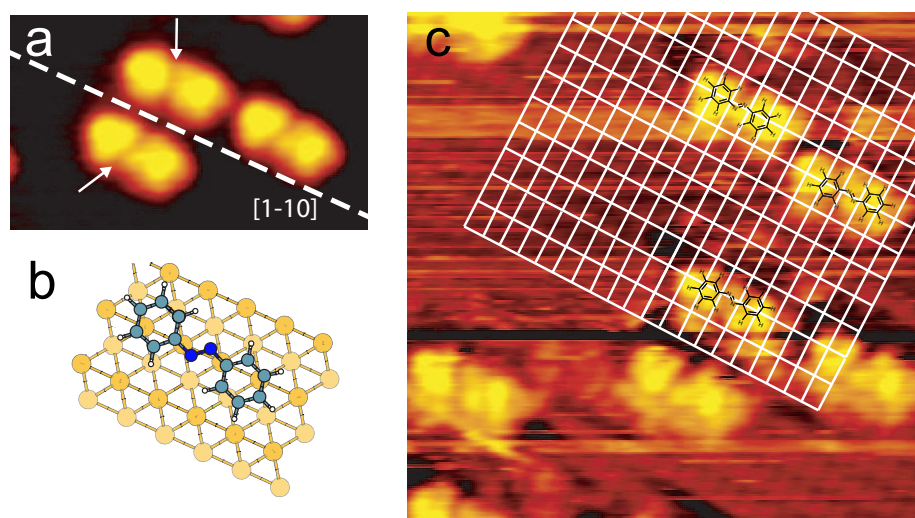


Figure 3.4: Azobenzene on Cu(110). (a) Single molecules in two enantiomeric forms ( $50 \times 30 \text{ \AA}^2$ ). (b) Ball model of the adsorption geometry. (c) Determination of adsorption geometry from the underlying atomic lattice. Grid intersections correspond to the position of copper atoms ( $V_t = -0.12 \text{ V}$ ,  $I_t = 0.850 \text{ nA}$ ,  $70 \times 70 \text{ \AA}^2$ ).

their axis at a slight angle to the close-packed  $[1\bar{1}0]$  direction and with their  $\text{N}=\text{N}$  bond at a bridge site as determined from images showing the Cu lattice at atomic resolution (Fig. 3.4c). Loss of symmetry upon adsorption results in two different surface enantiomers, distinguishable by the direction of the central dark line as indicated by arrows in Fig 3.4a. A possible model of the molecular adsorption geometry is depicted in Fig. 3.4b (the enantiomer with the  $\text{N}=\text{N}$  bond along the dark line is tentatively chosen to correspond to the shown direction of rotation).

As the coverage is increased, the molecules do not show a strong tendency to cluster together (3.5a), even if annealed to 500 K. Near half of saturation coverage (Fig. 3.5b) the molecules begin to order by stacking sideways into columns running along the substrate  $[001]$  direction. The molecular head-to-head interaction appears to be weak or even repulsive as no ordering is observed along this direction.

At saturation coverage (Fig. 3.5c) the molecules form columns along the  $[001]$  direction with a periodicity of  $7.9 \pm 0.8 \text{ \AA}$  (dimension a in Fig. 3.5c), consistent with two lattice spacings of the Cu substrate. At this separation, intermolecular H-N hydrogen bonding can occur with a reasonable bond length of less than  $4 \text{ \AA}$ . The column-column distance along the  $[1\bar{1}0]$  direction is  $14.3 \pm 1.4 \text{ \AA}$  (dimension b in Fig. 3.5c). The structure has limited long-range order as entire columns are often shifted relative to each other by one lattice spacing along the  $[001]$  direction, leading to either head-to-head or interdigitating molecular arrangements (see Fig. 3.5c). Since the  $\text{N}=\text{N}$  bonds appear dark in the STM images, phenyl rings of adjacent molecules can appear to comprise a single molecule. However the assignment of the molecular features shown in Fig. 3.5c

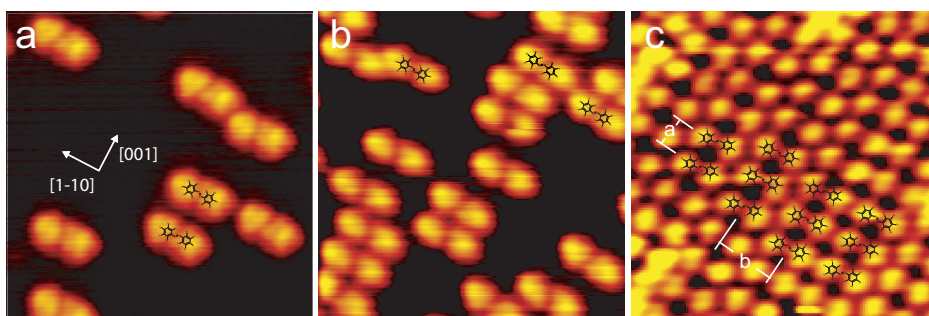


Figure 3.5: Azobenzene at different coverages. (a) Low coverage ( $70 \times 70 \text{ \AA}^2$ ). (b) Intermediate coverage ( $70 \times 70 \text{ \AA}^2$ ). (c) Saturation coverage. The structure does not appear to involve chiral segregation (the choice of enantiomers for the superimposed molecular models is arbitrary) ( $80 \times 80 \text{ \AA}^2$ ).

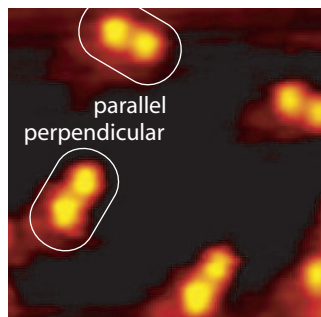


Figure 3.6: Perpendicular adsorption geometry observed upon deposition at a cold ( $\sim 120 \text{ K}$ ) surface ( $60 \times 60 \text{ \AA}^2$ ).

is confirmed by inspecting molecules close to step edges or defect sites.

### 3.2.2 Low-temperature deposition

Upon deposition onto a Cu(110) surface held at low temperatures ( $\sim 120 \text{ K}$ ), we observe a second adsorption geometry with the molecular axis perpendicular to the  $[1\bar{1}0]$  direction (Fig. 3.6). If the sample is annealed to  $300 - 500 \text{ K}$ , we no longer observe this perpendicular species. We therefore conclude that the parallel configuration is the most energetically favorable adsorption geometry and that the perpendicular configuration is a metastable state that is trapped upon adsorption on a cold surface. The similar appearance of the parallel and perpendicular configuration indicates that both cases are the trans isomer.

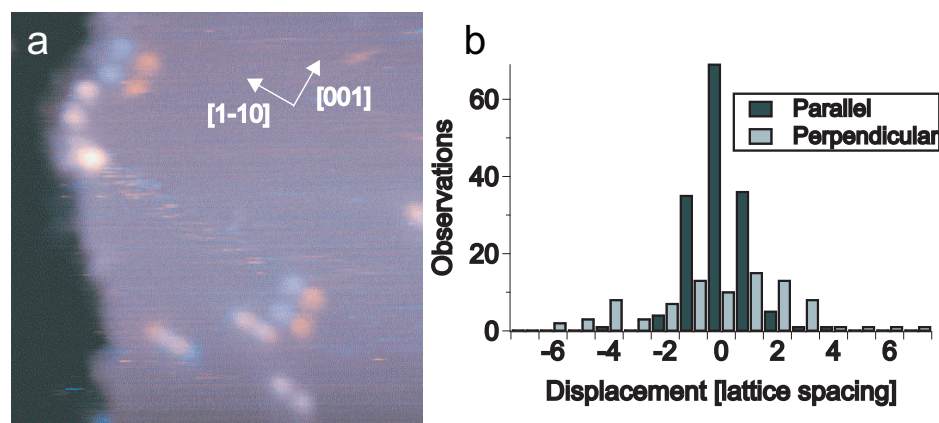


Figure 3.7: (a) Overlay of two time-separated STM images showing the diffusion of both parallel and perpendicular configurations. Blue/orange colours correspond to initial/final positions, respectively. Stationary features appear gray ( $140 \times 140 \text{ \AA}^2$ ). (b) A distribution of displacement for azobenzene at 168 K.

### 3.3 Diffusion

By acquiring sequences of time-lapsed STM images (STM movies) at 168 K, the diffusion of azobenzene for the parallel and perpendicular adsorption states was investigated. We observed that both species diffuse along the closed-packed  $[1\bar{1}0]$  direction and the diffusion is consequently one-dimensional. The shift in position of the adsorbates is demonstrated in Fig. 3.7a by superimposing two sequential STM images of the same portion of the surface. The images have been colored blue and orange, respectively, such that stationary molecules appear grey, and blue/orange indicates initial/final positions of the molecules that have moved. The molecular displacements, determined at lattice spacing resolution, are plotted in the two histograms of Fig. 3.7b. At 168 K we found diffusion coefficients,  $D$ , for the parallel and perpendicular configurations  $0.2 \times 10^{-16} \text{ cm}^2/\text{s}$  and  $1.3 \times 10^{-16} \text{ cm}^2/\text{s}$ , respectively. Assuming only nearest neighbor jump events<sup>5</sup>, this corresponds to a difference in activation energy of  $\Delta E = 0.03 \text{ eV}$ . Furthermore using an attempt frequency [113, 118] of  $10^{12} \text{ s}^{-1}$  we find activation energies of 0.44 eV (parallel) and 0.41 eV (perpendicular). This may be compared to recent results for adsorption of azobenzene on Au(111) showing a much higher mobility on this substrate [181]. The  $\sim 6$  times greater diffusion coefficient for the perpendicular configuration compared to the parallel one demonstrates that different orientations of the same isomer influence the molecular diffusivity. A similar result was recently demonstrated by manipulating a large organic molecule into a metastable state using the STM tip [114]. In the present system, however, the molecules spontaneously assume the metastable state of higher mobility by deposition onto a cold surface.

<sup>5</sup>An assumption of equal root mean-squared jump lengths for the perpendicular and parallel adsorption states is equally valid in the determination of the difference in activation energy [113, 183].

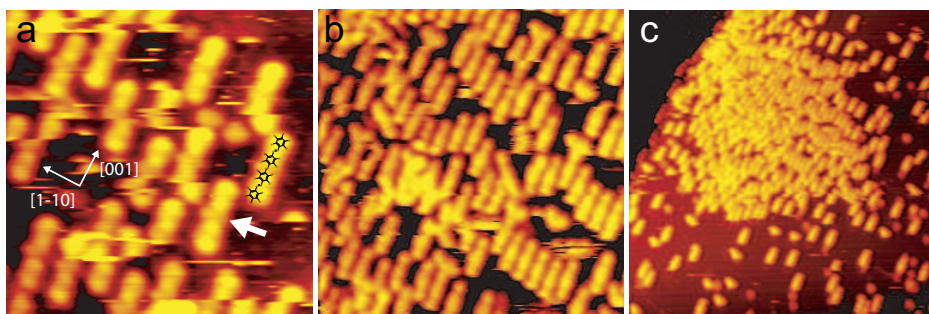


Figure 3.8: Tip-induced clustering. (a) High-resolution STM image of azobenzene dimers ( $70 \times 70 \text{ \AA}^2$ ). (b) Dimer cluster formed after successive scanning of the same area ( $150 \times 150 \text{ \AA}^2$ ). (c) Zoom out of the area in (b) ( $380 \times 380 \text{ \AA}^2$ ).

### 3.4 Clustering

In some experiments we observed clustering of azobenzene molecules. We interpret the clusters to consist of azobenzene dimers oriented along the  $[001]$  direction of the substrate, as shown in the overlay of Fig. 3.8a. At the connection point of the dimer we sometimes observe two protrusions (the arrow in Fig. 3.8a) which we speculate to be stabilizing copper ad-atoms [185]. The STM image in Fig. 3.8b shows an area which was scanned several times with a sample bias of  $\sim 2 \text{ V}$  and a tunneling current of  $0.4 \text{ nA}$ . For each scan the density of molecules grew. Zooming-out (Fig. 3.8c) revealed that cluster formation only took place at the scanned area. The cluster formation must therefore be tip-induced. The azobenzene dimers could be formed by molecules collected and subsequently dropped by the STM tip. Alternatively, the dimers result from catching and anchoring of highly diffusive azobenzene molecules, perhaps *cis*-isomers, to copper ad-atoms by the STM tip. A similar cluster formation of azobenzene on Au(111) by anchor-site creation has been observed by Comstock et al., if they applied voltage pulses below  $-4 \text{ V}$  to the STM tip [182].

### 3.5 Discussion

Although azobenzene may exist in either a *trans* or a *cis* conformation we only appear to observe the former after deposition. In the photostationary state existing in the transparent glass vial holding the molecules (exposed to ordinary laboratory light), the fraction of *cis* isomers is expected to be significantly higher, in the order of 10 percent [165,170]. It is possible that *cis* conformers dosed onto the surface relax to the *trans* form upon adsorption. Alternatively, the non-planar conformation of the *cis* isomer in the gas phase could imply that the *cis*-isomer adsorbs with only one phenyl ring attached to the surface, appearing slightly larger than a single phenyl ring. This was observed for azobenzene on Au(111) [135]. A non-flat adsorption geometry should result in a lower molecule-surface interaction for the *cis* isomer compared to the *trans* isomer which may lead

to more diffusive species. Occasionally we observe highly mobile entities which we speculate could be cis isomers, but the experimental setup does not allow for sufficiently low sample temperatures to stabilize them.

In the experiments we were not able to induce trans-cis isomerizations by the STM tip. This could be a result of the stronger binding between azobenzene and Cu(110) compared to Au(111). To obtain conformational switching [23] on Cu(110), it may therefore prove helpful to provide thermal activation in conjunction with photoirradiation.



## CHAPTER 4

---

### Conformational switching for a class of oligo-phenylene-ethynylenes

---

Both dynamical and stereochemical effects play an important role in the build-up of functional nanoarchitectures. In this chapter the self-assembly of a class of three conjugated organic molecules is investigated. A chiral switching process is demonstrated by which the molecules alter their conformation after adsorption by thermally induced intramolecular rotations. The switching process enables a new and efficient channel towards chiral segregation into homochiral networks.

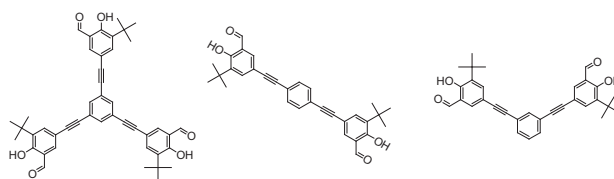


Figure 4.1: The three compounds studied here with (from left to right) *threespoke*, *para*, and *meta*-configuration.

## 4.1 Introduction

In this chapter we investigate chiral ordering and conformational dynamics for a class of three highly conjugated organic molecules (oligo-phenylene-ethynylenes) using time-resolved STM under ultra-high vacuum (UHV) conditions [22, 23]. The molecules (see Fig. 4.1) vary in geometry, but contain the same functional moieties. After adsorption on a Au(111)-(22 × √3) surface, the molecules assume various surface conformations, some of which are chiral. Chirality is also expressed in the tiling pattern of several of the observed molecular adsorption structures, and we find that the two levels of chirality, organizational and intramolecular, display a high degree of correlation which, for some of the structures, reflects differences in interaction energies between different surface conformers as small as 0.005 – 0.05 eV.

Dynamically, the molecules are found to be able to undergo a thermally induced conformational change, involving rotation of a bulky molecular end-group, which causes them to switch between chiral and non-chiral forms or between opposite surface enantiomers. Kinetic studies performed in the temperature interval 150 – 220 K show that the conformational switching occurs with an activation energy of approximately 0.3 eV. The observed chiral switching enables a new mechanism towards segregation into homochiral domains in which the molecules dynamically accommodate to the chirality of the surrounding tiling pattern [77]. This new mechanism offers perspectives with respect to forming homochiral surface assemblies by seeding [13, 61] with a small quantity of an appropriate chiral compound.

A fourth member of the molecular class with an *ortho*-conformation of the molecular spokes displays an entirely different adsorption behavior on Au(111) and will be devoted its own chapter (Chapter 5).

### 4.1.1 The molecular system

Oligo-phenylene-ethynylenes are highly conjugated organic molecules built up by a few<sup>1</sup> benzene rings connected by triple bonds. The adsorption and conductivity behavior of thiol functionalized oligo-phenylene-ethynylenes on Au(111) has been studied extensively [186–189], and it has been demonstrated that the compounds display a high conductivity. Functionalized oligo-phenylenes-ethynylenes are thus interesting

<sup>1</sup>Oligo = "a few".



candidates for the formation of 1 and 2-dimensional molecular nanostructures formed by a bottom-up approach [32, 190, 191], requested as e.g. molecular wires in electronic devices.

The family of oligo-phenylenes-ethynylenes [192, 193] studied here (Fig.4.1) consists of a central benzene ring with two or three ethynylene spokes extending from it. In solution members of this family have been used as modules in DNA-programmed assembly [194, 195] and polycondensation [193]. For the two-spoke molecules, the *para*-compound<sup>2</sup> [193, 196] and the *meta*-compound<sup>3</sup>, the angle between the spokes is 180° and 120°, respectively, and for the *threespoke*-compound<sup>4</sup> [192, 193] the angle is 120°. Each ethynylene spoke is connected to a *tert*-butyl substituted salicylaldehyde moiety (a benzene ring with an aldehyde group, a hydroxyl group, and a *tert*-butyl group). The backbone of all three molecules consists of a conjugated  $\pi$ -system. Previous studies have shown that such conjugated systems preferentially align parallel to metal surfaces [27] in order to maximize the van der Waals (vdW) interaction with the surface.

In the gas phase the terminal salicylaldehyde moiety has freedom of rotation around the ethynylene spoke. (The energy barrier towards rotation for the *para*-compound is determined to 0.037 eV by simple DFTB calculations). When the molecules adsorb with the  $\pi$ -system parallel to the surface this rotation is hindered, leading to two possible orientations for each terminal moiety. The resulting surface conformers are summarized in Fig. 4.2. Some of the conformers do not have a mirror plane perpendicular to the surface, and are hence chiral. [27] To distinguish the different conformers, we note for each terminal group whether the *tert*-butyl group is to the left (L) or to the right (R) when looking along the spoke from the central benzene ring (and top-down on the molecule on the surface). For the *meta*-compound, the order of the terminal groups is taken to be counterclockwise in the enclosed angle.

For the *para*-compound, there are two salicylaldehyde moieties yielding 2<sup>2</sup> combinatorial possibilities, RL, LR, RR, and LL. RL and LR are identical, however, connected with a  $C_2$  rotation around the surface normal. This leaves three distinct surface conformers as shown. The RR and LL conformers are enantiomers. Similarly, in the case of the *meta*-compound there exist four combinatorial possibilities, but due to the bent geometry of the molecule, the RL and LR species are no longer equivalent. Hence we expect four different surface conformers with RR and LL being enantiomers. Finally, in the case of the *threespoke*-compound there are three salicylaldehyde moieties, leading to 2<sup>3</sup> combinatorial possibilities, some of which are related by a  $C_3$  rotation around the surface normal. As illustrated in Fig. 4.2 we expect for the *threespoke*-compound to find four different conformers grouped as two pairs of enantiomers.

The molecules, which form a solid at room temperature, were grinded into a powder and evaporated from a glass crucible heated to a temperature in the range of 360 – 400 K depending on the compound. The molecules were deposited in submonolayer coverage onto the Au(111) sample held at approximately 300 K. Prior to imaging the substrate was cooled to lower temperatures in the STM. Temperatures of 140 – 170 K were applied unless clearly stated otherwise. Close-packed self-assembled molecular islands of

<sup>2</sup>Systematic name: 1,4-bis[(5-*tert*-butyl-3-formyl-4-hydroxyphenyl)ethynyl]benzene.

<sup>3</sup>Systematic name: 1,3-bis[(5-*tert*-butyl-3-formyl-4-hydroxyphenyl)ethynyl]benzene.

<sup>4</sup>Systematic name: 1,3,5-tris[(5-*tert*-butyl-3-formyl-4-hydroxyphenyl)ethynyl]benzene.

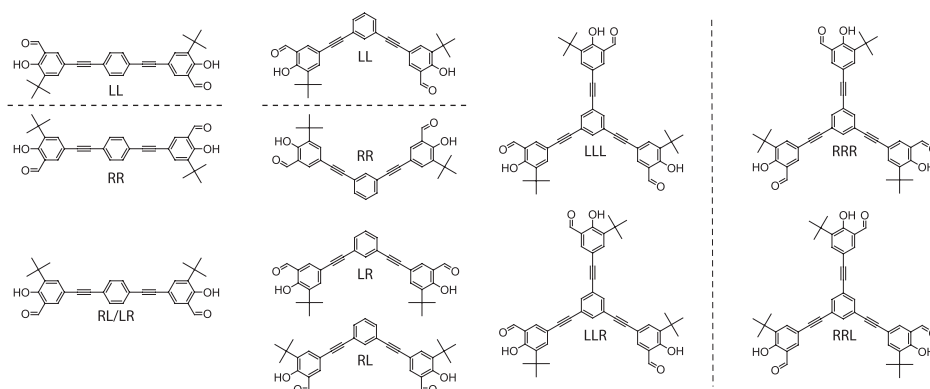


Figure 4.2: Surface conformers of the molecules. Top left: the *para*-compound has three conformers, two of which are enantiomers. Top right: the *meta*-compound has four conformers, two of which are enantiomers. Bottom: the *threespoke*-compound has four conformers, grouped as two times two enantiomers. Dashed lines indicate mirror planes.

monomolecular height were observed for all compounds investigated in this study. In general, the molecules were best imaged at  $\approx 1$  V bias voltage and  $\approx 1$  nA tunneling current. The polarity of the bias voltage did not have any systematic influence on the appearance of the molecules in the STM images, but negative bias voltage (applied to the sample) typically resulted in a more stable tunneling junction.

#### 4.1.2 Au(111)-( $22 \times \sqrt{3}$ )

The topmost layer of a (111) surface exhibits 6-fold symmetry (fig. 4.3a,b). If the underlying crystal has an fcc stacking, this is reduced to 3-fold symmetry<sup>5</sup>, as seen on Fig. 4.3a. This implies in particular that, depending upon whether a molecule interacts with the underlying crystal planes or only with the topmost layer, it will form molecular adsorption structures with either 3 or 6 equivalent rotational domains. Gold exhibits a reconstruction of the close-packed (111) surface [140, 197, 198]. This herringbone reconstruction (STM image in Fig. 4.3c) arises from a stress-induced uniform contraction of the topmost surface layer along the  $\langle 1\bar{1}0 \rangle$  direction resulting in a  $(22 \times \sqrt{3})$  rectangular unit cell containing both hcp and fcc sites. The transition between fcc and hcp stacking domains results in 0.2 Å corrugation double lines running along the  $\langle 11\bar{2} \rangle$  direction with a repeat distance of 63 Å. The regions within the double lines are hcp-like and regions between the double lines fcc-like. Consequently, the dominant stacking is fcc and hence fcc surface stacking is energetically more favourable than hcp stacking, as is the case in the bulk. As a consequence of the 3-fold symmetry the lines are created in three directions separated by 120°. At the boundary between two domains the lines are not completely parallel. The nearest neighbor distance between the Au(111) surface

<sup>5</sup>This is also the case for a hcp stacking.

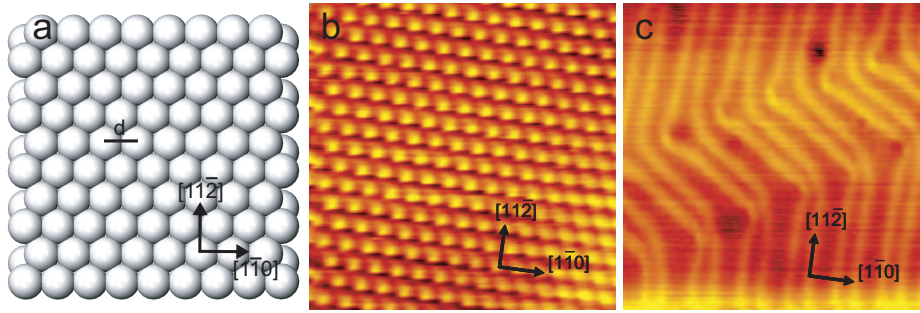


Figure 4.3: Au(111)-( $22 \times \sqrt{3}$ ). (a) Ball model of the 2 topmost (111) close-packed layers of an unreconstructed fcc crystal. (b) Atomic resolution on Au(111) ( $40 \times 40 \text{ Å}^2$ ,  $I_t=1.83 \text{ nA}$ ,  $V_t = 15.3 \text{ mV}$ ). (c) Herringbone reconstruction ( $500 \times 500 \text{ Å}^2$ ,  $I_t = 2.05 \text{ nA}$ ,  $V_t = 40.9 \text{ mV}$ ).

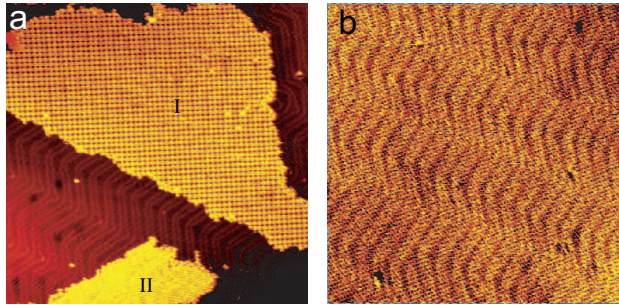


Figure 4.4: (a) Examples of coexisting monomolecular high islands formed from *para*-molecules. I: Grid structure, II: Brick-wall structure. (b) The Au(111) herringbone reconstruction is visible as a height modulation in the molecular islands (here formed by the *meta*-molecules). Image sizes  $1550 \times 1550 \text{ Å}^2$ .

atoms is  $d = 2.88 \text{ Å}$ .

In the experiments an atomically clean Au(111) single crystal surface was prepared by repeated cycles of sputtering with  $1.5 \text{ keV Ar}^+$  ions followed by annealing to  $840 - 900 \text{ K}$ , until STM revealed a well-ordered herringbone ( $22 \times \sqrt{3}$ ) reconstruction.

### 4.1.3 Molecular imaging modes

Following deposition at a coverage below saturation of the first monolayer, the three species are observed to self-assemble into large (several hundred  $\text{Å}$  wide) monomolecular high islands (see Fig. 4.4a). The herringbone reconstruction of the Au(111) surface does not appear to be perturbed by the molecular adsorption, as the characteristic corrugation of the reconstruction clearly is observed to modulate the height of the adsorbed molecular overlayers, as shown in Fig. 4.4b.

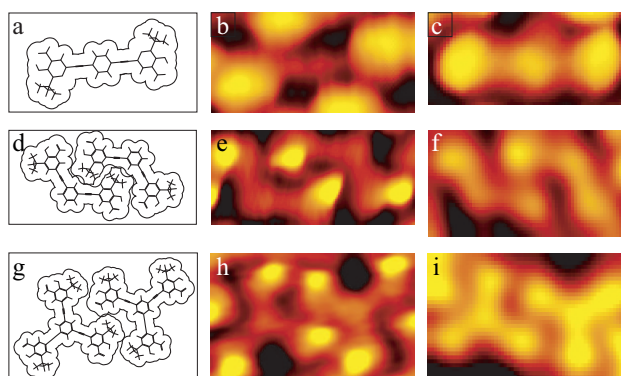


Figure 4.5: STM imaging for the three molecular species: left column: stick model of the molecules including their van-der-Waals radii. The molecular orientation and conformation is chosen to approximate the accompanying STM images. Center column: STM imaging mode characterized by prominent *tert*-butyl groups (*tert*-butyl mode). Right column: Imaging mode revealing the molecular backbone ( $\pi$ -mode). Top row: *para*-compound, center row: *meta*-compound, and bottom row: *threespoke*-compound.

The individual molecules are revealed in high resolution images acquired inside the islands as displayed in Fig. 4.5. Two primary STM imaging modes are observed: In the majority of images the topography is dominated by bright protrusions at the ends of the molecules (Fig. 4.5b,e,h). These protrusions which are attributed to the *tert*-butyl groups in agreement with other studies [129, 137, 199] appear  $(2.40 \pm 0.02)$  Å high compared to the underlying surface and are positioned off-axis with respect to the ethynylene spokes, and they thus allow us to determine the molecular conformation.

An alternative imaging mode is observed where only the aromatic molecular backbone ( $\pi$ -system) is visible, revealing the characteristic shape of the molecule (Fig. 4.5c, 4.5f, 4.5i). We will refer to these two imaging modes as *tert*-butyl and  $\pi$ -system mode, respectively. Since we have not observed any correlation between specific tunneling parameters and appearance of the molecules, we attribute the two modes to different states of the STM tip, presumably caused by the attachment and detachment of molecules at the tip apex. [44] As displayed in Fig. 4.5, the  $\pi$ -system imaging mode clearly reveals that the molecules indeed adsorb with their backbone parallel to the surface.

#### 4.1.4 Data analysis

The unit cell of the observed molecular structure is defined by  $|\vec{a}_o|$ ,  $|\vec{b}_o|$ , the angle between  $\vec{b}_o$  and  $\vec{a}_o$ , and the angle between  $\vec{b}_o$  and the closest  $\langle 110 \rangle$ -direction, see Tab. 4.1. The uncertainty in measured angles and distances is estimated to be less than 5% resulting from dynamic distortions of the image caused by thermal drift and piezo creep and static distortions resulting from anisotropies in the scanner tube. Consequently, the STM data alone does not allow us to unambiguously determine whether an overlayer

Com- pound	Structure	$ \vec{a}_o $ [Å]	$ \vec{b}_o $ [Å]	$\angle \vec{b}_o, \vec{a}_o$ [°]	$\angle \vec{b}_o, \langle 110 \rangle$ [°]	$N$	$A_{\text{mol}}$ [Å <sup>2</sup> ]	$A_{\text{vdW}}/A_{\text{mol}}$	Matrix
<b>Para</b>	Brick-wall	30	25	143	-23	2	230	0.80	$\begin{pmatrix} 3 & -9 \\ 4 & 10 \end{pmatrix}$
	Grid	26	36	135	-15	2	320	0.58	$\begin{pmatrix} 5 & -5 \\ 4 & 14 \end{pmatrix}$
<b>Meta</b>		30	29	88	-30	4	220	0.85	$\begin{pmatrix} 10 & 0 \\ 6 & 12 \end{pmatrix}$
<b>Three- spoke</b>	Hexagonal	27	26	120	19	2	310	0.88	$\begin{pmatrix} 11 & 4 \\ -4 & 7 \end{pmatrix}$
	Row	28	32	92	-3	2	440	0.63	$\begin{pmatrix} 11 & 4 \\ 1 & 11 \end{pmatrix}$
	Dense lad.	30	23	128	-5.0	2	260	0.96	$\begin{pmatrix} 10 & -2 \\ 0 & 8 \end{pmatrix}$
	Open lad.	39	24	125	0	2	390	0.70	$\begin{pmatrix} 13 & -1 \\ 0 & 8 \end{pmatrix}$

Table 4.1: Overview of the experimental results.  $|\vec{a}_o|$ ,  $|\vec{b}_o|$ : length of unit cell vectors as defined in Figs. 4.6, 4.10, 4.14, 4.17, 4.18, and 4.19;  $\angle \vec{b}_o, \vec{a}_o$ : angle between the lattice vectors;  $\angle \vec{b}_o, \langle 110 \rangle$ : angle between  $\vec{b}_o$  and the closest  $\langle 110 \rangle$ -direction;  $N$ : number of molecules per unit cell;  $A_{\text{mol}}$ : area occupied by one molecule;  $A_{\text{vdW}}/A_{\text{mol}}$ : packing density ; Matrix: best fit to the superstructure assuming commensurability.

is commensurate or incommensurate. The unit cell vectors were determined from the STM data and approximated by integer-value vectors<sup>6</sup> [27] .

$$\begin{pmatrix} \vec{a}_o \\ \vec{b}_o \end{pmatrix} = M \begin{pmatrix} \vec{a}_s \\ \vec{b}_s \end{pmatrix}. \quad (4.1)$$

As a measure for the molecular packing density we use  $A_{\text{vdW}}/A_{\text{mol}}$ , with  $A_{\text{mol}}$  defined as the area occupied by one molecule in the overlayer ( $A_{\text{mol}} = (\text{unit cell area})/N$  where  $N$  is the number of molecules in the unit cell) and  $A_{\text{vdW}}$  the projected vdW-area<sup>7</sup> (comp. Fig. 4.5a, d, and g;  $A_{\text{vdW}} = 274 \text{ Å}^2$  for the *threespoke* and  $185 \text{ Å}^2$  for the two-spoke compounds, assuming the whole conjugated system to be parallel to the surface).

The registry of the molecules with respect to the substrate could not be determined, since we were not able to obtain atomic resolution of the Au(111) substrate simultaneously with imaging the molecules. The molecules with  $120^\circ$  between the spokes (*meta*, *threespoke*) is thus assumed to adsorb with its center at a surface site with  $C_3$  symmetry (three-fold hollow site, on-top site) whereas the molecules with  $180^\circ$  between the spokes (*para*) is assumed to find sites with  $C_2$ -symmetry (bridge site, on-top site).

## 4.2 Para-compound

The *para*-compound dominantly forms two coexisting adsorption phases, referred to in the following as the brick-wall and grid structure, respectively (see also Fig. 4.4a).

<sup>6</sup>The contraction of the Au-lattice by 4% along one close-packed direction due to the herringbone-reconstruction does not seem to affect the adsorption structures and is neglected.

<sup>7</sup>The van-der-Waals radii were modelled with the program TITAN (1999), Wavefunction, Inc. and Schrödinger, Inc.



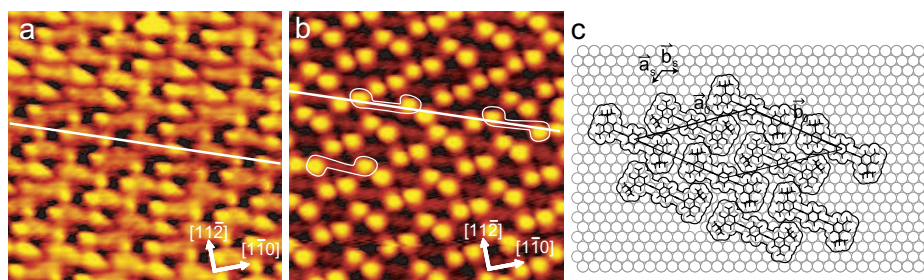


Figure 4.6: The brick-wall structure formed by the *para*-molecules. (a) STM image obtained in the  $\pi$ -system imaging mode (Size  $100 \times 100 \text{ \AA}^2$ ). (b) STM image in the *tert*-butyl imaging mode (size  $100 \times 100 \text{ \AA}^2$ ). (c) Tentative adsorption geometry.

### 4.2.1 Brick-wall structure

STM images of the brick-wall adsorption structure are shown in Fig. 4.6a and Fig. 4.6b. From the STM images obtained in the  $\pi$ -system imaging mode (Fig. 4.6a) the molecules are observed to arrange themselves into a regular tiling pattern in which all molecular backbones are parallel to each other. The molecules are aligned end-to-end in rows with adjacent rows being shifted relative to each other by half the repeat distance along the rows as for the stacking of bricks in a wall.

We assume molecules with  $180^\circ$  between the spokes to find sites with  $C_2$ -symmetry (ie. bridge sites or on-top sites). The molecular backbone forms an angle of  $\delta = 23^\circ$  with the  $\langle 110 \rangle$  direction. The requirement of placing both molecules in the unit cell with their centers at  $C_2$  sites can thus be fulfilled by placing the first molecule in an on-top site and the second molecule  $\frac{1}{2}\vec{a}_0$  away from it in a bridge site. This lead to the proposed structural model shown in Fig.4.6c, with the unit cell approximated as in table 4.1.

The packing density for the brick wall structure  $A_{\text{vdW}}/A_{\text{mol}} = 0.80$  (see table 4.1) shows that in this phase the molecules are packed rather efficiently, with the distance between the molecules matching a Van der Waals close-packing. The high symmetry direction of the overlayer does not coincide with a high-symmetry direction of the substrate, and the molecular overlayer in combination with the substrate therefore exhibits adsorption-induced organizational chirality.

When observed in the *tert*-butyl imaging mode (Fig. 4.6b), the brick-wall structure appears less ordered because the molecules assume different surface conformations placing the *tert*-butyl group differently with respect to the molecular backbone. Consequently, the structure is not truly periodic.

### Interactions

The observed structure can be rationalized by considering the conformers and intermolecular interaction motifs displayed in Fig. 4.7. The tables show probabilities,  $P$ , determined from analysis of STM images, of finding (i) the different surface conformers of the molecule, (ii) the different possible configurations for head-to-head intermolecu-

lar arrangements (*tert*-butyl groups on adjacent molecules either at the same side, *cis*, or opposite side, *trans*, of the line connecting two molecules), and (iii) the different possible configurations for side-to-side intermolecular arrangements (*tert*-butyl groups on adjacent molecules either pointing in the *same* or *opposite* directions).

The positions of the *tert*-butyl groups on neighboring molecules or within the same molecule are clearly correlated. The dominant intermolecular ordering motif is to have the *tert*-butyl groups lying *trans* where molecules meet head-to-head ( $P = 0.9 \pm 0.1$ ) and pointing to the *same* side where molecules meet side-to-side ( $P = 0.67 \pm 0.08$ ). This ordering gives rise to a structure such as the one in the region marked I on Fig. 4.7b and this idealized structure is the one depicted on the model in Fig. 4.6c. To realize these two preferred intermolecular configurations, the intramolecular conformation *must* be either LL or RR and alternating rows must consist of molecules entirely in the LL/RR conformation, respectively. This suggests that the preference for RR/LL intramolecular conformations ( $P = 0.69 \pm 0.03$ ) as opposed to RL/LR ( $P = 0.31 \pm 0.02$ ) results from the specific tiling pattern and inter-molecular interactions rather than from intramolecular interactions between the two ends of a given molecule (which are spaced far apart compared to the distance to adjacent molecules). A significant proportion ( $P = 0.33 \pm 0.08$ ) of the side-to-side interactions have the *tert*-butyl groups pointing in *opposite* directions, giving rise to structures as that in the region marked II on Fig. 4.7b. The minority population of molecules in the RL/LR conformation results from this type of structure.

The observed favored and unfavored end-group ordering along the rows (*trans* and *cis*) and between the rows (*same* and *opposite*) must result from interactions between the end-groups and the surrounding molecules. By assuming a Boltzmann distribution ( $\frac{N_{\text{uf}}}{N_{\text{f}}} = \exp(-\frac{\Delta E}{k_{\text{B}}T})$ ) the energy difference,  $\Delta E$ , between the favored and unfavored end-group arrangement can be estimated by the number,  $N_{\text{f}}(N_{\text{uf}})$  of end-groups having a favored(unfavored) orientation. Statistical analysis of several hundred molecules gives 93% *trans* head-to-head arrangements at 197 K and 58% end-groups with *same* side-to-side arrangement at 191 K. The energy difference resulting in the favoured/unfavoured *trans/cis* arrangement along the rows is thus 0.04 eV, whereas the energy difference directing the *same/opposite* arrangement between molecules in adjacent rows is only  $\sim 0.005$  eV.

### Chiral switching

From time-lapse sequences of STM images we find that the bright protrusions ascribed to *tert*-butyl groups occasionally change position from one side of the molecular backbone to the other. Such shifts are illustrated in Fig. 4.8a by superimposing two time-separated STM images of the same portion of the surface. The images have been coloured blue and orange, respectively, such that stationary protrusions appear grey, and blue (orange) indicates initial (final) positions of protrusions that have moved. On a given molecule, only one *tert*-butyl group at a time changes position. We therefore interpret the observed shifts as resulting from an intra-molecular conformational change in which one of the phenyl end-groups rotates around the axis of the ethynylene spoke, transferring the *tert*-butyl group from one side of the molecular axis to the other. A small number of events in which the *tert*-butyl groups at both ends of a molecule change

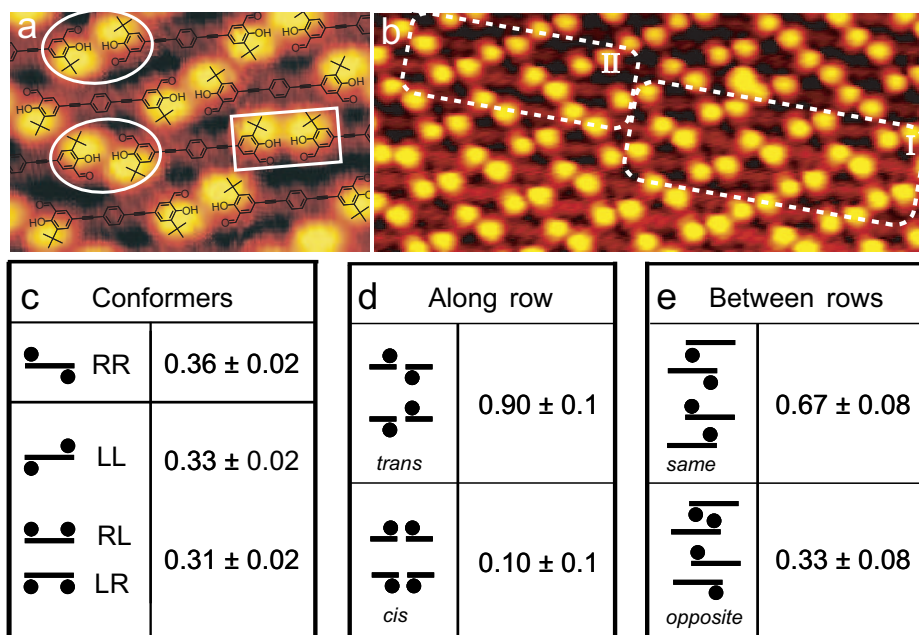


Figure 4.7: Interactions in the brick-wall structure. (a) Schematic model of the brick-wall adsorption structure superimposed on an STM image. The *cis* and *trans* arrangements for endgroups meeting head-to-head are indicated by a rectangles and ellipses, respectively. (b) STM image with a marked defect free (I) and defect rich (II) region. (c-e) Observed molecular conformers and intermolecular arrangements. Lines and circles indicate molecular backbones and *tert*-butyl groups, respectively.

position between consecutive images can be explained as uncorrelated, successive flips of the two molecular end-groups. This spontaneous flipping process implies that the molecules are not completely stereochemically fixed by the substrate, but can change between the different surface conformers, specifically from chiral (RR/LL) to achiral (RL/LR) or vice versa by a rotation of one end-group or between the two chiral enantiomers by a consecutive rotation of both end-groups.

The rates of conformational switching are controlled by the potential-energy landscape experienced by the molecule, and rates from an unfavored to a favored end-group configuration are thus higher than rates from a favored to an unfavored configuration. To estimate the rates we consider a simplified model in which only the strong head-to-head *cis*-/*trans*- interaction is taken into account<sup>8</sup>. From the analysis of STM videos the rates  $\Gamma_{t \rightarrow c}$  and  $\Gamma_{c \rightarrow t}$  between the *trans* and *cis*-configuration can be determined by solving a set of differential equations. The input STM data directly determined from the STM-

<sup>8</sup>The potential-energy surface is also influenced by interactions between molecules in adjacent rows and intramolecular interactions between the two ends of a molecule, but these contributions are weaker, since they lead to less ordering.



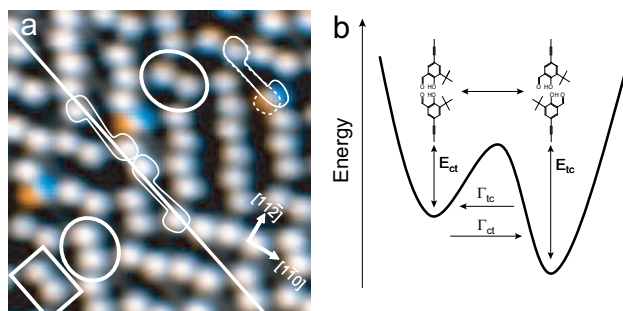


Figure 4.8: Conformational changes for the molecules in the brick-wall structure. (a) Overlay of two STM images taken with a time separation of 168 s (size  $90 \times 90 \text{ \AA}^2$ ,  $I_t = 0.4 \text{ nA}$ ,  $V_t = 1.96 \text{ V}$ ,  $T = 180 \text{ K}$ ). Blue (orange) indicates the initial (final) positions of *tert*-butyl groups that change position, whereas stationary groups appear grey. Two *cis*-*trans* (rightmost in image) flips are shown. Outlines of three molecules are indicated as well as stationary *cis* (rectangel) and *trans* (circles) arrangements of end-groups. (b) Schematic energy diagram of the *cis* and *trans* arrangements.

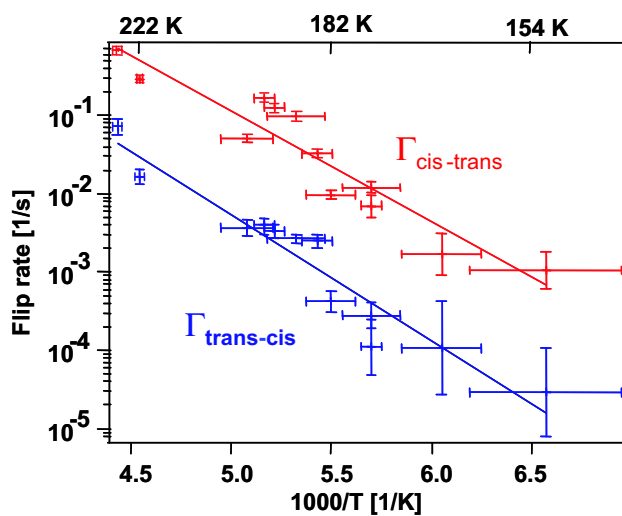


Figure 4.9: Arrhenius plot of the rate for *cis*-*trans* and *trans*-*cis* flips. Horizontal error bars indicate the temperature interval over which the STM data used to evaluate the respective datapoints were acquired. Vertical error bars represent one standard deviation.

movies is the time between two consecutive images, the number of flips  $N_{c \rightarrow t}$  ( $N_{t \rightarrow c}$ ) that change *cis*-pairs to *trans*-pairs (*trans*-pairs to *cis*-pairs) between two consecutive images and the population,  $N_c(0)$  ( $N_t(0)$ ), of *cis*-(*trans*)pairs counted in the first image.

The change in number of *cis*-pairs (*trans*-pairs),  $dN_c$  ( $dN_t$ ), in a short time interval is given by:

$$dN_{c(t)} = -\Gamma_{c \rightarrow t(t \rightarrow c)} N_{c(t)} dt + \Gamma_{t \rightarrow c(c \rightarrow t)} N_{t(c)} dt \quad (4.2)$$

where  $N = N_t + N_c$  is the total number of pairs, and  $N_c$  ( $N_t$ ) are the number of pairs in a *cis*- (*trans*-)configuration. The solutions consist of a steady-state and an exponentially decaying term:

$$N_{t(c)}(t) = \left( N_{t(c)}(0) - \frac{\Gamma_{c \rightarrow t(t \rightarrow c)}}{\Gamma_{c \rightarrow t} + \Gamma_{t \rightarrow c}} N \right) e^{-(\Gamma_{c \rightarrow t} + \Gamma_{t \rightarrow c})t} + \frac{\Gamma_{c \rightarrow t(t \rightarrow c)}}{\Gamma_{c \rightarrow t} + \Gamma_{t \rightarrow c}} N, \quad (4.3)$$

If only the population of *trans*-pairs in an image is considered (ie.  $N = N_t(0)$ ,  $N_c(0) = 0$ ), the above solutions give the number of *trans*-pairs that have converted to *cis*-pairs,  $N_{t \rightarrow c}$ , after the time  $t$  at given switching rates. By symmetry, we can find the number of *cis*-pairs that during time  $t$  will be changed to *trans*-pairs,  $N_{c \rightarrow t}$  by considering the original population of *cis*-pairs (ie.  $N = N_c(0)$ ,  $N_t(0) = 0$ ):

$$N_{t \rightarrow c(c \rightarrow t)}(t) = -\frac{\Gamma_{t \rightarrow c(c \rightarrow t)}}{\Gamma_{t \rightarrow c} + \Gamma_{c \rightarrow t}} N_{t(c)}(0) e^{-(\Gamma_{t \rightarrow c} + \Gamma_{c \rightarrow t})t} + \frac{\Gamma_{t \rightarrow c(c \rightarrow t)}}{\Gamma_{t \rightarrow c} + \Gamma_{c \rightarrow t}} N_{t(c)}(0) \quad (4.4)$$

From the equations in (4.4) we can find the corresponding switching rates,  $\Gamma_{t \rightarrow c}$  and  $\Gamma_{c \rightarrow t}$ :

$$\Gamma_{t \rightarrow c(c \rightarrow t)} = -\frac{N_{t \rightarrow c(c \rightarrow t)}}{N_{t(c)}(0)} \frac{\ln \left( 1 - \frac{N_{c \rightarrow t}}{N_c(0)} - \frac{N_{t \rightarrow c}}{N_t(0)} \right)}{\left( \frac{N_{c \rightarrow t}}{N_c(0)} + \frac{N_{t \rightarrow c}}{N_t(0)} \right) t} \quad (4.5)$$

The above deduction of the flipping rates from coupled differential equations takes into account the occurrence of multiple flips and areas with a non-equilibrium *cis/trans* population observed in the movies.

Rates determined from the analysis of STM videos acquired at a range of sample temperatures between 140 and 230 K are plotted in Fig. 4.9. The *cis-trans* rates indeed occur with a higher rate than *trans-cis*. Some of the scatter in the data results from the less strong side-to-side interactions between molecules in adjacent rows which depend on the local area imaged in a given STM movie. From fit to the Arrhenius form,  $\Gamma = \nu \exp(-E/k_B T)$ , where  $\nu$  is the pre-factor,  $E$  the activation energy,  $k_B$  the Boltzmann constant and  $T$  the temperature, we find  $E_{\text{trans} \rightarrow \text{cis}} = (0.32 \pm 0.03)$  eV and  $E_{\text{cis} \rightarrow \text{trans}} = (0.28 \pm 0.03)$  eV, consistent with the determined energy difference between *cis* and *trans*-pairs of 0.04 eV. The pre-factors  $\nu_{\text{trans} \rightarrow \text{cis}} = 10^{5.8 \pm 0.8} s^{-1}$  and  $\nu_{\text{cis} \rightarrow \text{trans}} = 10^{6.1 \pm 0.8} s^{-1}$  are considerably smaller than the standard  $k_B T/h \sim 10^{12} s^{-1}$  found for

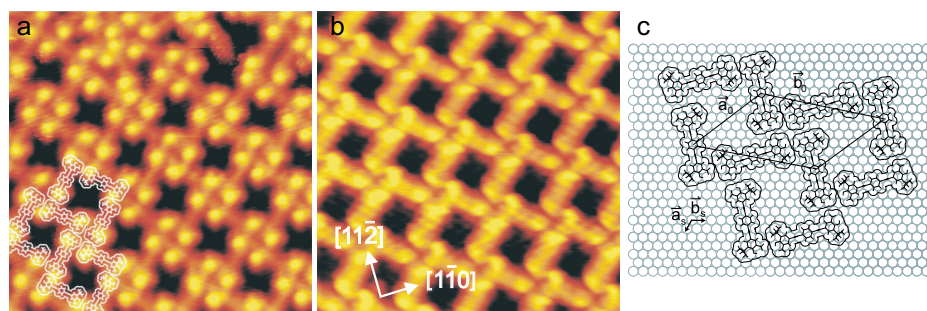


Figure 4.10: The nanogrid phase formed by the *para*-compound. STM images in (a) the *tert*-butyl mode with superimposed structural model, and (b)  $\pi$ -system mode (sizes  $140 \times 140 \text{ \AA}^2$ ). (c) Tentative adsorption geometry

other activated processes on surfaces, such as diffusion [106, 111, 113]. This might be related to a lowering of the entropy in the transition state caused by a confinement of molecular degrees of freedom.

#### 4.2.2 Grid structure

The second phase exhibited by the *para*-molecule is the grid structure shown in the STM images of Fig. 4.10a and b, depicting the structure in the *tert*-butyl and  $\pi$ -system imaging modes, respectively. The primary structural motif is a windmill-like arrangement of four molecules joined in a common node. Each molecule connects two such adjacent nodes producing an extended, highly ordered network with openings bounded by four molecules. For the parameters of the unit cell see Tab. 4.1. The grid structure is considerably more open than the brick-wall phase discussed above ( $A_{\text{vdW}}/A_{\text{mol}} = 0.58$ ). Since the molecules are not oriented along high-symmetry directions of the substrate, the molecular overlayer in combination with the substrate exhibits adsorption-induced chirality.

The two molecules in the unit cell are not equivalent, since one has  $\delta = -11^\circ$  and the other has  $\delta = 25^\circ$ . The enclosed angle of the rhombic holes in the structure is thus  $96^\circ$  ( $11^\circ + 60^\circ + 25^\circ$ ). Both molecules can be placed at an on-top site if the vector between them is  $\frac{1}{2}\vec{b}_0$ . This unit cell is depicted in Fig. 4.10c. Given the uncertainty ( $\sim 5\%$ ) in our measurements, it is possible that the molecules with  $\delta = 25^\circ$  in the grid phase has an identical adsorption geometry to the molecules in the brick-wall phase, where  $\delta = 23^\circ$  was determined.

The orientation of the *tert*-butyl groups is completely ordered in the grid phase. As seen from Fig. 4.11, the *tert*-butyl group always points away from the central node of the wind-mill motif. The grid phase is thus truly periodic, in contrast to the brick-wall structure which only showed periodicity in the tiling of the molecular backbones. The tiling pattern in the grid phase is chiral since the central wind-mill motif can be constructed with two opposing rotational directions. (The two domains shown in Fig. 4.11

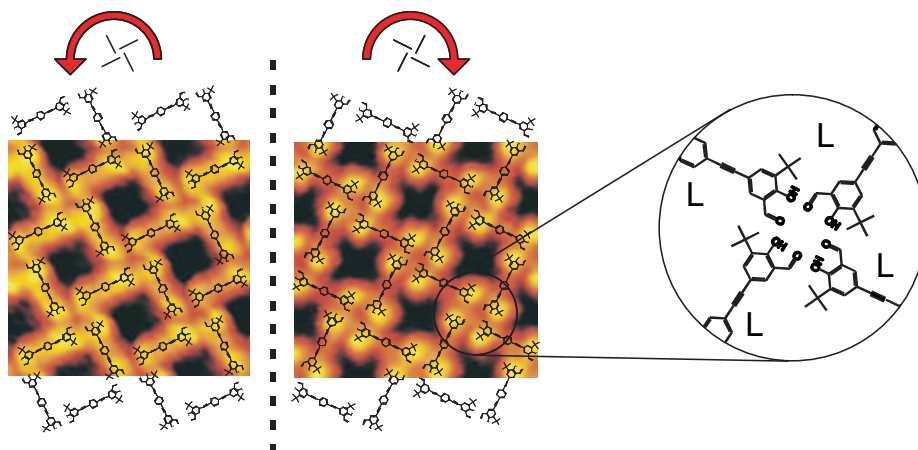


Figure 4.11: STM images with schematic models of the grid structure showing two domains of opposite chirality. The zoom-in on a structural node illustrates the correlation between the tiling pattern and the molecular chirality, leading to homochiral domains consisting exclusively of RR or LL-conformers.

have opposite sense of rotation for the windmill motif). The chirality of the surface conformers participating in the structure is completely correlated with the chirality of the backbone tiling: In order for the *tert*-butyl groups to point away from the central node, only LL conformers are found in the chiral domain shown in Fig. 4.10a to the left and only RR conformers participate in the domain of opposite chirality shown to the right. The structure thus shows perfect ordering of the RR/LL enantiomers into enantiopure domains and the non-chiral RL/LR conformers do not participate.

### Interactions

Compared to the brick-wall phase, the grid phase has a lower packing density and shows a higher degree of conformational order for the participating molecules. This points towards the existence of a directional intermolecular interaction compensating for the loss of vdW-intermolecular interaction resulting from the reduced packing density. We speculate that the molecular arrangement in the nodes of the grid structure facilitates the formation of an intermolecular hydrogen bonding network connecting hydroxyl and aldehyde groups on neighboring molecules. This possibility has been investigated by theoretical modelling and experimentally by modifications of the functional groups of the *para*-compound [200]. In order to keep this thesis at a sensible length results from this investigation will not be discussed further.

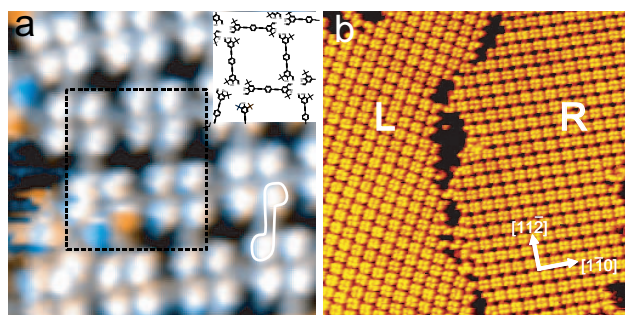


Figure 4.12: Accommodation by conformational change. (a) Overlay of two STM images visualizing the accommodation of an RL conformer at the boundary of an RR domain by a molecular conformational change (size  $110 \times 110 \text{ \AA}^2$ ,  $I_t = 0.66 \text{ nA}$ ,  $V_t = 1.25 \text{ V}$ , time separation 19 s). Inset: the molecular structure in the area marked by a dashed square, including initial (blue) and final (orange) positions of the *tert*-butyl group that moves. (b) Large-scale STM image showing the boundary between two homochiral domains of opposite chirality (size  $500 \times 500 \text{ \AA}^2$ ).

### Accommodation

Due to the strong binding in the nodes of the network the molecules in the grid structure were only observed to switch conformation at the island edges at the imaging temperature. Figure 4.12a shows an overlay of two time-separated STM images acquired at the edge of a homochiral domain consisting of RR conformers. In the first image (blue) an achiral RL conformer, coming from the lattice gas at the left side of the image, has attached itself to the edge, and in the second image (orange) a conformational change has occurred, switching this molecule to the chiral RR conformer, enabling it to fit into the structure. This flip is estimated to occur with a rate comparable to the rate observed for molecules in the brick-wall phase, although the molecule is situated in a different environment.

The ability to switch chirality by performing one or more conformational changes enables the molecules to accommodate to the chiral template found at the edge of the island and incorporate themselves into homochiral domains. Such an accommodation mechanism based on the combination of chiral recognition and conformational readjustment results in an effective pathway towards chiral segregation into homochiral networks.

### 4.2.3 DFT calculations

To illuminate the dynamics of the conformational change, modelling<sup>9</sup> based on density functional theory<sup>10</sup> has been performed. Calculations for the entire molecule on the Au

<sup>9</sup>All calculations in this chapter were performed by Eva Rauls and Bjørk Hammer.

<sup>10</sup>In the calculations the plane-wave-based DACAPO code [162, 163] with PW91 exchange, energy cutoff of 26 Ryd and periodic boundary conditions were applied.

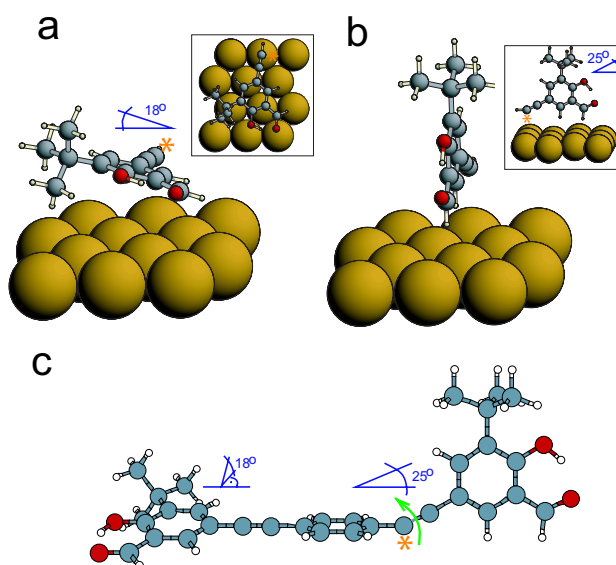


Figure 4.13: Structures from theoretical modelling. (a) Optimum adsorption geometry for the molecular fragment. The carbon atom marked by an asterisk has been saturated by a hydrogen atom. Inset: top view. (b) Optimum transition-state geometry. Inset: side view. (c) Free molecule in a strained geometry with the backbone bent by 25° as suggested from (b). (Note that not all gold atoms in the supercell used are shown in (a) and (b).)

surface are computationally unfeasible and hence only the end-portion of the molecule was modelled<sup>11</sup> (Fig. 4.13a). Since the two endgroups of a given molecule are observed to flip independently of each other, we assume that part of the molecule stays bound to the substrate during the conformational change. In the calculations the influence from this part of the molecule on the modelled end-portion is taken into account by constraining the carbon atom marked by an asterisk to be at the distance from the surface found to be optimum for a benzene molecule (3.48 Å). In the optimum adsorption configuration (Fig. 4.13a), the presence of the bulky *tert*-butyl group leads to an 18° tilting of the benzene ring in the end-portion, while in the transition state (Fig. 4.13b) the benzene ring is rotated to bring the *tert*-butyl group away from the surface. The energy difference between the two configurations is 0.20 eV.

In the transition state, the molecular axis is tilted by 25° away from the surface (see inset in Fig. 4.13b) corresponding to a pronounced bending of the molecular backbone. To estimate the associated energy cost, the entire free molecule in similarly bent

<sup>11</sup>The structures were modelled in a three-layer slab of the unreconstructed Au(111) surface using a 3 × 3 unit cell. Test calculations with a 3 × 4 unit cell, that is, increased intermolecular distance between the periodic images, resulted in 0.003 eV higher binding energies, showing that the smaller unit cell already yields converged values.



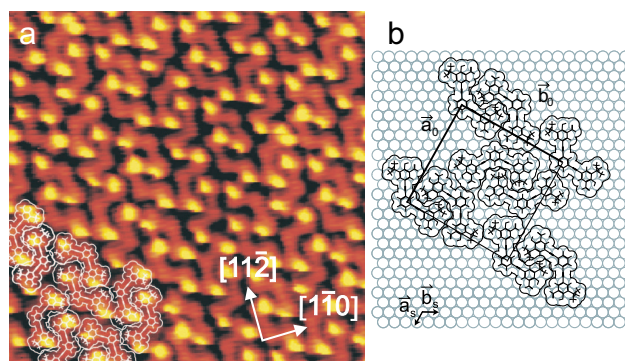




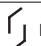
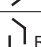


Figure 4.14: Adsorption structure formed by the *meta*-molecule. (a) STM image ( $120 \times 120 \text{ \AA}^2$ ). (b) Tentative adsorption geometry.







(Fig. 4.13c) and non-bent (not shown) transition state configurations was modelled<sup>12</sup> and we found an energy difference between the two of 0.17 eV. In conclusion, the net energy barrier for the conformational change is therefore estimated from the calculations to be 0.37 eV, comparable to the experimental value, and is comprised of two approximately equal contributions arising from a reduced molecule-surface interaction and bending strain in the molecule, respectively. For the free molecule, in comparison, the barrier towards rotation around the ethynylene spoke is found to be only 0.037 eV.

#### 4.2.4 Discussion

The ability to switch chirality by performing one or more conformational changes enables the *para*-compounds to accommodate to the chiral template found at the edge of the island and to incorporate themselves into homochiral domains. The chiral segregation [11, 35, 66] on surfaces of racemic mixtures formed from adsorbed prochiral compounds has been ascribed to lateral mass transport, sometimes over mesoscopic distances, in combination with chiral recognition/selection at the perimeters of enantiopure domains. The accommodation mechanism described here is a more effective channel towards chiral segregation on surfaces. The formation of homochiral adsorbate layer may be accomplished by seeding [13, 61] the surface with an appropriate chiral template compound or by adsorbing the molecules on a chiral metal surface [54].

<b>a</b>		RR 	LL 	RL 	LR 
 LL rows		<0.01	$0.78 \pm 0.08$	$0.06 \pm 0.02$	$0.16 \pm 0.04$
 RR rows		$0.67 \pm 0.08$	$0.05 \pm 0.02$	$0.05 \pm 0.02$	$0.22 \pm 0.04$

<b>b</b>	Within pairs	 towards	 same	 away
		$0.80 \pm 0.09$	$0.20 \pm 0.05$	<0.01
	Between pairs	 towards	 same	 away
		$0.58 \pm 0.08$	$0.42 \pm 0.07$	<0.01





<b>c</b> LL row				
LL	LR	RL	RR	
				

Figure 4.15: Molecular arrangements for the *meta*-molecule. (a) Distribution of different surface conformers in rows dominated by LL and RR conformers, respectively. (b) Distribution of relative orientations of *tert*-butyl groups on neighboring molecules. Top row: within the nested pairs, bottom row: between the nested pairs along the molecular rows (the numbers are derived from analysis of both chiralities of the tiling motif). (c) Illustration of the consequence of introducing other surface conformers (centermost molecule) into rows consisting of LL molecules. The circles indicate interactions that are unfavorable due to steric hindrance and/or loss of vdW-interaction

## 4.3 Meta and threespoke-compound

### 4.3.1 Meta-compound

The *meta*-compound exhibits only one distinct adsorption phase, displayed in the STM image of Fig. 4.14a (in which both molecular backbones and *tert*-butyl groups are readily recognized), see Tab. 4.1 for details. The dominant packing motif is a pair of molecules, rotated by  $180^\circ$  with respect to each other and oriented with an ethynylene spoke of each pointing toward the vertex formed from the two spokes of the other. These pairs stack into rows running along the  $\langle 112 \rangle$  direction. If the molecules are tentatively placed with their centers on on-top-sites with  $C_3$  symmetry, the adsorption geometries depicted in Fig. 4.14b are obtained.

The molecular pair-motif is chiral and can be realized in two enantiomeric forms as shown in Fig. 4.15a. All pairs within a given row are of the same chirality, and the rows alternate between the two possible enantiomeric forms. The unit cell is rectangular and contains two glide line symmetry elements connecting the molecular pair placed in the unit cell with the pairs of opposite chirality placed at the corners of the cell. The overall tiling pattern is thus *not* chiral despite being formed from chiral sub-units. The packing density is  $A_{\text{vdW}}/A_{\text{mol}} = 0.85$ .

The probabilities of finding different conformers and intermolecular configurations

<sup>12</sup>Calculations for the entire free molecule were performed with the self-consistent charge density-functional-based tight-binding (SCC-DFTB) method [201]



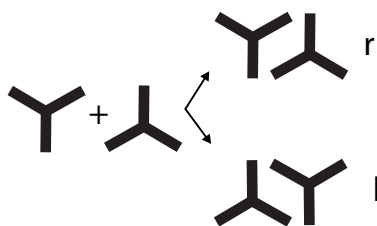


Figure 4.16: Chiral interaction motif observed for all four packing patterns. One molecule of the unit cell can be either positioned to the right ("r") or to the left ("l") of the spokes of the other molecule, as seen from the central benzene ring.

have been investigated. The analysis with respect to surface conformers has been done separately for the two types of rows with opposite chirality in the pair-motif (Fig. 4.15a).

The predominant conformers are the chiral LL/RR species which are observed with a probability of  $P = 0.7 \pm 0.1$ . The two types of rows are each strongly dominated by one of the two chiral conformers: The probability of finding an RR/LL conformer in a row dominated by LL/RR conformers is only a few percent. Of the two non-chiral conformers (RL and LR), the LR conformer is dominant in both types of rows. Probabilities,  $P$ , for different intermolecular configurations, reflecting possible nearest neighbor intermolecular interactions, are summarized in the table shown in Fig. 4.15b. Both within the molecular pairs and between them (along the direction of the molecular rows), there is a preference for having *tert*-butyl groups on neighboring molecules oriented towards each other ( $P = 0.80 \pm 0.09$  within pairs and  $P = 0.58 \pm 0.08$  between pairs). These predominant orientations of the *tert*-butyl groups favor RR/LL species depending upon the chirality of the tiling motif, as illustrated in Fig. 4.15c. When a deviating conformer is inserted into a row formed from LL conformers, non-preferential interaction configurations result to either one (LR or RL) or both (RR) neighbors, explaining the ordering of probabilities for finding the different conformers in LL rows.

### 4.3.2 Threespoke-compound

The *threespoke* compound is found to aggregate into four different adsorption structures. We will refer to these structures as hexagonal (Fig. 4.17), row (Fig. 4.18), dense ladder (Fig. 4.19a,c), and open ladder (Fig. 4.19b,d), respectively (see also Tab. 4.1). We could not attribute the formation of one specific phase to a special preparation or imaging condition, rather, the structures seem to coexist for a wide range of parameters.

#### Adsorption structures

The *threespoke* compound adsorbs with its spokes along high symmetry  $[11\bar{2}]$  directions. This can be realized in two distinct ways, related by a  $60^\circ$  rotation of the molecule. We will refer to these orientations as "up" and "down", respectively. Two molecules of up

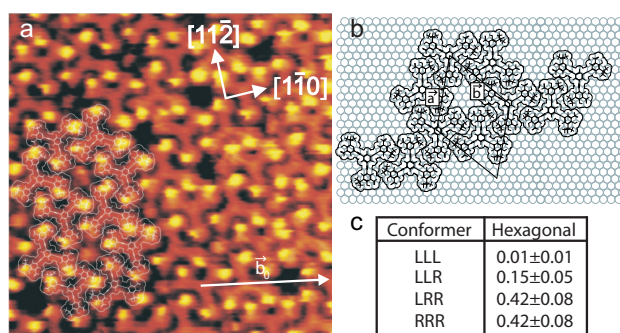


Figure 4.17: Hexagonal structure. (a) STM image (size  $120 \times 120 \text{ \AA}^2$ ). (b) Tentative adsorption geometry. (c) Distribution of surface conformers found in domains with 'r'-tiling. In mirror domains the inverse distribution is found.

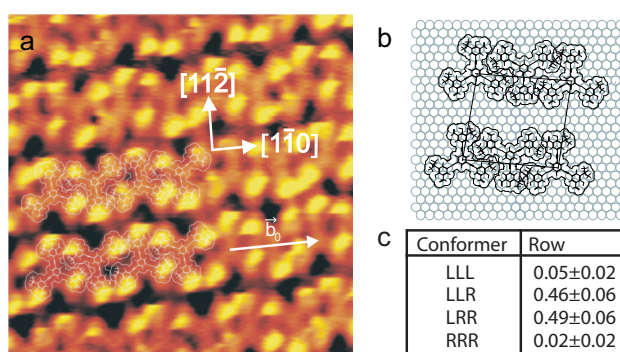


Figure 4.18: Row structure. (a) STM image (size  $120 \times 120 \text{ \AA}^2$ ). (b) Tentative adsorption geometry. (c) Distribution of surface conformers.

and down orientation close-pack with an end-group of one molecule lying in the vertex formed by two arms of the other (comp. Fig. 4.16). This arrangement is chiral, and can be formed in two distinct ways, termed "r" (right) and "l" (left). This motif is somewhat similar to the one adopted by the *meta*-compound.

In the hexagonal structure, the molecules are arranged into six-membered rings, each molecule belonging to three such interlocked rings. As one proceeds along the ring perimeter the molecules alternate between up and down. All spokes of the molecules participate in the described chiral interaction motif. In the domain shown in Fig. 4.17a, all these motifs are of r chirality. The molecular organization is thus chiral in itself. In the corresponding mirror domain (not shown), all interaction motifs are of the l type. The unit cell and a possible adsorption geometry for the molecules on the Au(111) surface with the central benzene ring on an on-top site, are shown in Fig. 4.17b.

In the row structure, Fig. 4.18a, the molecules are arranged into rows oriented slightly off the  $[1\bar{1}0]$  direction, therefore the structure has organizational chirality. Proceed-

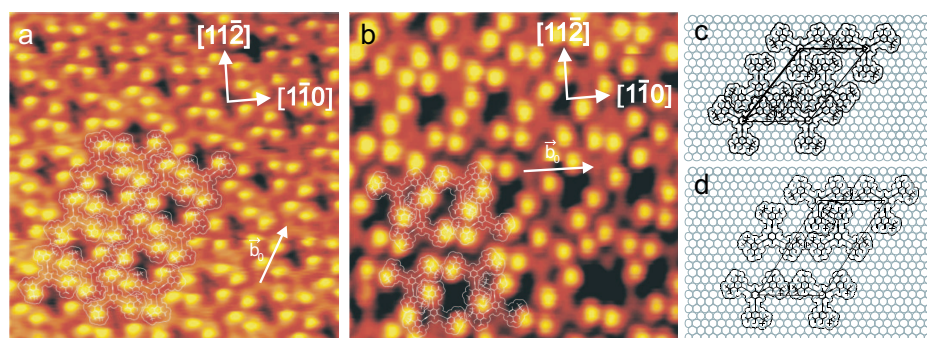


Figure 4.19: Dense ladder structure: (a) STM image (size  $120 \times 120 \text{ \AA}^2$ ) and (c) tentative adsorption geometry. Open ladder structure (b) STM image (size  $120 \times 120 \text{ \AA}^2$ ) and (d) tentative adsorption geometry.

ding along a row, the molecules alternate between up and down. Two spokes on each molecule participate in the chiral interaction motif while the last points towards the edge of the row. The interaction motifs alternate between the *r* and *l* chirality. A tentative adsorption model with the central benzene ring on an on-top site is seen in Fig. 4.18b.

The dense and open ladder structures (Fig. 4.19a and Fig. 4.19b) are closely related. In both structures, pairs of molecules, arranged in the chiral interaction motif, stack along the  $\langle 110 \rangle$  direction by joining sideways (best appreciated in Fig. 4.19b). The resulting "ladder-like" structures are spaced somewhat apart in the open ladder structure while they are closely packed in the dense ladder structure. The chiral interaction motif is assumed for one/two spoke(s) per molecule in the open/dense ladder structures, respectively. The interaction motifs are exclusively of one chirality (*l* for both domains shown in Fig. 4.19), and the structures are thus chiral. Suggested adsorption geometries for the two structures with the central benzene rings on on-top-sites are shown in Fig. 4.19c-d while unit cells and packing densities are listed in Table 4.1.

### Surface conformers

Also for the *threespoke*-compound, the orientation of the salicylaldehyde moieties presents an additional level of organization compared to the molecular tiling patterns. The probabilities of finding the different molecular surface conformers in the hexagonal and row structures have been evaluated from the STM images. In the table in Fig. 4.17c the distribution of surface conformers is seen. The numbers correspond to hexagonal domains with the *r* chirality of the tiling pattern (as the one shown in Fig. 4.17a). The distribution is clearly asymmetric, favoring the *R* orientation<sup>13</sup>. The distribution for the row structure (Fig. 4.18c) is symmetric within the error bars, with the RRR/LLL conformers occurring with a somewhat lower probability than expected for a random distribution.

<sup>13</sup>Domains with the opposite "*l*" chirality of the tiling pattern favor the *L* orientation (not shown).

The preference for different surface conformers is thus strongly affected by the particular tiling pattern assumed by the molecules. Both the hexagonal and row structures are dominated by the chiral packing motif with terminal groups positioned in the vertex of a neighboring molecule. In this arrangement the end-group can be oriented with its *tert*-butyl group pointing either towards or away from the vertex. From an analysis of the STM images, we find the *tert*-butyl group to predominantly point towards the neighboring vertex, which occurs with probabilities of  $0.75 \pm 0.07$  and  $0.72 \pm 0.05$  for the hexagonal and row structures, respectively. In the hexagonal structure, where only intermolecular packing of the r-type occurs (in the analyzed domain), this requires the molecules to predominantly assume the R rotational orientation of the end-group. In the row structure, on the other hand, the two end-groups per molecule that participate in the chiral packing motif are in vertices of r and l orientation, respectively, while the third end-group resides in a fairly symmetric environment. As a result, the assumed molecular conformers become symmetric with respect to R/L orientation, and RRR/LLL conformers become less likely.

The correlation between tiling pattern and adopted molecular conformations is more complicated for the two ladder structures and has not been analyzed in detail.

### 4.3.3 Interactions

The packing density of the structures formed by the *meta* and *threespoke*-compounds fits a van der Waals close-packing. That the observed structures do not favor intermolecular hydrogen bond formation<sup>14</sup> may be caused by the molecules having an intramolecular hydrogen bond ( $E_b = 0.34$  eV/group [129]) between the aldehyde and hydroxyl groups which has to be broken before intermolecular hydrogen bonds can form. Despite the similarity of the molecules, the intermolecular separations are not always identical; the *meta*-compound shows the same local geometry inside the pairs as the open ladder structure and the hexagonal phase is similar to the row phase. This indicates that the intermolecular forces stabilizing the structures vary slightly.

In all the structures formed by the *meta* and *threespoke*-compounds we found a certain order of the head-groups, presumably directed by the potential energy landscape felt by the molecules. Since each end-group can be oriented in two ways with respect to the surroundings, as the *tert*-butyl group is positioned either to the right (R) or to the left (L) when observed along the spoke from the central benzene ring (see Fig. 4.2) favored and unfavored end-group orientations result. This is similar to the brick-wall structure for the *para*-compound. By assuming Boltzmann distributions the energy gain associated with the preferred arrangement in which *tert*-butyl groups on the molecular spokes are oriented towards the vertex a neighboring molecule found for both *meta*-molecule and the row and hexagonal structure of the *threespoke*-molecules can be estimated. Here we find the optimum arrangement to be between 0.014 and 0.020 eV lower in energy than the arrangement in which the end-group is oriented oppositely. The other observed interaction motifs yield similar energies. Consequently, the potential-energy landscape controlling the conformational order of the *meta* and *threespoke*-molecules has only

<sup>14</sup>The original intention behind the design of the compounds was to form molecular wires connected by intermolecular hydrogen bonds between the aldehyde and hydroxyl groups.

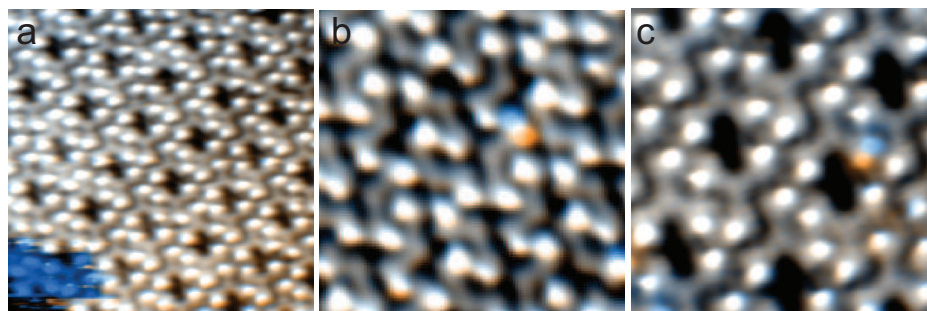


Figure 4.20: Dynamics of the molecules shown by overlay images where the initial/final image is color coded blue/orange. (a) STM images ( $150 \times 150 \text{ \AA}^2$ ) revealing *threespoke* molecules leaving the island. (b-c) STM images ( $70 \times 70 \text{ \AA}^2$ ) revealing conformational changes inside the islands for the *meta*-compound (b) and the *threespoke*-compound (c).

small variations and is similar to the interaction strengths observed in the brick-wall phase for the *para*-compound ( $0.005 - 0.05 \text{ eV}$ ).

#### 4.3.4 Molecular dynamics

As for the *para*-compound, the *meta* and *threespoke*-compounds form structures where there is a clear correlation between the chirality of the molecular tiling patterns and the conformation of the embedded surface conformers. The creation of order is also in these cases affected by dynamical processes, involving interchange of molecules between the structures and the lattice gas combined with conformational changes.

Dynamical phenomena for the *meta* and *threespoke*-compounds are revealed in the blue/orange color coded STM images shown in Fig. 4.20<sup>15</sup>. In Fig. 4.20 *threespoke*-molecules originally embedded in an island (blue) are seen to detach and diffuse into the lattice gas (orange) [116]. The networks thus interchange molecules with the lattice gas at the imaging temperatures of 140-170 K. As single molecules are never observed outside the condensed phases, the molecules in the 2D gas phase are assumed to be highly mobile.

By overlay images as the ones shown in Fig. 4.20b and 4.20c, we observe that the *meta* and *threespoke*-compounds also switch conformation spontaneously on the surface. The ability to switch conformation is thus a general phenomenon for this class of compounds<sup>16</sup>. The spontaneous switching implies that the molecules are not completely fixed by the substrate, but can change between the different surface conformers after adsorption. For all structures formed by the *threespoke*-molecule and the structure formed by the *meta*-molecule conformational changes have been observed in the interior of the domains at the imaging temperatures 140 – 170 K. The energy barriers for the *meta* and

<sup>15</sup>The first image is color coded blue and overlaid with the next image color coded orange.

<sup>16</sup>Conformational changes after adsorption have also been observed for a class of *para*-compounds with varying chemical end-groups [200].



*threespoke*-molecules are thus likely to be similar to the barrier of  $\sim 0.3$  eV found for the *para*-molecule, as all these compounds have been observed to switch conformation in the same temperature window.

The correlation between the tiling pattern of the structures and the conformation of the embedded molecules can be explained by an accommodation mechanism (similar to the mechanism described for the *para*-compound) in which conformational switching occurs after growth of the structures. Ultimately this results in an equilibrium distribution of surface conformers which is determined by the potential-energy landscape of the specific domain. A clear example is the asymmetry in the LLL/RRR and LLR/RRL distribution found for the hexagonal phase of the *threespoke*-compound caused by one spoke orientation (towards or away from the vertex) being energetically favored depending on the chirality of the tiling pattern (see Fig. 4.17).

To investigate whether growth occurs prior to conformational ordering, the *threespoke*-molecule was deposited onto a sample held at a low temperature of 95 K. The sample was subsequently slowly heated up during scanning in the STM. We observed that islands started growing at sample temperatures between 160 K and 165 K. In this temperature window the rate for the conformational switching is such that steady state can be reached within a few minutes. The two processes of aggregation and switching therefore happen simultaneously in these experiments.

The observed process of conformational switching may be general to a whole class of molecules that possess a rotational degree of freedom around a single bond which allows them to change their conformation even after adsorption. In addition to the molecules described in these studies, a candidate for such a process is for example 4-[trans-2-(pyrid-4-yl-vinyl)]-benzoic acid (PVBA) [11, 30].

## 4.4 Conclusion

In conclusion, the three studied molecules tend to arrange themselves into van der Waals close-packed structures mainly determined by the shape of the molecule. In the structures chiral ordering is observed both in the tiling pattern of the molecules and in the distribution of conformers. We find that the conformation of the embedded molecules is correlated with the arrangement of the tiling pattern and we find that the interactions directing this ordering are fairly weak, in the order of 0.005 - 0.05 eV. For one compound we observe a more open grid structure with complete conformational order, which we speculate may be due to more directional hydrogen bonding interactions between the functional groups. [200]

We observe that molecules at the island edges attach and detach. We therefore assume that the structures are in equilibrium with the lattice gas [116] and consequently even so with the other co-existing structures observed for the same compound. We find that all the studied molecules can switch their conformation after adsorption by a rotation around the molecular spokes and that the observed conformational ordering inside the domains is enhanced by dynamical changes in the molecular conformation upon incorporation of the molecules into the islands. We observe how molecules accommodate to the structures and change their conformation after or during attachment to reach the

state of highest binding energy. This accommodation procedure is effective as it reduces the mass transport compared to segregation procedures in which molecules reaching the islands only incorporate if they have the right conformation. In future studies [77] the formation of global homochiral domains may be realized by seeding [13,61] the surface with a chiral template compound or by adsorbing the molecules on a chiral template surface [54]. The potential ability to form such homochiral surface layers is of high interest to the field of heterogeneous asymmetric catalysis and even with respect to the understanding of the chiral asymmetry observed in nature.





## CHAPTER 5

---

### **An upright-standing oligo-phenylene-ethynylene**

---

The orientation of adsorbed molecules depends in general on the specific molecule-metal system. In this chapter a fourth member of the oligo-phenylene-ethynylene family is investigated, demonstrating that a change in molecular adsorption geometry from flat-lying to upright-standing can result solely from a change in molecular geometry, without any alterations to the molecular size and functional groups.

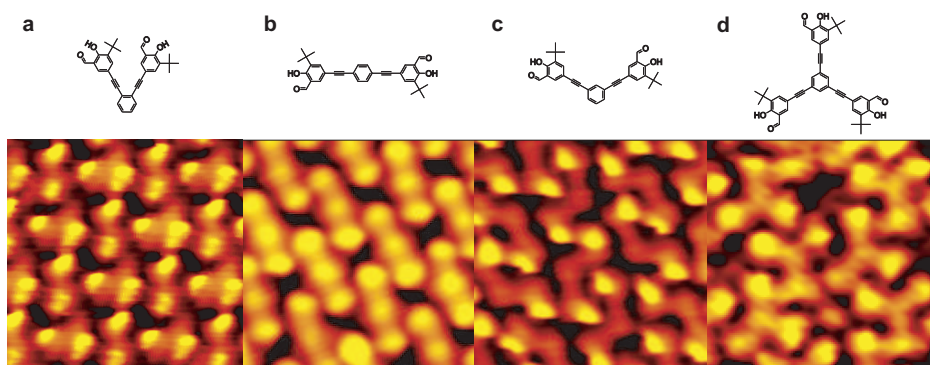


Figure 5.1: STM images (size  $50 \times 50 \text{ \AA}^2$ ) of the four chemically similar compounds with (a) *ortho*-, (b) *para*-, (c) *meta*- and (d) *threespoke*-configuration of the molecular spokes.

## 5.1 Introduction

The orientation of adsorbed molecules depends in general on the specific molecule-metal system [27]. Flat-lying adsorption geometries, which allow for large molecular footprints and strong interactions between the surface and the electronic system of the molecular backbone, have been observed both for aliphatic hydrocarbons [43] and for a large range of planar aromatic molecules such as pentacene [202], porphyrins [10], DNA bases [35, 38], PVBA [29], or oligo-phenylene-ethynylenes [22].

In contrast, upright-standing adsorption geometries typically occur for layers of molecules that contain functional groups with a high surface affinity, such as thiols [31, 32, 189, 203], pyridines [33], or carboxylic acids [34]. In those latter cases the closer packing allows for a higher density of interacting affinity groups which compensates for the loss in backbone-surface interaction. The balance between the two situations may depend both on surface coverage [31, 33] and molecular chain length [32].

In this chapter the last member of the oligo-phenylene-ethynylene family with an *ortho*-configuration of the molecular spokes is investigated (Fig. 5.1a). Whereas the compounds with the ethynylene spokes placed in a *para*-, *meta*- or *threespoke*-configuration exclusively form molecular adsorption structures built up of molecules with a nearly flat-lying adsorption geometry,<sup>1</sup> the *ortho*-compound surprisingly form structures with an upright adsorption orientation of the nucleated molecules. In Fig. 5.1 an overview of high-resolution STM images of the four geometric variants is given for completeness. Whereas the *para*-, *meta*- and *threespoke*-compounds are all visualized with their characteristic linear, bend and tripodal molecular shape expected for flat-lying molecules, the expected v-shape of the *ortho*-molecules is not found.

<sup>1</sup>DFT calculations yielded an  $18^\circ$  tilt angle of the outer benzene rings.

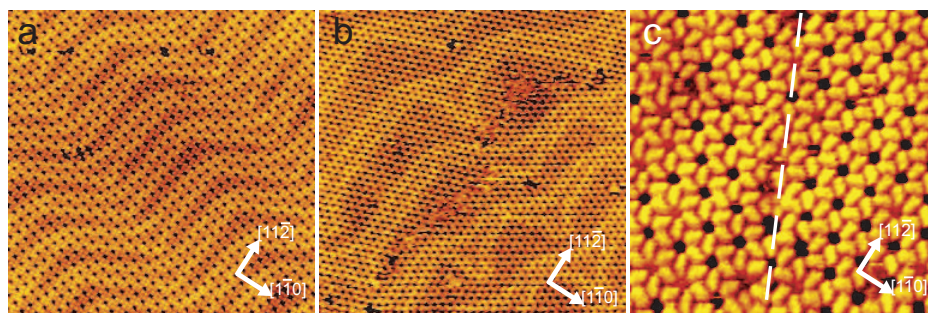


Figure 5.2: Large scale STM images (size  $500 \times 500 \text{ \AA}^2$ ) of (a) the rhombic phase ( $I_t = 0.87 \text{ nA}$ ,  $V_t = 1.25 \text{ V}$ ) and (b) the hexagonal phase ( $I_t = 0.86 \text{ nA}$ ,  $V_t = 1.43 \text{ V}$ ). c) STM image of the hexagonal phase with a boundary between two mirror domains (size  $170 \times 170 \text{ \AA}^2$ )

## 5.2 Adsorption structures

The *ortho*-compound (1,2-bis[(5-*tert*-butyl-3-formyl-4-hydroxy-phenyl)ethynyl]benzene) was sublimated onto the Au(111) sample under ultrahigh vacuum conditions from a heated glass crucible, and the STM measurements were performed at sample temperatures between 140-170 K. The sample preparation was thus similar to the sample preparation of the other family members. Upon deposition two co-existing adsorption phases were formed, termed the hexagonal and the rhombic structure, respectively. For both structures large self-assembled islands were observed (see Fig. 5.2) with the herringbone reconstruction of the underlying Au(111) substrate being visible through the molecular layer in the STM images.

As for the *para*-, *meta*- and *threespoke*-compounds, the *ortho*-compounds were imaged either in the  $\pi$ -system imaging mode revealing the aromatic backbone (eg. Fig. 5.3a) or in the *tert*-butyl imaging mode with bright protrusions attributed to *tert*-butyl groups (eg. Fig. 5.3b).

### 5.2.1 Hexagonal structure

Images of the hexagonal structure obtained in the  $\pi$ -system imaging mode and in the *tert*-butyl imaging mode are seen in Fig. 5.3. In the  $\pi$ -system imaging mode (Fig. 5.3a) individual molecules are revealed as crescent moon-like shapes, clearly different from the expected v-shape, with six molecules forming a chiral rosette motif. At the boundary between two chiral domains conformational mismatches lead to disorder (Fig. 5.2c).

The packing density given by the ratio between the estimated van der Waals footprint of the flat-lying molecule ( $A_{vdW}$ ) and the area occupied by a molecule in the experimentally observed structures ( $A_{mol}$ ) is  $A_{vdW}/A_{mol} = 1.5$ . The structure is thus packed more densely than anticipated for a structure containing flat-lying molecules.

The bright protrusions arising from the *tert*-butyl groups in Fig. 5.3b can unambigu-

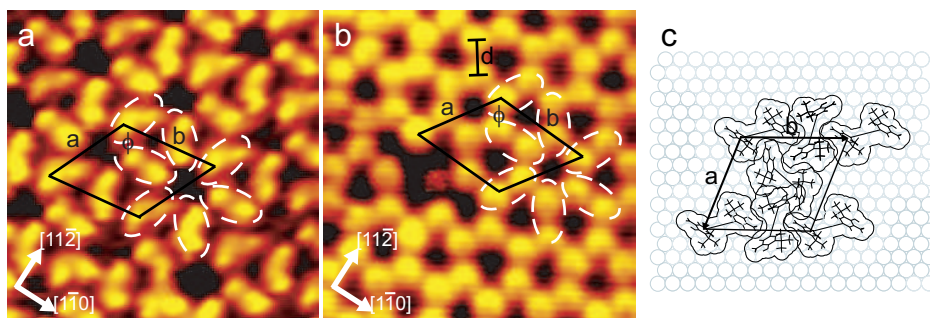


Figure 5.3: The hexagonal structure: (a-b) STM images (size  $70 \times 70 \text{ Å}^2$ ,  $I_t \sim 1 \text{ nA}$ ,  $V_t = 1.5 \text{ V}$ ) obtained in the  $\pi$ -system (a) and *tert*-butyl imaging mode (b). (c) Tentative adsorption model.

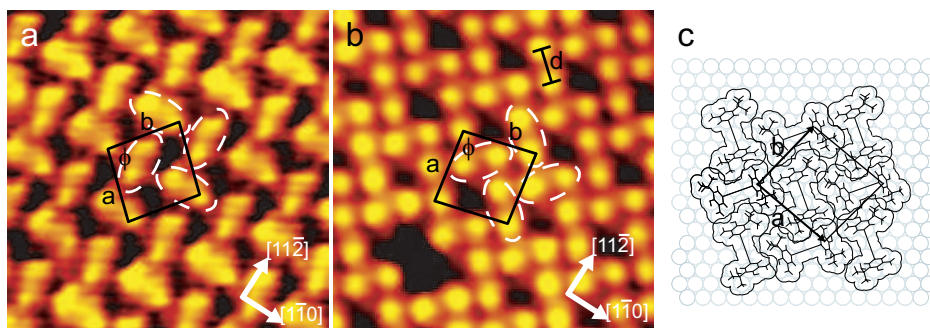


Figure 5.4: The rhombic structure: (a-b) STM images (size  $70 \times 70 \text{ Å}^2$ ,  $I_t \sim 1 \text{ nA}$ ,  $V_t = 1.5 \text{ V}$ ) obtained in the  $\pi$ -system (a) and *tert*-butyl imaging mode (b). (c) Tentative adsorption model.

ously be assigned to individual molecules by comparison to single-molecule vacancies in the structures. The distance,  $d$ , between the maxima for two protrusions belonging to the same molecule is found to be  $d = (7.3 \pm 0.5) \text{ Å}$ .

A nearly hexagonal unit cell ( $|a| = (19.6 \pm 1.0) \text{ Å}$ ,  $|b| = (22.3 \pm 1.1) \text{ Å}$ ,  $\phi = 121.1^\circ \pm 5.0^\circ$ ) containing three molecules can be assigned to the structure, as marked on the STM images in Figs. 5.3a and 5.3b. The hexagonal structure has a definite orientational relationship to the underlying substrate with an angle of  $-5.9^\circ \pm 5.0^\circ$  between the unit-cell vector,  $b$ , and the  $[1\bar{1}0]$  direction of the Au(111) surface. In Fig. 5.3c a tentative adsorption model is seen. In the model the backbones are assumed to be perpendicular to the substrate and the two outermost benzene rings to be parallel to each other. The central benzene ring is indicated as a short line due to the projection.

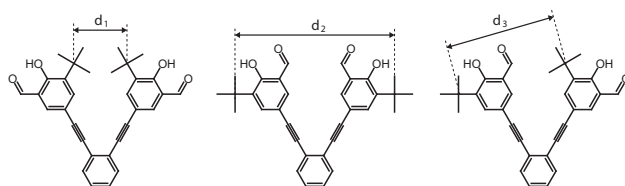


Figure 5.5: Schematic model of possible planar conformations with indicated distance,  $d$ , between the *tert*-butyl groups.

### 5.2.2 Rhombic structure

In the rhombic structure, four molecules join in a wind-mill type arrangement as marked on Figs. 5.4a and 5.4b. In the  $\pi$ -system imaging mode the molecules appear with a characteristic s-shape, again different from the anticipated v-shape. In the *tert*-butyl imaging mode the individual molecules are assigned to the bright protrusions from single molecule vacancies. The distance between the maxima for the two protrusions identifying a molecule is,  $d = (7.9 \pm 0.5) \text{ \AA}$ .

The unit cell (see Fig. 5.4) contains two molecules and is truly rhombic ( $|a| = (15.4 \pm 0.8) \text{ \AA}$ ,  $|b| = (14.9 \pm 0.7) \text{ \AA}$ ,  $\phi = 83.5^\circ \pm 5.0^\circ$ ) with a packing density of  $A_{vdW}/A_{mol} = 1.6$ . In contrast to the hexagonal structure, the rhombic structure assumes a range of orientations compared to the underlying substrate, suggesting a weaker molecule-substrate interaction in this case.

## 5.3 Adsorption orientation

The hexagonal and rhombic adsorption structures differ in two respects from those of the previously studied compounds: (i) the characteristic v-shape for a flat-lying *ortho*-backbone is not observed, and (ii) the molecular packing density is considerably higher,  $A_{vdW}/A_{mol} = 1.5$  (1.6) for the hexagonal (rhombic) structures, respectively, while the similar ratios for the *para*, *meta*, and *threespoke*-compounds were found to lie between 0.58 and 0.96. Packing densities substantially larger than 1 do not conform with a flat-lying orientation of the molecular backbone. We therefore conclude that the *ortho*-compounds adsorb in an upright-standing geometry.

The distance,  $d$ , between the maxima for two protrusions belonging to the same molecule was found to be  $d = (7.3 \pm 0.5) \text{ \AA}$  ( $(7.9 \pm 0.5) \text{ \AA}$ ) for the hexagonal (rhombic) structure. This may be compared to theoretical distances between *tert*-butyl groups for molecules with planar backbones as sketched in Fig. 5.5 ( $d_1 = 5.9 \text{ \AA}$ ,  $d_2 = 14.2 \text{ \AA}$ ,  $d_3 = 10.9 \text{ \AA}$ ). The poor agreement suggests that the molecular spokes are rotated such that the two outermost benzene rings are not parallel to the centermost one. In this way any distance between  $d_1$  and  $d_2$  may be realized, allowing for agreement with the experimental observations.

## 5.4 Discussion

Compared to the *para*, *meta*, and *threespoke*-molecules the two spokes of the *ortho*-compound are in much closer proximity, implying larger steric effects between the *tert*-butyl groups and stronger attractive interactions between the aromatic systems of the two spokes [204]. The non-planar conformation with rotated outermost benzene rings may result from these interactions [205]. A non-planar conformation is expected to weaken the backbone-substrate interaction in case of flat-lying adsorption geometries. We speculate that the upright orientation of the *ortho*-molecules is induced by this effect and further stabilized by attractive  $\pi - \pi$  interactions with the aromatic systems of the neighboring molecules [206]. In addition, the acute angle between the spokes allow both end groups to be placed in close proximity on the substrate for an upright adsorption orientation which would not be possible for the other compounds studied.

The molecular packing in the observed phases for the *ortho*-compound is less dense [189] than in conventional self-assembled monolayers while still keeping the conducting backbone in an upright orientation. This makes the structures highly interesting from the perspective of performing single-molecule conduction measurements on the oligo-phenylene-ethynylene backbones since the electron transport through neighboring molecules is largely reduced if the molecules are better dispersed on the surface [203].

## CHAPTER 6

---

### Amines on Au(111)

---

In this chapter the adsorption of aliphatic amines on the Au(111) surface will be investigated. It will be shown that the structures formed by octylamine undergo an irreversible change upon annealing. Based on both STM, XPS and NEXAFS measurements, it will be evidenced that the new structures consist of di- and trioctylamine.



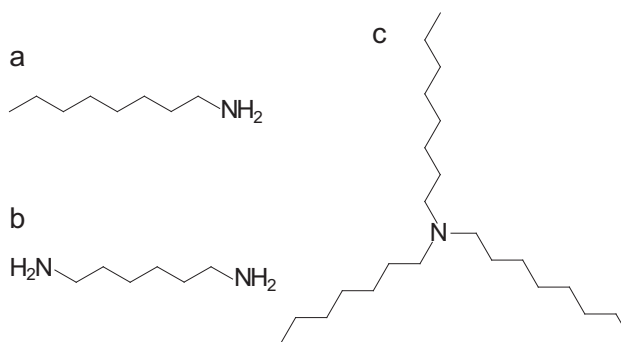


Figure 6.1: Schematic drawing of the aliphatic amines. (a) Octylamine. (b) 1,6-diaminohexane. (c) Trioctylamine.

## 6.1 Introduction

The topic of this chapter is the adsorption of aliphatic amines on the inert Au(111) surface under UHV conditions. The investigations are motivated by the use of octylamine and 1,6-diaminohexane as reactants in surface mediated condensation reactions discussed in the following chapters. The amines investigated are octylamine, trioctylamine, and 1,6-diaminohexane (see Fig. 6.1).

Octylamine was investigated in most detail with both STM, XPS and NEXAFS. We found that a lamellar structure is formed upon deposition at room temperature. Upon annealing above 400 K the molecular layer undergoes a structural change, resulting in domains where the molecules are arranged into either a honeycomb or zig-zag structure, as revealed by STM measurements. The new structures are thermally very stable and survive annealing above 500 K which points towards very strong intermolecular interactions. The spectroscopic results indicate that the structural changes result from a dehydrogenation process followed by the formation of di- and trioctylamine. To provide further evidence for this hypothesis the honeycomb structure is compared to the STM signature of trioctylamine on Au(111) which forms a similar honeycomb structure.

1,6-diaminohexanes also form lamellar structures on the Au(111) surface upon deposition at room temperature. The molecules could only be imaged with STM on a sample cooled below 120 K since they were otherwise diffusive.

### 6.1.1 Amine adsorption studies

The adsorption of aliphatic amines on various transition metal surfaces has been studied in the past, motivated mainly by amine related heterogeneous catalysis [207] and the use of alkylamines in the field of metal corrosion and adhesion [208].

The studies have mainly focused on the decomposition of methylamine caused by thermal treatment, and it has been shown that the fragmentation route is substrate dependent. Dehydrogenation of either the amino or alkyl groups has been observed for methylamine adsorbed on different substrates such as Pd(111) [209], Pt(111) [210],



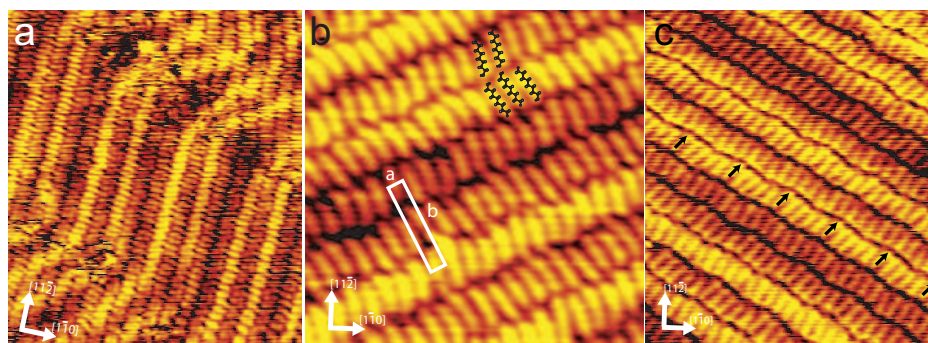


Figure 6.2: STM images of the lamellar adsorption structure formed after deposition of octylamine on Au(111) at room temperature a) Large-scale image (size  $216 \times 300 \text{Å}^2$ ). b) High-resolution image with superimposed molecular models and unit cell (size  $100 \times 100 \text{Å}^2$ ). c) STM image revealing a wavy pattern along the lamellar rows (size  $130 \times 150 \text{Å}^2$ ).

Pt(100) [211], and Ni(111) [212]. In contrast, at the Cu(110) [213] and Cu(211) [214] surface methylamine desorbs intact. In the latter case, however, the presence of oxygen results in dehydrogenation and further reactions cause a formation of dimethylamine [214]. On Cr(100) and Cr(111) methylamine was observed to undergo *C-N* bond cleavage [215]. Investigations of other aliphatic amines exist, such as dimethylamine and ethylamine on Cu(211) [207] and trimethylamine on Pt(111) [216], but no studies into amine adsorption on the Au(111) surface could be found.

Common to all the mentioned studies is that they have been obtained with averaging techniques. In contrast scanning probe investigations giving spatial information on the amine layers are very scarce. The few studies are limited to dimethylamine and trimethylamine on Si(111) [217], 1, 3-diaminopropane on the hydrogen terminated Si(111) surface [218], and dioctadecylamine at a graphite/liquid interface [219].

In contrast to alkylamines interest has been given to the adsorption of other simple hydrocarbons on Au(111) such as alkanes [43, 220, 221], alkanols [222], and not at least alkanethiols [223] forming self-assembled monolayers.

## 6.2 Octylamine

### 6.2.1 STM results

#### Room-temperature deposition

Octylamine was deposited at a pressure of  $1 - 2 \times 10^{-8}$  mBar for 1 min. through a leak valve onto the Au(111)-( $22 \times \sqrt{3}$ ) surface held at room temperature ( $\sim 300$  K). Upon cooling to a temperature in the interval of 110 – 150 K and imaging with STM, octylamine was observed to form a dense-packed lamellar structure covering most of the

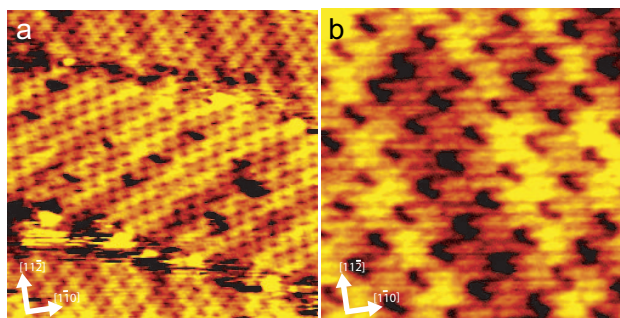


Figure 6.3: A different lamellar structure observed upon deposition onto a sample held below 120K. (a) Large-scale STM image (size  $350 \times 350 \text{Å}^2$ ). (b) Small-scale STM image (size  $100 \times 100 \text{Å}^2$ ).

surface. STM images can be seen in Fig. 6.2. The lamellar structure could be imaged at both positive and negative bias.

In the lamellar structure an octylamine molecule is visualized as a bright elongated feature with a length matching expectations (see. Fig. 6.2b). The octylamines adsorb with the alkyl chains parallel with the surface and stacked into rows (lamellae) running along a  $\langle 11\bar{2} \rangle$  high symmetry direction. We observe a preference for stacking along the ridges of the herringbone reconstruction compared to the other  $\langle 11\bar{2} \rangle$  directions. Within a row each molecule can interact by Van der Waals interactions with two neighboring molecules. All molecules within a row are tilted by an angle of either  $+(11 \pm 1)^\circ$  or  $-(11 \pm 1)^\circ$  with respect to a  $\langle 1\bar{1}0 \rangle$  high symmetry direction. The sense of rotation alternates between adjacent rows resulting in a  $(22 \pm 2)^\circ$  angle between molecules in neighboring rows. We can construct a rectangular unit cell to the structure containing 2 molecules with dimensions  $a = 5.2 \pm 0.4 \text{Å}$  and  $b = 26.3 \pm 1 \text{Å}$ , as depicted in Fig. 6.2b. Note that the distance,  $a$ , corresponds to one repeat distance,  $d$ , along a  $\langle 11\bar{2} \rangle$  direction of the substrate ( $d = 5.0 \text{Å}$  parallel to a ridge,  $d = 4.8 \text{Å}$  otherwise).

The position of the amino group cannot be determined from the STM images and is thus speculative. However, in some images we observe a wavy pattern of the molecules along the row with a repeat distance of 5 molecules, as marked by the arrows in Fig. 6.2c. This could indicate a non-random arrangement of the amino groups along the row, potentially realized by three neighboring amino groups in one row interacting with two neighboring amino groups in the adjacent row.

If the molecules are dosed onto a surface cooled below 120K we occasionally observed another and co-existing lamellar structure in which the octylamines are stacked three-by-three into rows, as seen in Fig. 6.3. We assume that the two structures deviate in the orientation of the amino groups. In this case the three-by-three pattern could be realized if two neighboring amino-groups in one row interact with one amino group in the adjacent row.

We assume that the lamellar structures formed are mainly governed by molecule-substrate interactions due to the high degree of commensurability between the molecules

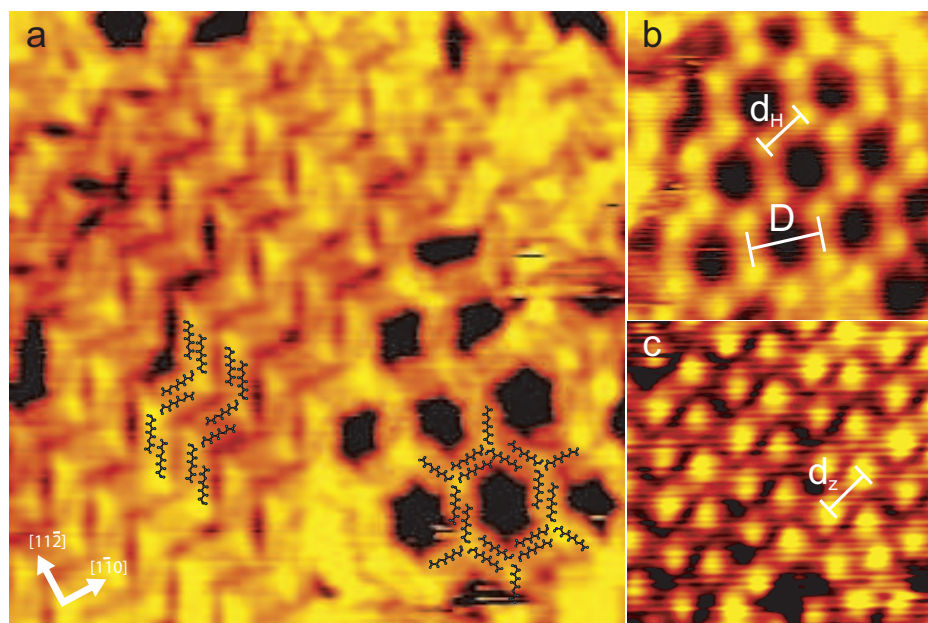


Figure 6.4: Phase transition upon annealing to 400K a) Backbone imaging mode (size  $170 \times 170 \text{ \AA}^2$ ). Nitrogen imaging mode of the b) honeycomb phase and c) zig-zag structure (sizes  $100 \times 100 \text{ \AA}^2$ ).

and the surface reconstruction and by Van der Waals interactions between the molecules. This is supported by the fact that amino groups normally form only very weak hydrogen bonds, as primary amines only participate as hydrogen donors in hydrogen bonds [224].

### Thermal activation

Upon annealing above 400K the molecular layer undergoes an irreversible structural change, as seen in the STM images of Fig. 6.4. We observe two co-existing phases, an open honeycomb structure (right side in Fig. 6.4a and Fig. 6.4b) and densely packed zig-zag rows (left side in Fig. 6.4a and Fig. 6.4c). The new phases can be imaged in two imaging modes. The image in Fig. 6.4a is obtained in an imaging mode revealing the individual alkyl chains whereas the images in Figs. 6.4b and 6.4c are dominated by bright protrusions which we attribute to a moiety comprising one or more N-atoms. Note that the appearance of the individual molecules has changed after the structural change, so that we now have two imaging modes both revealing a higher contrast at one molecular end.

From images revealing the molecular backbone, (see Fig. 6.4a), it is evident that the alkyl chains are oriented along the  $\langle 1\bar{1}0 \rangle$  directions. The honeycomb structure can be rationalized by trimers consisting of three molecules meeting head-to-head in a  $120^\circ$  angle. Six such trimers can be joined pairwise tail-along-tail as seen on the model in

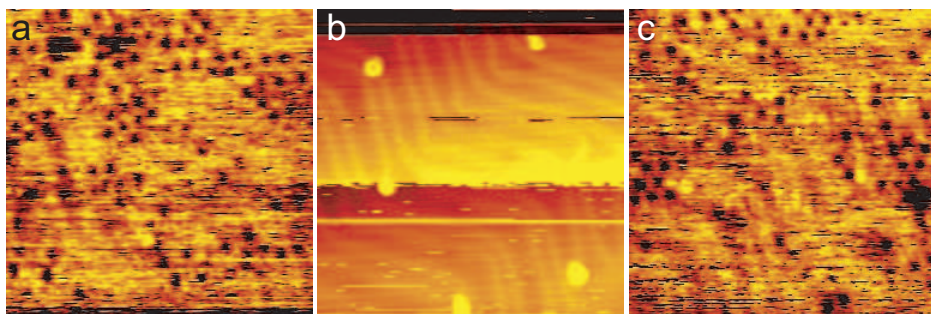


Figure 6.5: STM image sequence of the same area (size  $500 \times 500 \text{ \AA}^2$ ) with alternating bias voltage applied to the sample showing that the honeycomb structure and zig-zag structure are invisible at negative bias. (a) First image ( $I_t = 0.37$ ,  $V_t = +1.846$ ). (b) Second image ( $I_t = 0.43$ ,  $V_t = -1.846$ ). (c) Third image ( $I_t = 0.37$ ,  $V_t = +1.846$ ).

Fig. 6.4a, resulting in a hexagonal pore of  $D = 27 \pm 2 \text{ \AA}$  diameter<sup>1</sup>. In the densely packed phase only two molecules, forming a dimer, meet head-to-head in a  $120^\circ$  angle. These dimers are again joined tail-to-tail resulting in zig-zag lines as seen in Fig. 6.4a.

As the tails can be joined in two mirroring ways, both structures express organizational chirality. The distance  $d_H = 15 \pm 2 \text{ \AA}$  ( $d_Z = 15 \pm 2 \text{ \AA}$ ) (see Figs. 6.4b (6.4c)) between two head-to-head meeting points in the honeycomb phase (zig-zag phase) match, supporting the similar built-up arrangement. The structures are still found upon annealing to 500 K, which is far above the desorption temperature ( $T < 280 \text{ K}$ ) of alkanes with similar chain length [220].

In contrast to the lamellar structure, the new phases could only be observed at positive bias and the tunneling junction was often very unstable. At negative bias the molecules are not visible in the STM images and the underlying herringbone reconstructed Au(111) substrate is imaged instead (see a bias dependent image sequence in Fig. 6.5).

## Discussion

The STM results clearly demonstrate an irreversible structural change in the molecular layer. Furthermore we observe a change in imaging conditions and a change in the appearance of the individual molecules (compare the images in Fig. 6.2 and Fig. 6.4). This indicates that the structural change is accompanied by a change in the electron density of states or even a chemical change. Based on the STM images alone we can only speculate on the driving force for the structural changes.

In the simplest model two or three octylamines arrange head-to-head in a node, and the structure should in this case be mediated by three hydrogen bonds within the node. However, hydrogen bonds formed between amines are expected to be weak and the high desorption temperature (above 500 K) would in this case be unexpected. Furthermore,

<sup>1</sup>Very precise distance measurements were not possible due to a high drift in the images.

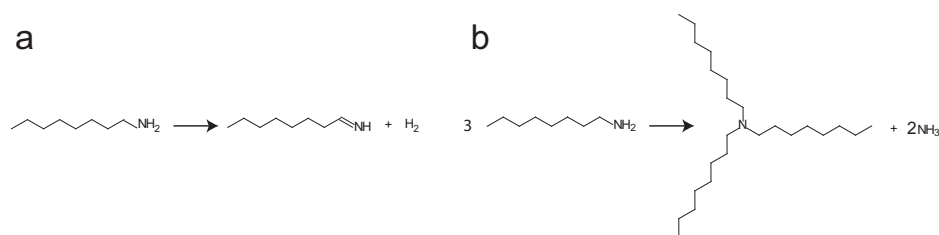


Figure 6.6: Possible chemical changes in octylamine. (a) Elimination to octylimine. (b) Substitution to trioctylamine.

since the molecules are not chemically changed, there is no explanation for the change in imaging conditions. We thus think that a more profound change has occurred.

Potentially, some of the amines could undergo deprotonation of the amino group, which could lead to a stronger intermolecular bonding in the nodes. In this case a change in imaging conditions would be less unanticipated. Dehydrogenation of the amino group has been observed for methylamine on Pd(111) and Pt(111) [209]

In another model, the structural change is based on an elimination reaction in which octylamine is converted to octylimine under the release of hydrogen (see 6.6a). A similar dehydrogenation driven phase transition was observed for DPDI on Cu(111) previously [36]. Due to the  $sp^2$  hybridization of the nitrogen atom in imines compared the  $sp^3$  hybridization of the nitrogen atom in amines, stronger hydrogen bonds within the imino nodes would be expected. Furthermore, since the molecule has undergone a chemical change, a change in imaging conditions would be expected.

In a third model, two or three amines have reacted by a substitution reactions whereby dioctylamine and trioctylamine is formed, as shown in Fig. 6.6b. Such a reaction is not expected in solution and would therefore have to be catalyzed by the Au(111) surface. Since new molecules would be formed in this case, a change in imaging conditions and molecular appearance would not be unreasonable. For studies of trimethylamine on Si(111) the same bias dependent imaging was observed [217].

### 6.2.2 Spectroscopy results

To obtain information about the chemical state of the adsorbed molecules we performed x-ray photoelectron spectroscopy (XPS) and near-edge x-ray absorption fine structure (NEXAFS) spectroscopy at beamline I311 at MAX-Lab.

The experiments were performed by two different preparation procedures. In preparation procedure A octylamines were dosed at a pressure of  $10^{-7}$  mBar for 6 minutes onto a sample held below 120 K. This resulted in the build-up of multilayers. In preparation procedure B, octylamines were dosed at a pressure of  $2 \times 10^{-7}$  mBar for 1 minute onto a sample held at 293 K.



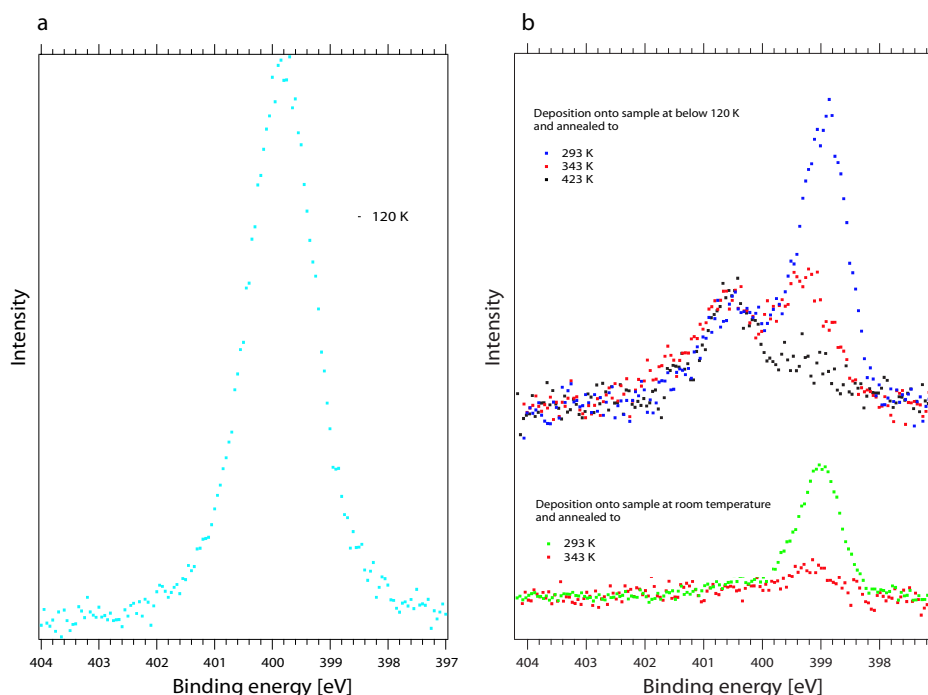


Figure 6.7: XPS  $N_{1s}$  spectra. (a) Multilayer deposited at  $\sim 120$  K. (b) Monolayer at different annealing temperatures and different preparation procedures. Upper graphs: Preparation A. Lower graphs: Preparation B

### XPS

The  $N_{1s}$  and  $C_{1s}$  x-ray photoemission spectra are shown in Figs. 6.7 and 6.8, respectively. The  $N_{1s}$  multilayer spectrum obtained at a temperature below 120 K displays a single peak with a binding energy of 399.8 eV. A chemical shift from 399.8 eV to 398.9 eV along with the appearance of an additional minor high-energy peak at 400.4 eV is observed upon annealing to room temperature (293 K). A further annealing to 343 K results in a narrowing of the main peak associated with an upward energy shift from 398.9 to 399.2 eV and a possible slight change in position of the high energy peak to 400.6 eV. As the surface temperature reaches 423 K the low energy peak at 399.2 eV has almost disappeared and the peak at 400.6 eV is now dominant. In accordance with Ref. [209] the peaks with the high binding energies (between 399.8 eV and 400.6) can be attributed to mono, di, or trioctylamine, whereas the peaks with a lower binding energy (398.9 eV and 399.2 eV) can stem from partly dehydrogenated amines.

The  $C_{1s}$  multilayer spectrum displays a peak with a binding energy of 286.1 eV. Also in the carbon spectrum a significant shift is observed from 286.1 to 284.0 K upon annealing to room temperature 293 K. A further annealing to 343 K results in a peak broadening with an associated shift in peak position to 284.2 eV. No further shifts are ob-

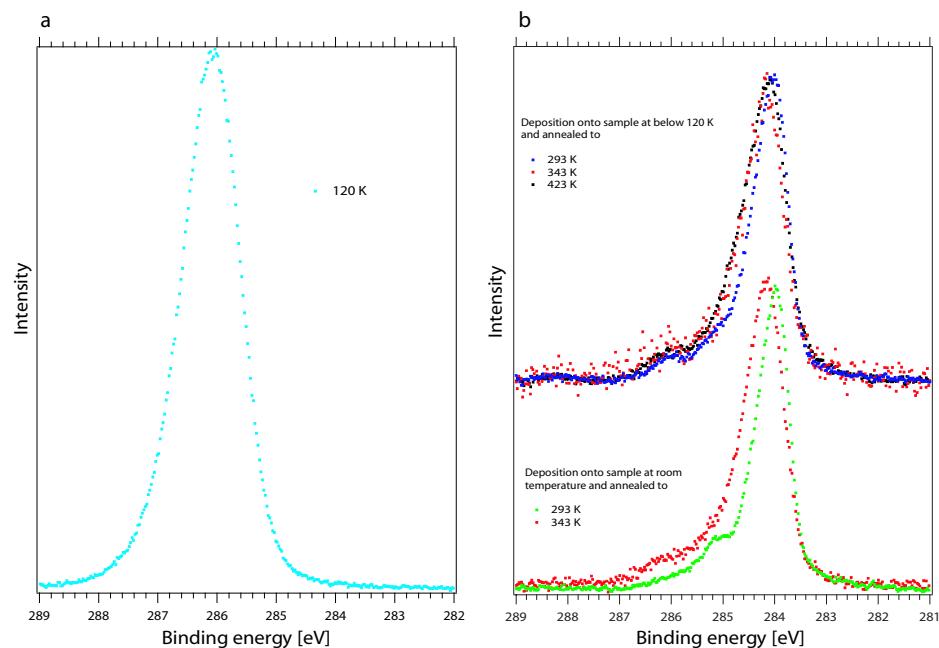


Figure 6.8: XPS  $C_{1s}$  spectra. (a) Multilayer deposited at ~ 120 K. (b) Monolayer at different annealing temperatures and different preparation procedures. Upper graph: Preparation A. Lower graph: Preparation B.

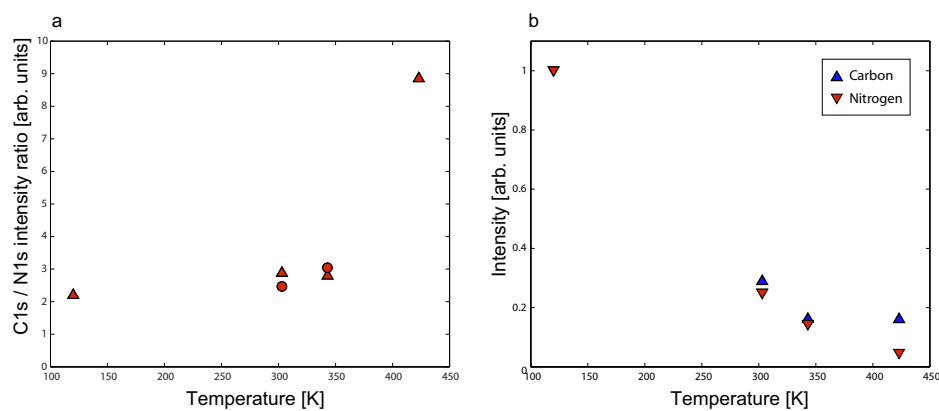


Figure 6.9:  $C_{1s}$  and  $N_{1s}$  intensity plots. (a) Relative intensities as a function of annealing temperature. Triangles and circles mark data obtained upon preparation A respectively B. (b)  $C_{1s}$  and  $N_{1s}$  intensities normalized to the initial  $C_{1s}$  and  $N_{1s}$  intensity, respectively. The data stem from preparation A.

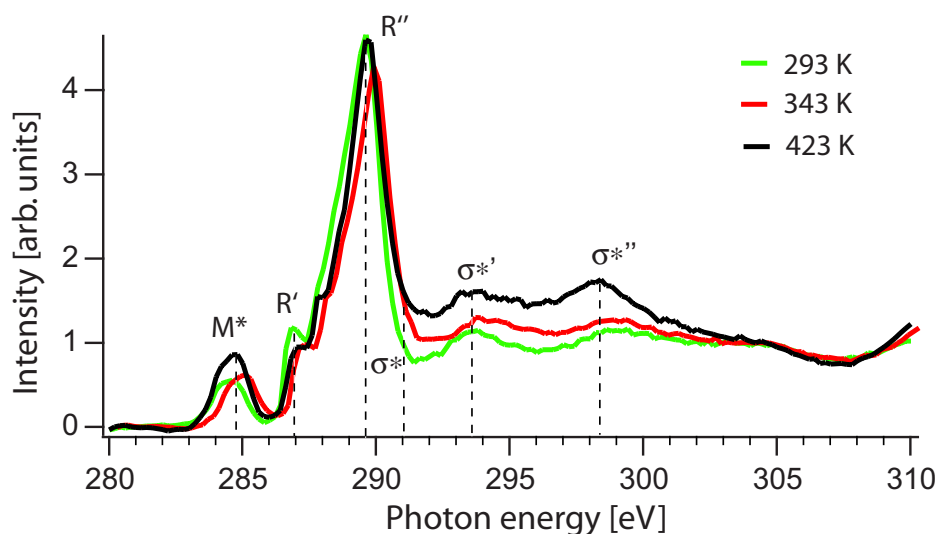


Figure 6.10: NEXAFS  $C_{1s}$  spectra with  $55^\circ$  photon incidence angle obtained after different annealing steps following preparation 1.

served in the last annealing step to 423 K. A downwards shift in binding energy between an organic multilayer and the corresponding monolayer is often observed for saturated hydrocarbons [225] and is caused by a more efficient screening in the photoemission process of the created core hole by the metallic electrons. The peak broadening above 343 K indicates a chemical shift towards higher binding in at least one of the carbons, potentially the  $C-N$  carbon.

In Fig. 6.9 plots of the  $C_{1s}$  and  $N_{1s}$  intensities at different annealing stages are seen. From the plot in Fig. 6.9b it is evident that there is a high degree of desorption at all annealing stages. However, it seems that only nitrogen is desorbing during the last step from 343 K to 423 K. In Fig. 6.9a the ratio between the  $C_{1s}$  and  $N_{1s}$  intensity is plotted as a function of temperature. The graph reveals that the  $C_{1s}/N_{1s}$  intensity stays nearly constant until 343 K, and increases by a factor of  $\sim 3$  during the last annealing step. This indicates that the stoichiometric ratio between carbon and nitrogen has increased with a factor of 3 after the phase transition signalling dissociation of  $C-N$  bonds and desorption of nitrogen.

### NEXAFS

$C_{1s}$  NEXAFS spectra obtained at different annealing stages with a  $55^\circ$  photon incidence angle are shown in Fig. 6.10. The spectra are dominated by 5 peaks. The broad resonance, termed  $M^*$ , at appr. 285 eV is assigned to excitations into metal-molecule hybrid orbitals which indicate the formation of weak bonds between the saturated hydrocarbon and the Au(111) surface [225]. The  $R'$  and  $R''$  resonances at 287.0 eV and 289.7 eV, respectively, can be attributed to transitions into Rydberg states with  $R'$  corresponding



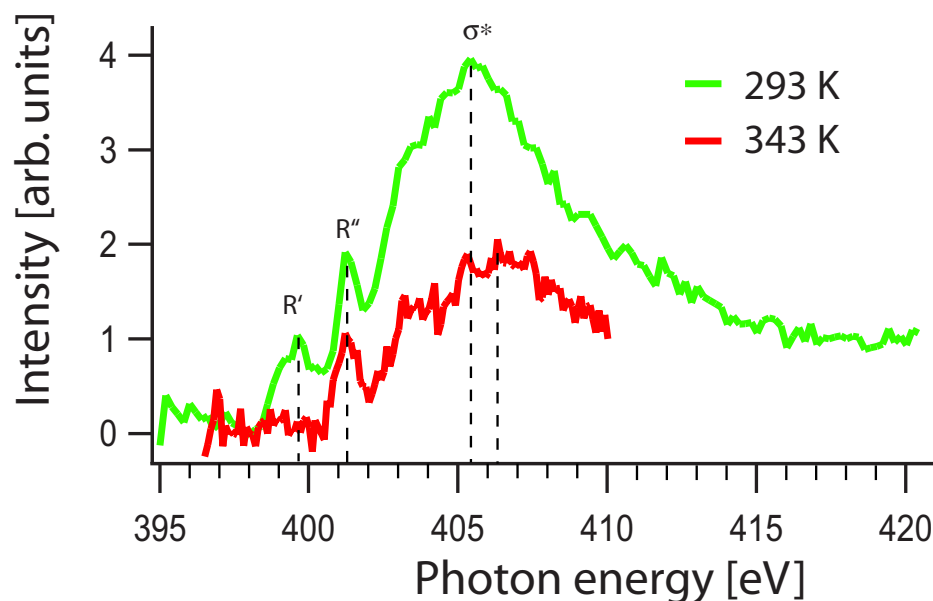


Figure 6.11: NEXAFS  $N_{1s}$  spectra with  $55^\circ$  photon incidence angle obtained after different annealing steps following preparation 2.

to the  $1s - 3s$  transition and  $R''$  corresponding to the  $1s - 3p$  transition [225, 226]. We observe a decrease in  $R'$  upon annealing which is expected for three-fold symmetric molecules (such as trimethylamine) [226]. The sigma resonances are associated with transitions into valence orbitals of the carbon-carbon and carbon-nitrogen backbone [225, 226].

Similar  $N_{1s}$  NEXAFS spectra are shown in Fig. 6.11. The spectrum obtained at room temperature is dominated by two sharp Rydberg resonances and a broad sigma peak (405.5 eV). We can assign the  $R'$  (399.7 eV) and  $R''$  (401.3 eV) resonances to the  $1s - 3s$  and  $1s - 3p$  transitions [226]. Upon annealing to 343 K the  $1s - 3s$  resonance disappears which indicates that the nitrogen atom is now situated in a symmetric environment [226]. Furthermore, the sigma resonance is shifted approximately 1 eV towards higher photon energies.

## Discussion

The NEXAFS results do not show any low lying  $\pi$ -resonances corresponding to  $C = N$  double bonds. We therefore rule out that octylimines have been formed upon annealing.

The XPS results show that the octylamines change chemically during the different annealing steps up to 423 K. Upon annealing to room temperature the spectra indicate that both the amino groups and the carbonyl backbones undergo some dehydrogenation. Furthermore, a resonance with a high binding energy is observed in the  $N_{1s}$  spectrum

(even higher than the initial binding energy). At 423 K close to all nitrogen atoms are in this higher binding state. From the intensity plots we can see the chemical changes are competing with desorption of molecules. Furthermore we observe that the stoichiometric ratio between the nitrogen and carbon signal decreases by a factor of 3 during the annealing to 423 K. Taken together, all these spectroscopic features point towards the formation of dioctylamine or trioctylamine which are both expected to have a slightly higher binding energy than octylamine, in agreement with the  $N_{1s}$  peak at 400.6 eV and the peak broadening observed in the  $C_{1s}$  spectrum. Furthermore, both the  $N_{1s}$  and  $C_{1s}$  NEXAFS spectra show that the resonance corresponding to  $1s - 3s$  Rydberg transitions are decreased upon annealing, which is expected for threefold symmetric molecules such as trioctylamine and ammonia.

The combined STM and spectroscopic data show that octylamine undergoes a chemical change upon annealing above 400 K. Due to the molecular geometry observed in the STM images of the honeycomb and zig-zag structure combined with the spectroscopic results, we speculate that dioctylamine and trioctylamine have been formed on the surface. This reaction is not expected to happen spontaneously by conventional solution phase chemistry, and the Au(111) surface should in this scenario act as a catalyst.

Since the stoichiometry between nitrogen and carbon XPS intensities decreased upon annealing, some  $C-N$  dissociation must have proceeded. DFT calculations of the energy barrier (3.5 eV [227]) towards direct dissociation of  $C-N$  bonds on the Au(111) show that this is an unexpected event. The barrier towards the  $C-N$  bond dissociation could potentially be lowered by bond-formation to other amino groups during cleavage. This however is pure speculation and a future topic for DFT investigations.

The spectroscopic measurements also indicated some dehydrogenation of both the amino and alkyl groups. The honeycomb and zig-zag phases could thus also be mediated by strong intermolecular ionic bonds, potentially with additional bond formation to the surface.

### 6.3 Trioctylamine

To produce further evidence that octylamine undergoes a substitution reaction on Au(111) which results in the formation of dioctylamine and trioctylamine, we performed STM measurements for trioctylamine adsorbed directly onto the Au(111) surface.

Upon deposition of trioctylamine at a pressure of  $1 - 2 \times 10^{-8}$  mBar for 1 min. onto the Au(111) sample held at room temperature ( $\sim 300$  K) and subsequent scanning with STM, trioctylamine was observed to form the honeycomb structure shown in the STM images of Fig. 6.12. A further annealing to 400 K did not cause changes in the structures.

The structure has the same characteristics as the structures formed by octylamine annealed above 400 K: (i) The structure can be imaged in two distinct imaging modes revealing either the nitrogen atoms (Fig. 6.12a) or the molecular backbones (Fig. 6.12b). (ii) The structure can only be imaged with a positive bias applied to the sample. If a negative bias is applied the herringbone reconstructed Au(111) surface is imaged instead.

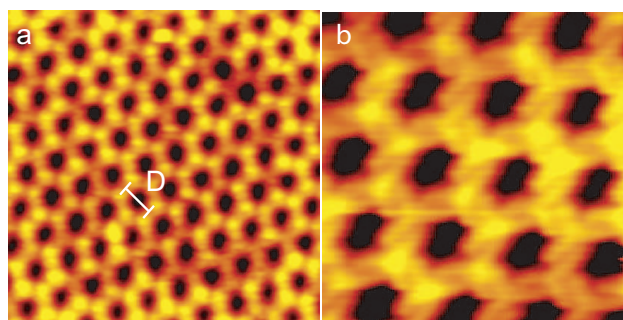


Figure 6.12: STM images obtained after deposition of trioctylamine on Au(111). (a) Nitrogen imaging mode (size  $\sim 250 \times 250 \text{ \AA}^2$ ). (b) Backbone imaging mode (size  $\sim 100 \times 100 \text{ \AA}^2$ ).

(iii) The pore size<sup>2</sup>,  $D = 26.5 \pm 3 \text{ \AA}$ , matches the pore size observed for the honeycomb structure formed by the octylamines. We see the STM results as further evidence that trioctylamine and dioctylamine are formed upon thermal treatment of octylamine on the Au(111) surface.

## 6.4 1,6-diaminohexane

1,6-diaminohexane was deposited onto the Au(111) surface at a pressure of  $1 \times 10^{-8}$  mBar for 30 s through a leak valve. During deposition the Au(111) surface was held at room temperature ( $\sim 300 \text{ K}$ ). Upon cooling to a temperature below 120 K and imaging with STM, 1,6-diaminohexane was observed to form dense-packed lamellar rows on the surface. An STM image can be seen in Fig. 6.13. The molecular structure could be imaged at both positive and negative bias.

The structure is built up of flat-lying 1,6-diaminohexanes stacked into rows with molecules in adjacent rows meeting end-to-end. At the row boundaries amino groups show up as a bright protrusion. The rows are running along a  $\langle 11\bar{2} \rangle$  high symmetry direction. Compared to the molecular layers formed by octylamine, the ordered domains consisting of amine rows are smaller, often consisting of only a single row. Due to low resolution in the images it is not possible to determine if the molecular backbones are oriented along a  $\langle 1\bar{1}0 \rangle$  direction or tilted slightly.

At temperatures above 120 K the molecules are too diffusive to be stabilized in the structures. Since the needed stabilization temperature is close to the low temperature limit of the system, the images had to be acquired right after the cooling was released. This caused a high drift in the images, and precise distance measurements could therefore not be performed. However the observed elongated molecular units have a length which does not contradict the expectation for single 1,6-diaminohexane molecules. Models of 1,6-diaminohexanes are superimposed on the image.

<sup>2</sup>Due to a high drift in the images it was not possible to measure distances very precisely.

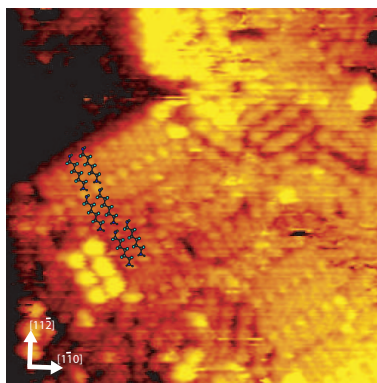


Figure 6.13: STM image obtained after deposition of 1,6-diaminohexane on Au(111) (size  $120 \times 120 \text{ \AA}^2$ ).

## 6.5 Summary

We have investigated the adsorption structures formed by octylamine, trioctylamine, and 1,6-diaminohexane on Au(111). Both octylamine and 1,6-diaminohexane formed lamellar structures on the Au(111) surface. In both cases the lamellar rows were oriented along  $\langle 11\bar{2} \rangle$  directions. The rotationally ordered domains were larger for octylamine compared to 1,6-diaminohexane which could be caused by the 1,6-diaminohexanes being more mobile at the imaging temperature.

Furthermore, based on a combination of STM images and spectroscopy measurements we found evidence that octylamine undergoes a thermally activated substitution reaction on the Au(111) surface whereby di and trioctylamine is formed. This process is competing with desorption of unreacted octylamine molecules. Such a reaction is not expected to happen spontaneously in conventional solution phase chemistry, and the Au(111) surface is therefore expected to act as a catalyst. We hope that future DFT calculations will shine light on the reaction mechanism for this unanticipated surface reaction.

## CHAPTER 7

---

### Imineformation on Au(111)

---

The formation of Schiff bases is one of the most fundamental reactions in organic chemistry. In this chapter it will be demonstrated that the reaction can proceed on a Au(111) metal substrate under ultrahigh vacuum conditions. Furthermore, the conformation of the reaction products will be investigated upon different preparation procedures.

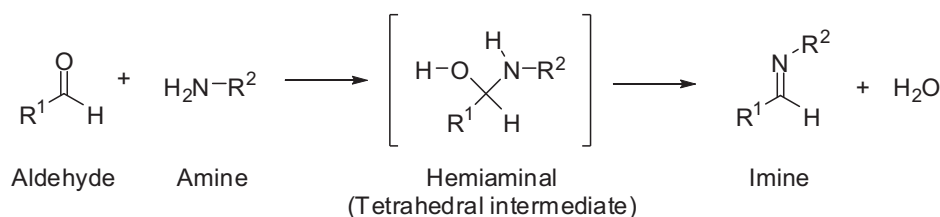


Figure 7.1: Generalized solution catalyzed imineformation between an aldehyde and an amine.

## 7.1 Introduction

The aim of this chapter is to demonstrate that imineformation can proceed in the extreme low-coverage limit from reactants co-adsorbed directly on the inert herringbone reconstructed Au(111)- $(22 \times \sqrt{7})$  surface under UHV conditions [196]. Furthermore, the conformation of the reaction products will be investigated at the submolecular level by STM upon different preparation procedures.

### 7.1.1 Imineformation

Imines are formed when carbonyls react with amines under elimination of water. The basic reaction mechanism [166, 228] is shown in Fig. 7.1. In the first step the amine attacks the aldehyde and an intermediate, called a hemiaminal, is formed. In the second step dehydration gives the imine. When the reaction is carried out in solution an acid catalyst is normally added to increase the speed of water elimination by protonation of the leaving group in the second step. At low pH values the nucleophilic attack in the first step is however hindered by a high amount of protonated amines. The condensation reaction is therefore most effective in a weak acid environment (pH 4-6) close to neutral conditions, just as in biological reactions. In an aqueous environment imineformation is a reversible reaction, and imines are consequently unstable with respect to their parent carbonyl and amine compound unless water is removed from the reaction mixture.

In nature imines (also called Schiff bases) and their formation by condensation of amines with carbonyls are crucial in several important enzymatic processes, such as formation of amino acids from keto acids [229]. In synthetic chemistry imines are likewise of fundamental importance, and are used in the synthesis of e.g. secondary amines by reductive amination [166] and in the formation polymeric materials [230]. Recently, imineformation has proven excellent in the formation of large, ordered, covalently bound structures in solution owing to the reversibility of the reaction. By applying a combination of supramolecular metal coordination chemistry and covalent interlinking by condensation of carbonyl and amino groups, large structures with high order have been realized [20, 193, 231, 232].

Within surface science, thin films ( $\sim 10$  nm) of polyimines have been grown on metal surfaces under UHV conditions by the technique of vapour deposition polymerization [82, 230, 233]. Such multi-layer thick imine films have mostly been studied by

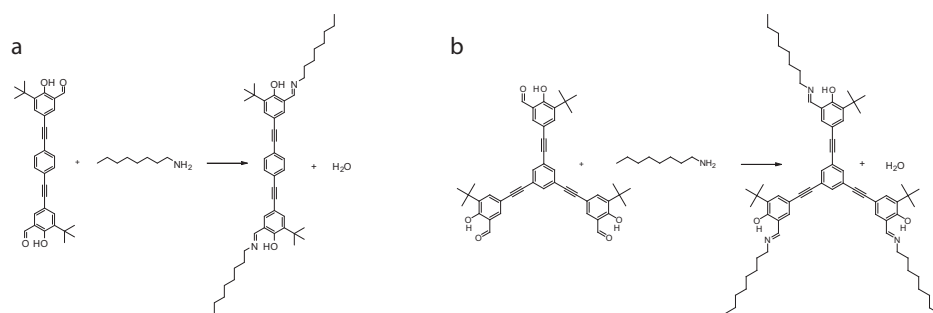


Figure 7.2: Model systems: (a) Reaction between the *para*-molecule (dialdehyde) and octylamine. (b) Reaction between the *three-spoke*-molecule (trialdehyde) and octylamine.

spectroscopic techniques such as x-ray photoelectron spectroscopy (XPS), near-edge-x-ray adsorption fine structure (NEXAFS) or photoluminescence. STM studies are in contrast very scarce and of low resolution [82].

### 7.1.2 Model systems

As model systems we chose imineformation between octylamine and the aldehyde groups on the *para*-compound (Fig. 7.2a) respectively the *three-spoke*-compound (Fig. 7.2b). The systems were selected because the *para* and *three-spoke*- compounds display a high degree of flexibility on the Au(111) surface at room temperature, owing to lateral diffusion and conformational changes, discussed in Chapter 4. Furthermore, it has previously been shown that condensation of the *three-spoke*-molecule with ethylenediamine and manganese acetate results in the formation of chiral manganese-salen-linked polymers in solution [193]. The chain length of the amine was chosen to optimize the ease of deposition (high vapour pressure) with the visibility by STM and fixation on the substrate (long alkyl-chains).

The adsorption characteristics of the reactants are discussed in Chapters 4 and 6. From these studies we know that the reactants adsorb with a flat-lying geometry on the Au(111) surface. The *para* and *three-spoke*-compounds (Chap. 4) form large, ordered domains containing a number of different structures, as observed by STM at low temperatures. From images obtained in the *tert*-butyl imaging mode the different conformations of the *para* and *three-spoke*-molecules can be distinguished, and all the different surface conformers are thereby known to exist on the surface after deposition and possibly annealing to 450K. Examples of STM images revealing some of the conformers of the *para* and *three-spoke*-compounds are shown for reminder in Figs. 7.3a and 7.3b. Octylamine forms a densely-packed lamellae structure upon deposition at room temperature (Fig. 7.3c).

The reaction between octylamine and the *para*-compound will be discussed in the first part of this chapter. By STM and NEXAFS data we will give evidence that the reactants interlink covalently upon co-adsorption. Furthermore, a solvent-free reaction

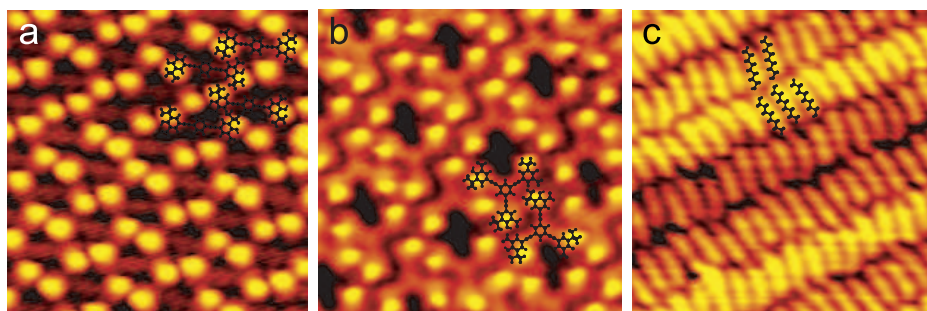


Figure 7.3: STM images of the reactants (Size  $80 \times 80 \text{Å}^2$ ): (a) *Para*-molecule. (b) *Threespoke*-molecule. (c) Octylamine.

path is proposed based on ab-initio density functional theory calculations. In the second part of the chapter the imineformation with the threespoke molecule and octylamine will be discussed with focus on the observed conformations of the products.

## 7.2 Para-compound and octylamine

To react the *para*-compound with octylamine on the Au(111) surface in UHV, we first deposited the *para*-compounds on the substrate to create a submonolayer coverage. Subsequently, the surface was exposed to a vapour of octylamines. In this preparation all the steps were performed inside the vacuum chamber (*in-situ*), and the imine products are thus referred to as the *in-situ* reaction products.

For comparison the imine reaction product was also synthesized by conventional solution phase chemistry and deposited directly onto the Au(111) substrate by evaporation from a heated glass crucible. The reaction products formed by this procedure are referred to as the *ex-situ* reaction products.

### 7.2.1 STM results

#### In-situ reaction

To form the reaction *in-situ* for imaging with STM, we first deposited the *para*-compounds on the Au(111) substrate (typically  $< 1/3$  ML as estimated by STM). Subsequently, the surface was brought close to saturation of the first monolayer by exposing it to a vapour of octylamines ( $p \sim 1 - 5 \times 10^{-8}$  mbar) with the sample held at RT ( $\sim 300$  K) during evaporation. For imaging with STM the sample was cooled down to temperatures between  $120 - 160$  K. This procedure resulted in the formation of large, highly ordered islands surrounded by more disordered areas, as seen in Fig. 7.4a.

The structure of the islands (see Fig. 7.4b) is clearly different from the structures formed by exposing the surface to the individual reactants. The protrusions in the STM images associated with the *tert*-butyl groups form parallel double rows with the aromatic



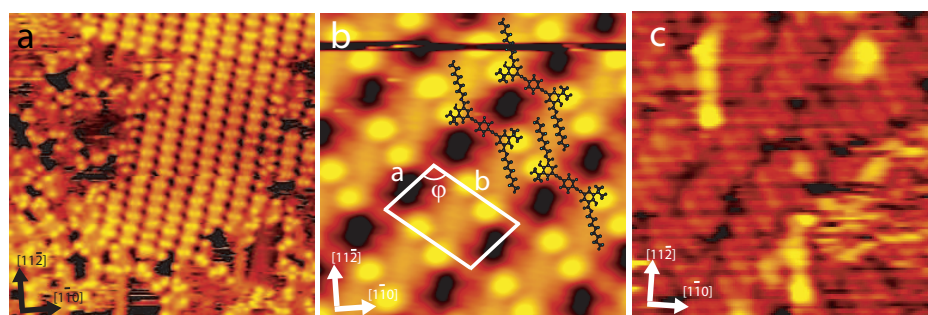


Figure 7.4: STM images obtained after co-deposition of the *para*-reactant and octylamine at room temperature: (a) Large scale image (size  $400 \times 400 \text{Å}^2$ ). (b) The in-situ structure (size  $80 \times 80 \text{Å}^2$ ). (c) Outside the condensed islands (size  $80 \times 80 \text{Å}^2$ ).

backbone visualized between two bright protrusions belonging to neighbouring rows. The backbones are tilted at an angle of  $24.0^\circ \pm 4.0^\circ$  with respect to a close-packed  $\langle 110 \rangle$  direction of the substrate. The structure has thus a definite orientational relationship with the directions of the underlying substrate lattice. Features with a length matching the length of the octylamine are observed to extend from the aromatic end-group at the side opposite to the *tert*-butyl group, i.e. the position originally occupied by the aldehyde-group. Alkyl chains from adjacent molecules align pairwise similarly to the lamellae motif observed for the octylamine structure. All these STM features observed for the co-deposited molecular structures are consistent with it being formed by the imine reaction product, as shown in the overlay of Fig. 7.4b. The position of the alkyl chains with respect to the molecular backbone matches the expected conformation of the imine reaction product which is stabilized by an intramolecular hydrogen bond between the imine nitrogen atom and the hydroxyl group (see Fig. 7.2a). The structure is homochiral with all backbones in an island being either of the chiral RR or LL conformation<sup>1</sup> which furthermore implies that all *para*-backbones meeting head-to-head adopt a *trans*-conformation. The islands shown in Figs. 7.4a and 7.4b are of opposite chirality and the overlay in Fig. 7.4b clearly reveals the LL-conformation of the backbone. As marked on Fig. 7.4b we can construct a unit cell to the structure with the dimensions:  $a = 16.9 \pm 0.9 \text{Å}$ ,  $b = 26.8 \pm 1.3 \text{Å}$ , and  $\phi = 106.6^\circ \pm 3.0^\circ$ .

Outside the islands we observe less ordered areas with single *para*-compounds surrounded by non-reacted octylamines forming lamellae structures (see Figs. 7.4a and 7.4c). In these areas all surface conformers of the *para*-compound can be identified. Since both octylamines and free *para*-compounds are slightly diffusive at the imaging temperature, we are not able to determine whether the *para*-compounds found outside the islands have yet reacted fully or partly to the imine products.

After annealing to 400/450K followed by cooling in the STM, very large ordered islands are observed (Fig. 7.5). Upon imaging at negative bias the clean herringbone reconstructed Au(111) surface is revealed outside the islands. At positive bias a ho-

<sup>1</sup>For definitions of RR/LL, see the introduction to Chapter 4.

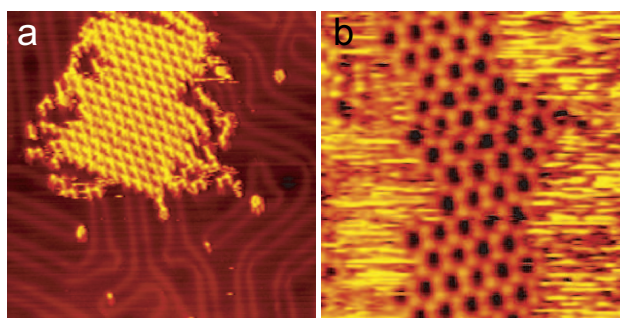


Figure 7.5: STM images obtained after co-deposition of the *para*-reactant and octylamine at room temperature and subsequent annealing to 400K: (a) Large-scale image (size  $600 \times 600 \text{ \AA}^2$ ,  $V_t = -2 \text{ V}$ ,  $I_t = 2 \text{ nA}$ ). (b) Honeycomb structure observed outside the islands containing *in-situ* products (size  $300 \times 300 \text{ \AA}^2$ ,  $V_t = 2 \text{ V}$ ,  $I_t = 0.32 \text{ nA}$ ).

honeycomb structure is observed on the terraces (Fig. 7.5b). We interpret the honeycomb structure to consist of trioctylamine formed by the excess of octylamine also observed before annealing, as discussed in Chapter 6.

The improved order after annealing signals a completion of reaction or increased surface mobility and switching of molecular conformation<sup>2</sup>. Furthermore, since all the *para*-compounds are condensed into islands, the reaction products now assume only the chiral conformations and achiral RL/LR<sup>3</sup> conformations, observed prior to the reaction, have thus been suppressed.

### Ex-situ reaction

To confirm that covalent imine-bonds have indeed been formed by the *in-situ* reaction, the imine product was synthesized *ex-situ* by conventional solution phase chemistry techniques and was evaporated directly onto the Au(111) substrate for comparison.

To prevent thermally activated on-surface reactions the substrate was held at a temperature below 130 K during evaporation<sup>4</sup> of the *ex-situ* product (Fig. 7.6). Adsorption of the *ex-situ* reaction product indeed resulted in small structural domains (Fig. 7.6a) identical to those observed after co-deposition of the individual reactants: Both the unit cell dimensions for the *ex-situ* structure ( $a = 16.9 \pm 0.9 \text{ \AA}$ ,  $b = 26.8 \pm 1.3 \text{ \AA}$ ,  $\phi = 106.6^\circ \pm 3.0^\circ$ ) and the tilt angle between the aromatic backbones and the close-packed  $\langle 1\bar{1}0 \rangle$  direction of the substrate ( $24.0^\circ \pm 4.0^\circ$ ) agree with the observations for the *in-situ* product. Outside the ordered domains we observe *para*-backbones embedded in a matrix of octylamines (Fig. 7.6b). Since both octylamines and *para*-compounds are diffusive at the imaging temperature, we cannot determine whether the backbones

<sup>2</sup>Time-resolved movies reveal that the reaction product formed with the *threespoke*-compound and octylamine can change conformation even at imaging temperatures.

<sup>3</sup>For definitions of RL/LR see the introduction to Chapter 4.

<sup>4</sup>The crucible containing the molecular powder was heated to  $\sim 421 \text{ K}$  during evaporation.

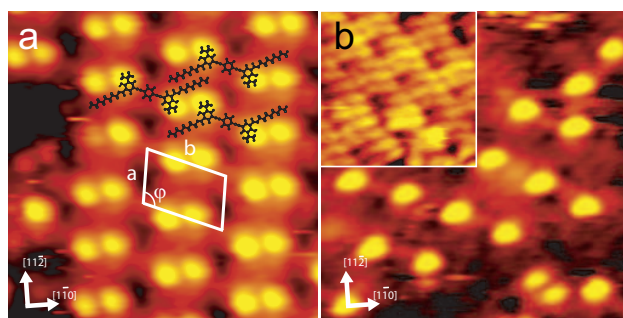


Figure 7.6: STM images obtained after deposition of the *ex-situ* reaction product onto a cold substrate ( $\sim 120$  K): (a) Small ordered island (size  $100 \times 100 \text{ \AA}^2$ ). (b) Disorder outside the islands (size  $100 \times 100 \text{ \AA}^2$ ). Inset with lamellae structure (size  $50 \times 50 \text{ \AA}^2$ ).

belong to the aldehyde (reactant) or imine form (product). In a single experiment<sup>5</sup> (not shown) a different meta-stable structure built up of molecules with the RL/LR conformation was found. This structure was never observed after annealing to 450 K.

Upon annealing to 400/450 K, large ordered domains (up to  $500 \times 500 \text{ \AA}^2$ ) of the *ex-situ* product is formed (Fig. 7.7a,b). The images shown were obtained in the  $\pi$ -system imaging mode revealing the shape of the products more clearly. Outside the domains formed by the *ex-situ* product, a honeycomb structure is observed (Fig. 7.7c image I). This implies that an excess of octylamine has been transferred to the sample upon evaporation.

Furthermore, if a lower crucible temperature ( $\sim 400$  K) is applied for evaporation of the *ex-situ* product, exclusively honeycomb structure (Fig 7.7c image II) is found on the substrate, attributed to trioctylamine formed by free octylamine molecules. We can only speculate on the origin of the observed octylamine: Either some fragmentation takes place upon evaporation or a surplus of octylamines are present in the molecular powder. Since imineformation is a reversible reaction, octylamines would be formed in the presence of water in the surroundings, but this should be rather unlikely given the UHV conditions.

### 7.2.2 Spectroscopy results

In principle, the self-assembled structures observed for the reaction products could also be realized by non-reacted *para*-compounds and octylamine molecules forming hydrogen bonds with each other. To obtain spectroscopic confirmation that this is not the case and that an *in-situ* 2D surface reaction has occurred, we performed x-ray photoelectron spectroscopy (XPS) and near-edge X-ray adsorption fine structure (NEXAFS) spectroscopy studies at the beamline HE-SGM at BESSY II.

<sup>5</sup>In this experiment the molecules were evaporated onto a sample held at RT.

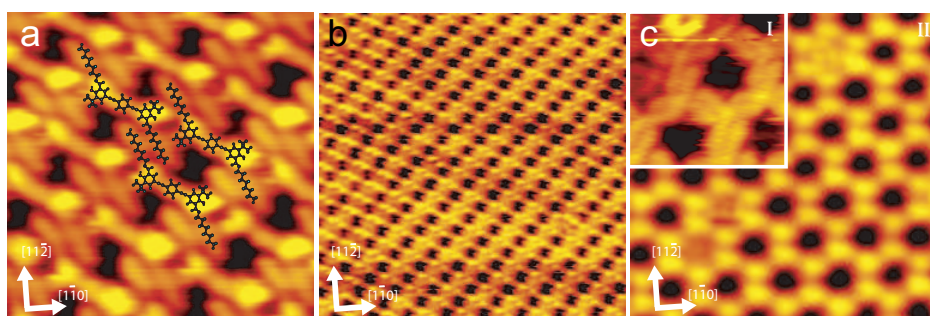


Figure 7.7: STM images obtained after deposition of the *ex-situ* reaction product and subsequent annealing to 450 K: (a) Zoom in on an ordered island (size  $80 \times 80 \text{ \AA}^2$ ). (b) Large-scale image (size  $300 \times 300 \text{ \AA}^2$ ). (c) Honeycomb structure. Image I: Honeycomb structure co-existing with the *ex-situ* product domains in (a,b)  $50 \times 50 \text{ \AA}^2$ . Image II: Pure honeycomb phase observed by lower evaporation temperatures (here 403K) (size  $150 \times 150 \text{ \AA}^2$ ).

### NEXAFS

In Fig. 7.8  $C_{1s}$  NEXAFS spectra of the reactants as well as the *ex-situ* and the *in-situ* synthesized reaction products on the Au(111) surface are shown.

The reference spectra were obtained for a saturated monolayer of octylamine<sup>6</sup>, a saturated monolayer of the *para*-compounds<sup>7</sup>, and a multilayer of the *ex-situ* product. For the *in-situ* reaction 1/3 of saturation coverage of *para*-compounds was evaporated<sup>8</sup>, and the sample was subsequently cooled to 239 K and exposed to 27 L octylamine, resulting in multilayer adsorption of octylamine. The sample was then annealed to 410 K to desorb multilayers and complete the reaction.

The peaks can be assigned from literature values<sup>9</sup>. The peak at  $E_{\pi_{1*}} = 284.9 \text{ eV}$  is attributed to a superposition of peaks arising from carbon on the aromatic backbone and is shared by the *para*-compound as well as *ex-situ* and *in-situ* reaction products. Small shifts in the  $\pi_1$  positions arise from the difference between a chemisorbed monolayer and a physisorbed multilayer. As expected, the peak assigned to these aromatic carbons is absent for the octylamines which only show a broad resonance arising from  $\sigma$ -orbitals of the alkyl chains. The peak at  $E_{\pi_{1*}} = 286.3 \text{ eV}$  stems from the carbon in the aldehyde group and is present for the *para*-compound and absent for the *ex-situ* product which does not contain an aldehyde group. For the *in-situ* product (red curve) the aldehyde peak is significantly reduced, which is the expected spectroscopic signature of formation of the imine. (A peak for imine-carbon is not observed in the spectrum as it is expected to be superimposed on the peaks arising from aromatic carbons).

<sup>6</sup>Multilayers were deposited at 108 K and the sample was then heated to 260 K.

<sup>7</sup>Multilayers were deposited at RT and the sample was then heated to 435 K.

<sup>8</sup>The coverage was determined using XPS

<sup>9</sup>Literature values of 284.5 eV for aromatic C [234], 286.6 eV for carbonyl C [234], and 285.9 eV for imine C [235]

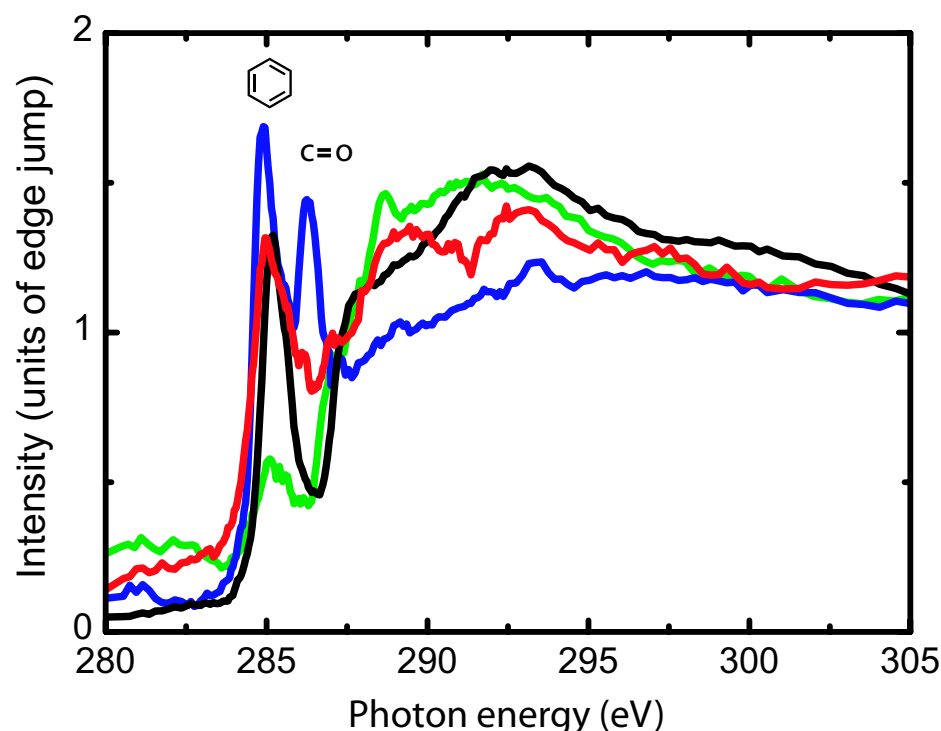


Figure 7.8: Carbon 1s NEXAFS spectra. The spectra are obtained at a  $30^\circ$  incidence and shows octylamine (green), *para*-compound (blue), *ex-situ* reacted imine product (black), and the *in-situ* reacted imine product (red).

## XPS

Further evidence for the *in-situ* reaction was obtained by XPS measurements. Fig. 7.9 shows the  $O_{1s}$  XPS spectra for the *para*-compound (coverage  $\sim 1/3$  ML) and the *in-situ* synthesized reaction product on the Au(111) surface.

Since the oxygen coverage is rather low in the experiments the oxygen peaks are small and the signal-to-noise ratio is poor. Even so, the spectra show a reduction of the oxygen peak upon *in-situ* reaction. This is the expected result in the case of a completed reaction in which case the oxygen of the carbonyl group will disappear and desorb as  $H_2O$ . (The oxygen on the hydroxyl group should still be present upon reaction.) The XPS results thus indicate that the reaction goes to completion which further implies that the imine reaction product and not the hemiaminal transition product is formed.

### 7.2.3 DFT calculations

It is surprising that the imineformation proceeds under the extreme UHV conditions, because in the conventional reaction scheme (Fig. 7.1), the last step, in which the tetra-

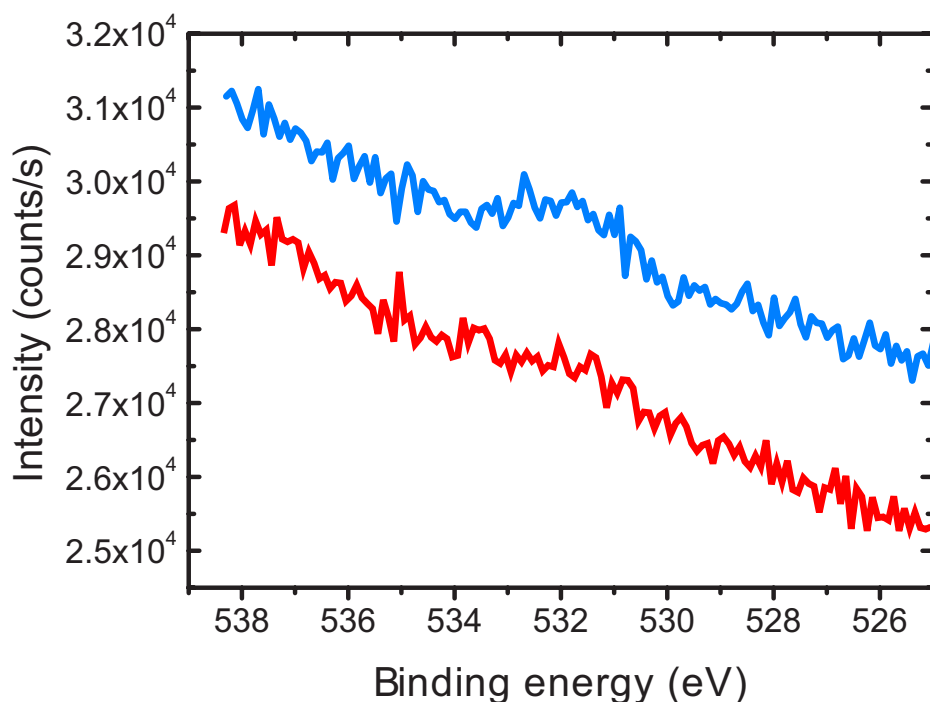


Figure 7.9: Oxygen 1s XPS spectra of the *para*-compound (blue), and the *in-situ* reacted imine product (red).

hedral intermediate is converted into the imine product, is normally catalyzed by the solvent, which acts as a combined proton donor/acceptor. To establish a plausible reaction path in the absence of a solvent, state-of-the-art, ab-initio DFT calculations<sup>10</sup> were performed using the DACAPO code with the PW91 exchange-correlation functional<sup>11</sup> (Fig. 7.10). For simplicity, and to reduce the computational load, the amine and *para*-compound were cut off beyond the reacting groups and saturated with hydrogen atoms as shown in the start configuration (1). In the first step of the reaction path the amino group undergoes a nucleophilic addition to the carbonyl group under the formation of the tetrahedral intermediate, in this case a hemiaminal, as in the conventional reaction scheme (2). Next, the phenol hydroxyl group donates a proton to the hydroxyl group of

<sup>10</sup>The calculations were performed by Mats Dahlbom and Bjørk Hammer.

<sup>11</sup>The molecules were described in a large ( $17 \times 15 \times 10 \text{ \AA}^3$ ) repeated super cell, and the wave functions were expanded on a basis of plane waves with energy up to 25 Ry. Ultrasoft pseudopotentials were used to describe the atomic cores. The population of the one-electron states was stabilized by a broadening of the states according to Fermi statistics at  $k_B T = 0.1 \text{ eV}$ . The reaction energy pathways and transition states were determined using the Climbing Nudged Elastic Band method. The positions of the  $N = 48$  atoms in the setup were optimized until the  $3N$  norm of the  $3N$  forces perpendicular to the individual reaction paths were smaller than  $0.2 \text{ eV/\AA}$ , or until the energy barrier was insignificant compared to the barriers along other parts of the reaction paths.



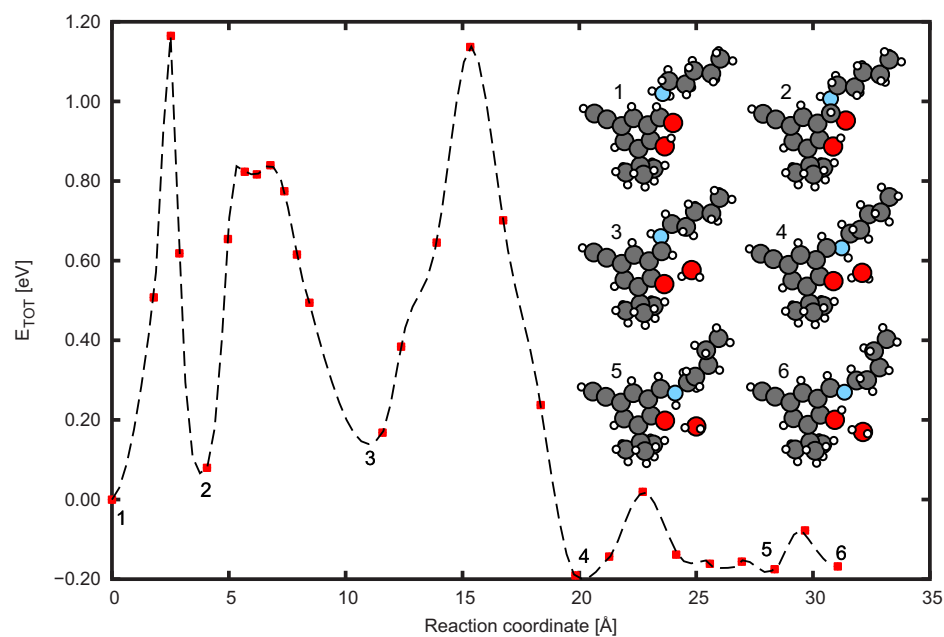


Figure 7.10: Optimum reaction pathway identified from theoretical modelling. The numbers on the graph correspond to the shown molecular conformations.

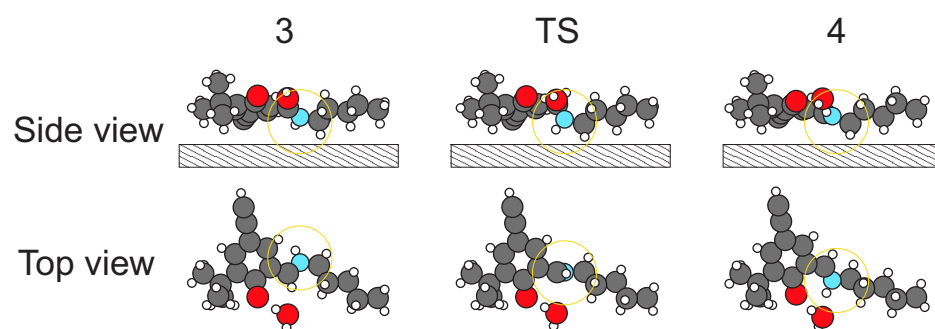


Figure 7.11: Calculated atomic structures during the rotation from the local energy minima 3, during the transition state (TS) to the local minima 4. Both top and side views are shown and a schematic metal surface is added in the side views.

the hemiaminal, and water is eliminated (3). Finally, a rotation around the bond between the phenyl ring and the iminium carbon atom takes place, and the iminium group donates a proton to the phenoxy group (4, 5 and 6). By further examination of the rotation from (3) to (4) (Fig. 7.11), we observe that the conformational changes in the molecules are largely localized to the region highlighted by the orange circle. This supports the assertion that the molecules need not detach from the surface during the rotation. The calculated barriers for the gas phase reaction consequently also provides a reasonable estimate for the barrier of rotation for adsorbed molecules.

In this reaction pathway all energy barriers are below 1.17 eV, enabling the reaction to proceed at the annealing temperature of 400 K<sup>12</sup>. In the experiments we observed that imineformation also proceeds on a sample held at room temperature. This observation indicates the existence of a more favourable energy pathway or reduced energy barriers caused by catalyzing effects of the underlying metal substrate. An important feature of the proposed reaction mechanism is that the phenol hydroxyl group acts as an internal proton donor/acceptor and thereby substitutes the solvent present under normal solution phase conditions. A direct conversion of the tetrahedral intermediate into the imine product in the absence of a proton donor/acceptor group has previously been shown to result in an energy barrier of  $\sim 2.4$  eV [236], which would make the reaction unlikely at moderate temperatures.

#### 7.2.4 Discussion

The STM measurements of the *in-situ* and *ex-situ* reaction products clearly revealed the formation of identical molecular structures. Furthermore, the NEXAFS results evidenced a removal or replacement of the carbonyl group during the surface mediated reaction. The combination of both experimental techniques thus show that covalent imine bonds were formed upon co-evaporation of the reactants in UHV.

From the STM images obtained after thermal activation, we exclusively observed reaction products (both *in-situ* and *ex-situ*) with the chiral RR/LL conformation of the backbone. The reactants, originally assuming both chiral and achiral conformations, are thus chirally steered by the reaction and subsequent island formation. We interpret the observed chiral steering to result from conformational switching of the backbone, as observed for the individual *para*-compounds after or during reaction.

The position of the alkyl chains with respect to the molecular backbone matches the conformation of the reaction product stabilized by an intramolecular hydrogen bond between the imine nitrogen atom and the hydroxyl group. The adopted configuration of the reacted alkyl chains observed on the condensed molecules is thus identical to the optimum configuration for gas phase molecules.

### 7.3 Threespoke-compound and octylamine

All investigations of the reaction between the *threespoke*-compound and octylamine on the Au(111) surface in UHV were performed with STM. As for the *para*-compound the

<sup>12</sup>An Arrhenius expression gives 0.02 reaction events per second with a prefactor of  $10^{13} \text{ s}^{-1}$ .



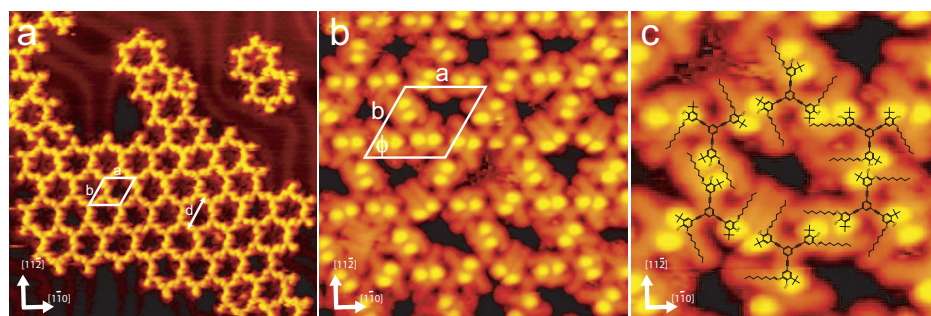


Figure 7.12: STM images obtained after co-deposition of the *threespoke* reactant and octylamine at room temperature: (a) Large scale image of the *in-situ* structure ( $400 \times 400 \text{ \AA}^2$ ) obtained in the  $\pi$ -system imaging mode. (b) Medium scale ( $150 \times 150 \text{ \AA}^2$ ), and (c) small scale ( $80 \times 80 \text{ \AA}^2$ ) images of the *in-situ* structure obtained in the *tert*-butyl imaging mode.

reaction carried out *in-situ* was compared with the reaction product synthesized *ex-situ* and deposited directly on the Au(111) surface by vapour deposition. Furthermore, the *in-situ* reaction was carried out by two different preparation procedures to investigate how kinetic parameters influence the reaction outcome. In the first preparation procedure a submonolayer of *threespoke* reactants was exposed to a low flux of octylamines at room temperature, whereas in the second preparation the sample with *threespoke* reactants was cooled below reaction temperature and saturated with octylamines.

### 7.3.1 In-situ reaction

In both preparation procedures to perform the reaction *in-situ* for imaging with STM, the *threespoke*-compounds were deposited on the Au(111) surface at a coverage below  $1/3 \text{ ML}$ , as estimated by STM. Details on the four adsorption structures formed can be found in Chapter 4.

#### Room temperature deposition

In the first preparation procedure the Au(111) surface containing *threespoke*-molecules was held at room temperature and exposed to octylamines ( $p \sim 1\text{--}5 \times 10^{-7} \text{ mbar}$ ). Based on the experiments with the *para*-compound the reaction is expected to run during this deposition step. Subsequently, the sample was briefly annealed to a temperature between 400 and 450 K. For imaging with STM the sample was cooled down in the STM to a temperature of 120–170 K. This procedure resulted in the formation of large ordered porous networks with pore diameters,  $d$ , of approximately 4 nm, as shown in the STM images of Fig. 7.12. Only one adsorption structure was observed.

The porous structure formed is clearly different from the structures formed by the individual reactants. In the structure six *threespoke*-molecules have arranged into a hexagon with the ethynylene-spokes meeting pairwise head-to-head, as seen in Figs.

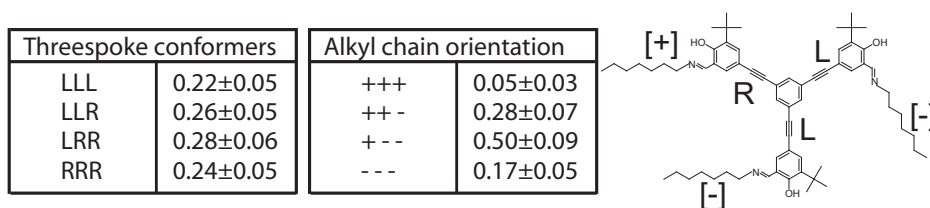


Figure 7.13: (a) Distribution of the different conformations of the *threespoke* backbone. (b) Distribution of alkyl chains with the conformation allowing an intramolecular hydrogen bond. (c) Model compound explaining the nomenclature.

7.12b and 7.12c. Each *threespoke*-molecule belongs to three such hexagons, resulting in the extended hexagonal network. The alkyl chains are attached to the aromatic head-groups at the site opposite to the *tert*-butyl group, as expected for the reaction product, and are observed to extend into the pores. The ethynylene-spokes are all oriented along a  $\langle 11\bar{2} \rangle$  direction, and the orientation of the backbones alternates between the "up" and "down" orientation around the pores<sup>13</sup> (see eg. Fig. 7.3b). The high orientational order of the backbones implies that the structure also has a definite orientational relationship with the symmetry directions of the underlying substrate lattice. From measurements<sup>14</sup> on the STM images, we can assign a hexagonal unit cell to the structure containing two molecules with the dimensions:  $a = (39.8 \pm 2.2) \text{ \AA}$ ,  $b = (39.8 \pm 2.2) \text{ \AA}$ ,  $\phi = 60^\circ \pm 3^\circ$ , and  $(\angle a; \langle 11\bar{2} \rangle) = 0^\circ \pm 3^\circ$ . Unit cells are marked on the STM images in Figs. 7.12a and 7.12b.

As seen in the STM images of Figs. 7.12b and 7.12c obtained in the *tert*-butyl imaging mode, the structure is not conformationally ordered. A quantitative analysis of high resolution STM images reveals that the four different surface conformations (RRR, RRL, LLR, LLL) of the *threespoke* backbone is found with nearly equal probability which implies that the RRL/LLR conformation appears with a lower probability than expected for a random distribution<sup>15</sup> (see the table in Fig. 7.13a). Furthermore, the orientation of the alkyl chains is less ordered than observed for the reacted *para*-compound. As shown in Fig. 7.13c, an alkyl chain can obtain two different orientations which can be termed + and -. In the + configuration an intramolecular hydrogen bond between the hydroxyl group and the imino group can exist. As seen in Fig. 7.13b, most of the *threespoke* products have only one out of three alkyl chains in the favored + orientation. In contrast, for the similar *para*-product, + orientations were assumed for all alkyl chains.

The molecular conformations are also in this case strongly affected by the interactions to the neighboring molecules. Since the molecules meet head-to-head around the

<sup>13</sup> An adsorption configuration in which the spokes are oriented along the  $[11\bar{2}]$  direction can be realized in two distinct ways, "up" and "down", related by a  $60^\circ$  rotation of the molecule, as discussed in Chap. 4.

<sup>14</sup> Only the positions of the aromatic backbones are considered, i.e. molecular conformations are not taken into account

<sup>15</sup> Assuming all surface conformers were equal in energy, a random distribution of (RRR, RRL, LLR, LLL) = (1/8, 3/8, 3/8, 1/8) is expected.

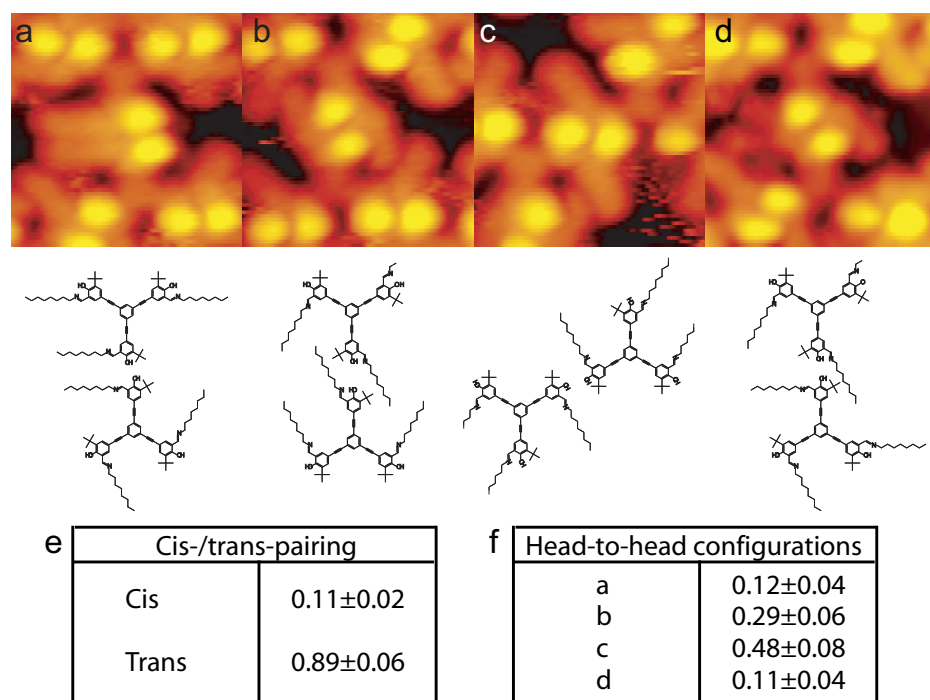


Figure 7.14: STM images of the different connection possibilities with models below the images, and tables showing the distributions: (a) Cis configuration. (b-d) Trans configurations. (Image sizes  $40 \times 40 \text{ \AA}^2$ ) (e-f) Distributions of head-to-head arrangements. a-d refer to the arrangement in the respective STM images

hexagon, the head-groups can assume either a *cis* configuration (Fig. 7.14a) or a *trans* configuration (Figs. 7.14b-d). As for both the reacted and unreacted *para*-compound there is a preference for the molecules to pair up in a *trans* fashion. The *cis/trans* statistics in Fig. 7.14e stem from the analysis of 225 head-to-head pairings counted at images obtained at a temperature between 120 K and 147 K. The energy difference estimated by use of Boltzmann statistics between the favoured/unfavoured *trans/cis* arrangement is thus 0.02-0.03 eV, and thereby similar to the interactions found for the structures formed by the oligo-phenylene-ethynylene reactants. A further level of complexity arises from the orientation of the alkyl chains. The possible orientations are shown in the molecular models of Fig. 7.14. The statistics in Fig. 7.14f show that alkyl chains belonging to groups meeting head-to-head preferentially assume identical orientations with the configuration in Fig. 7.14c being the most abundant. (The arrangement in Fig. 7.14a is the only sterically allowed *cis* configuration.) Since the alkyl chains are not visible in all STM images, the statistics in the table of Fig. 7.14f is poorer than in the table of Fig. 7.14e.

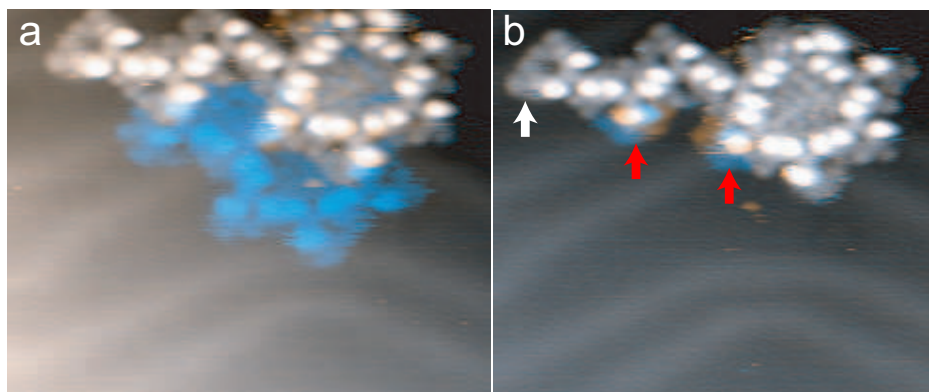


Figure 7.15: Dynamics of the reacted *threespoke*-molecules shown by overlay of STM images where blue/orange correspond to the initial/final configuration. (a) Molecules (blue) leaving the island. (b) Conformational changes. The red arrows mark switches around ethynylene spokes whereby the *tert*-butyl group and alkyl chain interchange positions. The white arrow marks orientational shifts for an alkyl chain.

### Dynamics

From STM movies we can investigate dynamical phenomena for the reacted *threespoke*-molecules. The blue/orange colour coded STM images shown in Fig. 7.15 are selected from a movie obtained at a temperature of  $\sim 168$  K.

We observe both attachment and detachment from islands which implies that the structures interchange molecules with the lattice gas. In Fig. 7.15a molecules originally embedded in an island (blue) are seen to detach and diffuse into the lattice gas. In the image sequence obtained prior to such a detachment event, the part of the island, which is about to leave, is imaged more fuzzy than the rest of the structure, indicating a decreased binding of the leaving cluster. Occasionally we observe single molecules or perhaps two-membered islands partly stabilized at the elbows of the Au(111) herringbone reconstruction. This indicates that the diffusivity of the reacted molecules is reduced compared to the reactants which were never observed individually. (Images of such small molecular clusters of reacted *threespoke*-molecules are slightly disturbed, probably due to diffusion events.)

The alkyl chains attached to the *threespoke* backbone are mobile at the imaging temperature and are thus sometimes imaged with a v-shape revealing both the + and – configuration at the same time. Such a fast switching between the + and – configuration is often observed for molecules at island boundaries. An example is marked by the white arrow in Fig. 7.15b. Shifts of alkyl chain orientation are also occasionally observed in the interior of the islands (see e.g. the alkyl chain pointing to the left in Fig. 7.14d). Since the alkyls can be imaged as if they were present at both positions at the same time, the rates for these orientational switches are high compared to the scanning speed. This implies that if a hydrogen bond is formed in the "+"-position, it is not expected to be

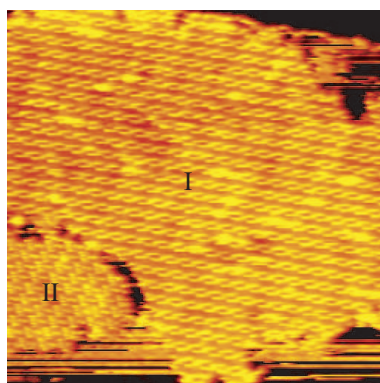


Figure 7.16: STM images of the row (I) and ladder (II) adsorption structure observed after a preparation where the *threespoke*-molecules were cooled sufficiently to be condensed into islands prior to octylamine exposure and subsequent annealing. (Image size  $850 \times 850 \text{Å}^2$ ).

stronger than  $0.4 \text{eV}^{16}$ . DFT calculations [237] foresee similar hydrogen bonds to be rather strong ( $0.37 - 0.78 \text{ eV}$ ). In summary, this implies that the  $+/-$  ordering of the alkyl chains can happen during and after nucleation of the molecules, and we expect the ordering observed in the structures to be influenced mainly by steric effects in the pores.

The overlay images in Fig. 7.15b show that the adsorbed *threespoke*-molecules are still able to switch conformation spontaneously by rotations around the ethynylene spokes after reaction. Two such switching events, from blue to orange, are marked by red arrows. Since the switches are observed for similar sample temperatures as was the case for the *threespoke* reactant (and the other oligo-phenylene-ethynylene group members), the energy barrier ( $\sim 0.3 \text{ eV}$ ) towards switching is presumably not changed significantly upon reaction. This indicates that the attached alkyl chains do not have a strong bonding to the surface (as is also revealed by the high orientational switching rate of the alkyl chains).

### Low temperature deposition

In the second preparation procedure the Au(111) surface containing *threespoke* molecules was cooled to a temperature below 170 K and exposed to octylamines ( $p \sim 1 - 5 \times 10^{-7} \text{ mbar}$ ). At this temperature multilayers of octylamine grow on the sample. After deposition, the sample was briefly annealed to a temperature between 300 and 400 K to desorb multilayers and initialize the reaction. For imaging with STM the sample was cooled to a temperature between 120 and 170 K. Upon this preparation procedure two co-existing adsorption structures were observed, which we will term the row and

<sup>16</sup>The estimate is based on an assumed Arrhenius behavior for the orientational switching with a lower limit for the rate of  $10 \text{ s}^{-1}$  and a tentative prefactor of  $10^{13} \text{ s}^{-1}$ .

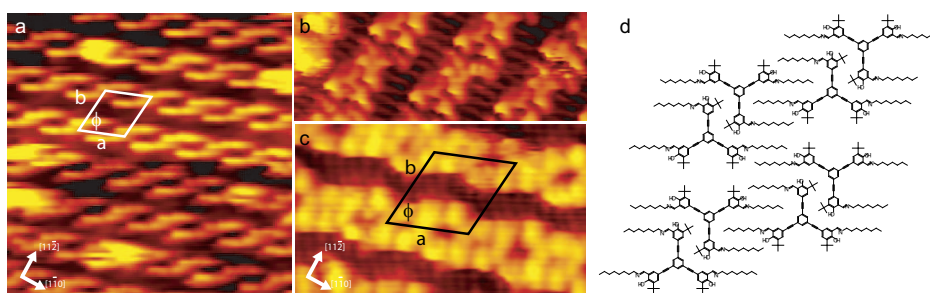


Figure 7.17: STM images and model of the row structure. (a) STM image obtained in the *tert*-butyl imaging mode. Due to a low resolution each bright line corresponds to two *tert*-butyl groups (image size  $225 \times 225 \text{ \AA}^2$ ). (b) High-resolution STM image in the *tert*-butyl imaging mode (image size  $135 \times 50 \text{ \AA}^2$ ), and (c) in the  $\pi$ -system imaging mode (image size  $135 \times 80 \text{ \AA}^2$ ). (d) Tentative molecular model.

ladder structure, as marked by "I" respectively "II" in Fig. 7.16<sup>17</sup>. Both structures are built up of flat-lying *threespoke*-molecules with alkyl chains extending from the site opposite to the *tert*-butyl groups.

In the row structure the ethynylene spokes of the *threespoke*-molecules are oriented along the  $\langle 11\bar{2} \rangle$  directions and the *threespoke*-molecules close-pack pairwise with an end-group of one ethynylene spoke lying in the vertex of the neighboring molecule (see Fig. 7.17b,c). In a given domain all these connections are either of the "r" or the "I" type<sup>18</sup>. The molecular pairs are arranged into long rows with the alkyl chains forming a lamellar motif between the rows. The structure is homochiral consisting exclusively of either molecules with the RRL or the LLR conformation, arranged in a completely ordered fashion, as shown in Fig. 7.17c. In the domains shown in Fig. 7.17b,c all the tilings are of the "r" type and all *threespoke* backbones of the RRL conformation. Furthermore, the orientation of the alkyl chains are completely ordered with a "-" orientation observed for the molecular R-spoke positioned in the vertex of the pairing molecule and "+" orientations for the other two other spokes. Each molecule thus obtains a configuration allowing for two intramolecular hydrogen bonds. We can assign a unit cell to the structure containing two molecules, with  $a = 33.4 \pm 1.8 \text{ \AA}$ ,  $b = 36.1 \pm 1.8 \text{ \AA}$ , and  $\phi = 63^\circ \pm 5^\circ$ .

Also in the ladder structure the *threespoke*-molecules close-pack pairwise with the end-group of one ethynylene spoke lying in the vertex of the pairing molecule. Within a given domain all such pairings are either of the "r" or "I" type (see Fig. 7.18). The molecular pairs are joined into long rows in a *trans* head-to-head fashion (as marked with a dashed circle in Fig. 7.18b). The alkyl chains fill out the space between the *threespoke* rows, by forming an interwoven structure. The conformation and arrangement of the

<sup>17</sup>Experiments following this preparation procedure were only performed successfully two times. We therefore cannot rule out that additional structures exist.

<sup>18</sup>See Fig. 4.16 in Chap. 4 for a drawing of the "r" and "I" coupling which was observed in all the structures formed by the *threespoke* reactants.



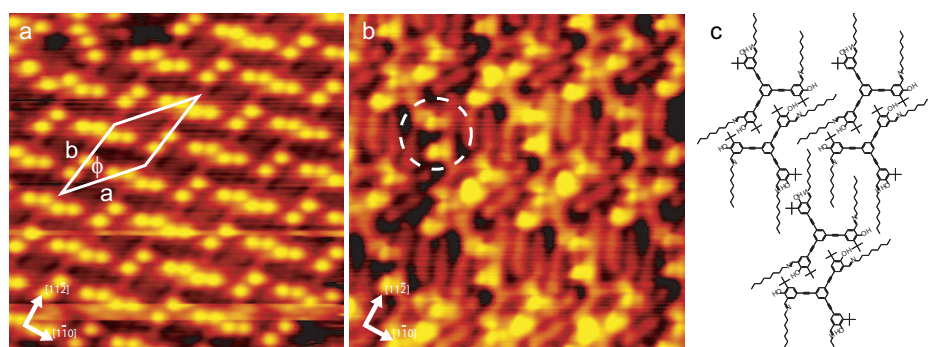


Figure 7.18: STM images and model of the ladder structure. (a) STM image obtained in the *tert*-butyl imaging mode (image size  $160 \times 160 \text{ \AA}^2$ ). (b) High-resolution STM-image (image size  $100 \times 100 \text{ \AA}^2$ ). The dashed circle marks two molecular end-groups meeting in a *cis*-configuration. (c) Tentative molecular model.

molecules is completely ordered: For domains with "r" ("l") type molecular pairs all *threespoke* backbones are of the RRL (LLR) conformation with a "-" orientation of the alkyl chain on the L (R) spoke and "+" orientations on the two R (L) spokes. The overall structure is thus homochiral with a clear correlation between the chirality of the tiling pattern and the molecular backbones. For a tentative model see Fig. 7.18c. We can assign a unit cell to the structure with dimensions,  $a = 41.5 \pm 2.1 \text{ \AA}$ ,  $b = 43.6 \pm 2.2 \text{ \AA}$ , and  $\phi = 35^\circ \pm 5^\circ$ . We observe some ladder domains where the ethynylene spokes are not oriented along the  $\langle 11\bar{2} \rangle$  directions.

The molecular arrangements in the row and ladder structure formed by the reacted *threespoke*-molecules are very similar. Both structures are homochiral, built up of molecules with the RRL (LLR) conformation forming "r" ("l") molecular pairs. Furthermore, the attached alkyls are oriented in the "+" fashion on two of the three molecular spokes. If the arrangement of backbones of reacted *threespoke*-molecules in the row (ladder) structure is compared with the arrangement in the row (open ladder) structure for the unreacted *threespoke*-compounds, see Chapter 4, the similarity is striking (see Fig. 7.19). The molecular pairs for the ladder structure formed by reacted compound is identical to the pairs in the open ladder structure formed by the *threespoke* reactant and the molecular pairs in the row structure of the reacted compounds can be realized from the pairs in the row structure of the unreacted compounds by only one conformational switch around an ethynylene spoke, as marked with the red dashed circle. Note that the reacted and unreacted structures are only locally similar. To form the reacted structures by reacting octylamine to the *threespoke*-molecules in the unreacted structures, the unreacted structures must open up to leave space around the molecular pairs for the extending alkyl chains.

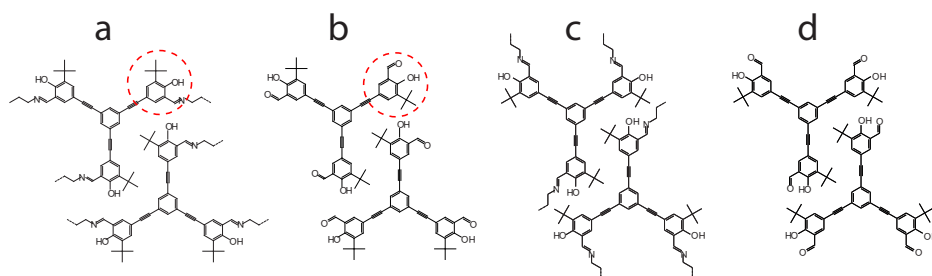


Figure 7.19: Most favoured molecular pairs. Row (a) and ladder (c) structure for the reacted *threespoke*-molecules. Row (b) and open ladder (d) structure for the unreacted *threespoke*-molecules.

## Discussion

The two preparation procedures resulted in the formation of very different molecular phases. The procedure where both compounds were dosed at room temperature resulted in the formation of an open and less conformational ordered structure. In contrast, the procedure where the *threespoke*-molecules were allowed to condense into islands prior to octylamine exposure yielded dense-packed structures with a complete conformational order. Even upon annealing to 400 K it was not possible to induce a phase transition from one of the structures to the other.

We speculate that the formed structures are a result of competing kinetic and thermodynamic factors. Normally, the structure formed at the highest temperature is expected to be the thermodynamically most stable structure, but the higher conformational order and denser packing observed in the low temperature structures indicate that this might not be the case here.

In the first preparation procedure we expect that most *threespoke*-molecules are not bound in molecular islands during deposition and reaction with the octylamine molecules. In this scenario, conformationally unordered reacted molecules are formed that are free to diffuse on the surface. Upon cool down the products condense into islands, as observed. Since the conformation of the molecules is not sufficiently well-ordered to close-pack without a large number of conformational changes, the molecules adopt the more conformationally unordered hexagonal structure, which would then be a meta-stable kinetic structure. Since the hexagonal structure is loosely packed the molecular conformations can furthermore be adjusted by conformational changes after condensation. Even at low temperatures (168 K) we observe that molecules can escape this structure. We therefore suppose that the structure is dissolved at the annealing temperature of 400 K, and re-formed upon cooling.

In the second preparation procedure the *threespoke* reactants are condensed into islands before exposure to octylamine. Assuming that the islands are not completely dissolved at the reaction temperature, octylamines should attach to the already condensed *threespoke* reactants. Due to the conformational order of the *threespoke* reactants and the steric hindrance in the networks, the products are potentially forced into the right



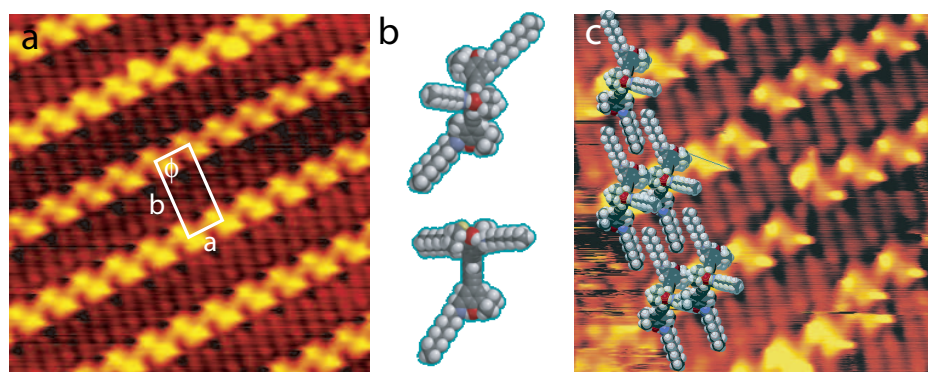


Figure 7.20: The structure formed after deposition of the *ex-situ* reacted *threespoke* product. (a) STM image of defect free region. (Image size  $120 \times 120 \text{ \AA}^2$ ). (b) Upright-standing molecule seen from two angles. (c) STM image with upright-standing molecular models.

conformation upon reaction. This can account for the more dense-packed structures observed, which are thus expected to be thermodynamically more stable, since they inherit parts of the energetically stable arrangement of the reactants with an associated high van der Waals attraction.

The observed differences in the molecular conformations based on the preparation conditions indicate that well-ordered covalently linked 2D structures can be realized if the reactants are allowed to preassemble before reaction. To take advantage of this, model systems should be designed, e.g. by directional hydrogen bonds, where the geometry of the preassembled structure matches the bonding pattern of the desired surface polymer.

### 7.3.2 Ex-situ reaction

For comparison with the *in-situ* reaction products, the imine *threespoke* product was synthesized *ex-situ* by conventional solution phase chemistry techniques. Upon evaporation onto the Au(111) substrate by vapour deposition and imaging with STM, the molecular structure shown in Fig. 7.20 was observed. During evaporation the crucible holding the molecules was heated to  $\sim 391 \text{ K}$ .

The structure formed by *threespoke* products synthesized *ex-situ* is clearly different from the structures formed by the reaction products reacted *in-situ*. The STM-image in Fig. 7.20a reveals long rows of bright asymmetric protrusions with a lamella arrangement between the rows. We attribute two bright protrusion and two alkyl chains to each molecular entity, since STM movies reveal that such units are able to move individually (see Fig. 7.21). We can assign a nearly rectangular unit cell to the structure containing a single molecular unit. The unit cell dimensions are  $a = (11.8 \pm 0.6) \text{ \AA}$ ,  $b = (28.0 \pm 1.4) \text{ \AA}$ , and  $\phi = 91^\circ \pm 3^\circ$  (see Fig. 7.20a).

It is not possible to fit a flat-lying *threespoke* product to a molecular unit. However, if

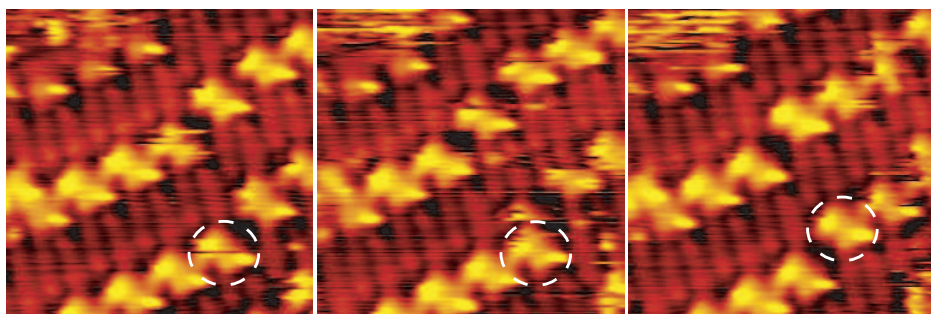


Figure 7.21: Image sequence from an STM movie. The dashed circle marks an "upward" moving molecule. (Image sizes  $70 \times 70 \text{ \AA}^2$ )

we instead draw the molecules in an upright standing position with one spoke pointing upwards, they match the structure perfectly (Fig. 7.20b,c). In this upright-standing scenario the two bright protrusions correspond to the *tert*-butyl group and the alkyl chain on the upward-pointing molecular head-group. The alkyl chains belonging to the two additional spokes form the lamella structure between the rows.

In contrast to the *in-situ* products which were stable at annealing temperatures above 500 K, the *threespoke* products synthesized *ex-situ* desorb upon annealing to 400 K. Consequently, the structure is not bound very strongly to the substrate. This is most probably a consequence of the upright-standing geometry resulting in a weaker interaction between the molecule and substrate.

As for the *ortho*-compound investigated in Chap. 5, we expect the upright-standing geometry to be favoured by  $\pi$ -stacking between the aromatic backbones of neighboring molecules. Furthermore, molecules with an upright-standing geometry can form three intramolecular hydrogen bonds between the nitrogen lone-pair and the hydroxyl groups. Such intramolecular hydrogen bonds could stabilize the structure further.

Since we know that the *ex-situ* synthesized *para*-product undergoes some decomposition upon deposition we cannot fully rule out that the structure observed for the *ex-situ* synthesized *threespoke* product does not consist of fragmented molecules. It is, however, less likely since all entities appear identical in the STM images.

### 7.3.3 Discussion

We can only speculate why the *ex-situ* and *in-situ* reacted *threespoke*-molecules do not form similar adsorption structures. However, as the strength of each potential intramolecular hydrogen bond is expected to be  $\sim 0.4$  eV and thus comparable with the interaction between an aromatic molecular spoke and the Au(111) surface ( $\sim 0.3$  eV), additional  $\pi$ - $\pi$  stacking effects can render the upright adsorption configuration the more energetically favourable.

In this scenario the flat-lying adsorption geometry observed for the *in-situ* reacted *threespoke*-molecules is caused by the reaction conditions: Since the preadsorbed *threespoke* reactants obtain a flat-lying adsorption configuration with a bonding to the surface

of at least 1 eV<sup>19</sup>, an upright-standing configuration after reaction can only be obtained if the *in-situ* products rise up. To do that the molecule has to overcome a similar energy barrier. If we assume an attempt frequency of 10<sup>6</sup>, as observed for the partly desorption/switching of the single ethynylene spokes, this should not happen at temperatures below 500 K.

## 7.4 Conclusion

In the present chapter it was demonstrated for two hetero-compound model systems that imineformation can proceed on a Au(111) surface under UHV conditions. Whereas the straight *para*-compound only formed one structure, the tripodal *threespoke*-compound formed a number of condensed structures depending on the reaction conditions.

There are a number of common trends in the structures. Both the *para*-product and *threespoke* product form structures in which the adsorption orientation of the aromatic backbone is similar to the orientation observed for the pure aromatic reactants. If the reacted molecules meet head-group to head-group in the structures, the head-groups preferentially obtain a *trans* arrangement, as also observed in the brick-wall phase of the *para*-reactant. Upon reaction all alkyl chains observed are straight (ie. they do not contain gauche defects), and alkyl chains on neighboring molecules are often found to form side-to-side lamella arrangements, as observed for pure octylamine.

However, there are also differences. Of particular interest is the upright orientation adopted exclusively by the *ex-situ* formed *threespoke* product. This shows that certain large complex organic molecules must be synthesized on the surface to form real 2D molecular networks. Furthermore, depending on the preparation conditions we observed a large variety of the phases for the *in-situ*-reacted *threespoke*-molecule. This indicates that the self-assembly of organic molecules may be important for the formation of ordered covalently linked networks. If highly ordered semi-stable molecular networks, formed by eg. hydrogen bond formation or metal complexation, are used as a reactive template, ordered covalently bound networks should be achievable by exposure with reactive partners of matching dimensions.

---

<sup>19</sup>The investigation of conformational changes revealed that each ethynylene spoke was attached to the surface by at least 0.3 eV.



## CHAPTER 8

---

### Polycondensation on Au(111)

---

The formation of nanoarchitectures by self-assembly has been studied extensively on metal surfaces under UHV conditions. In contrast, similar studies of surface structures based on covalent chemistry are surprisingly scarce. In this chapter, the formation of two-dimensional surface polymers is explored and it will be demonstrated that the connectivity of the formed polymers depends on the kinetics during preparation. Furthermore, the local bonding pattern will be investigated with STM focusing on connectivity, branching points, and ring or chain formations.

## 8.1 Introduction

In the previous chapter we demonstrated the formation of imine bonds between co-adsorbed aldehydes and amines on the Au(111)-(22 ×  $\sqrt{7}$ ) surface under ultrahigh vacuum conditions. In this chapter we will apply a similar condensation reaction to form a two dimensional polymeric network. By STM we investigate the local bonding pattern of the polymeric network with focus on connectivity, branching points, and ring or chain formation. We find that the connectivity of the polymeric network can be manipulated by controlling the kinetics during the preparation procedure, and that polymers with a high connectivity contain domains with chain or pore formations. The size distribution of the formed pores correlates with molecular geometry and strain.

### 8.1.1 Investigation of polymers

Polymers are giant molecules made up of many repeat units covalently joined together in the form of a long chain. A gel is the 3D version of a polymer and can be defined as a material composed of subunits that are able to bond with each other in such a way that one obtains a network of macroscopic dimensions, in which all the subunits are connected by bonds [238].

The geometry, bonding pattern and size of polymers and gels have been studied extensively in solution phase chemistry [78, 239]. If conventional analysis methods are applied only information on the average ordering is obtained. To receive information on the local bonding pattern, local techniques, such as scanning probe techniques, are crucial. Recently, investigations of the geometry, conformation, bonding pattern and size of large macromolecules on surfaces, such as molecular sheets [240], chains [241], DNA-helices [242] and macrocycles [243] have been performed in UHV using the pulse injection technique which minimizes decomposition [244]. At the liquid-solid interface polymer architecture and folding has been studied based upon drop-casting [245–248] and spin coating [249] of polymers synthesized in solution or alternatively upon electropolymerization directly on the surface [103, 104].

Synthetic polymers and gels have played a large role in the development of new materials and polycondensation reactions have been applied in the synthesis of widely used materials such as nylon, terylene<sup>1</sup> and kapton [166]. Similarly, the growth of thin organic polymer films is of great interest for the electronic, optic and display industries, and a number of studies into polyimine [82, 233] and polyimide [81, 83, 84, 250] thin films by vapour deposition polymerization exist, with the most studied system being the coupling reaction between pyromellitic dianhydride (PMDA) and oxydianiline (ODA) [81, 83].

Compared to thin films the formation of truly two-dimensional networks by polymerization directly on a surface has been less investigated, and STM studies have focused on the unwanted self-polymerization of methyl pyruvate on Pd(111) under UHV conditions [67, 85], the topochemical polymerization of diacetylene in both UHV, at the air-solid and at the liquid-solid interface [79, 91, 94], and on the synthesis of homo or hetero

---

<sup>1</sup>Terylene is often simply called polyester.

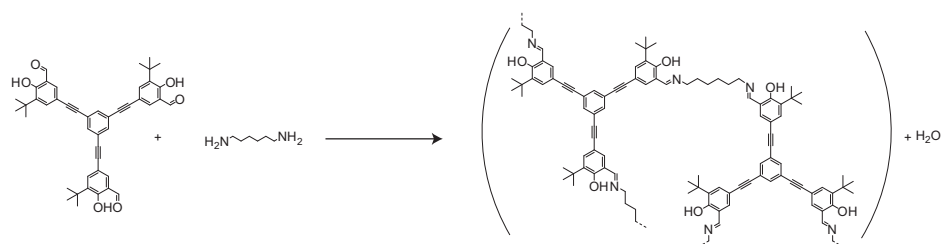


Figure 8.1: Polycondensation between the *threespoke*-molecule and 1,6-diaminohexane.

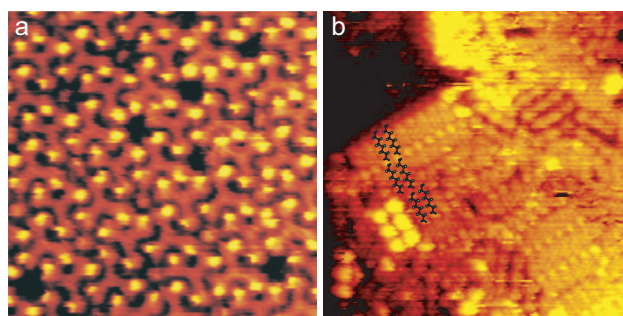


Figure 8.2: The reactants: (a) STM image of the hexagonal phase for the *threespoke*-compound. (b) 1,6-diaminohexanes forming a lamella structure. Molecular models are added to guide the eye. (Image sizes  $120 \times 120 \text{ \AA}^2$ ).

polythiophene wires at the liquid-solid interface by electrochemical epitaxial polymerization [103, 104]. Compared to the previously studied systems, the two-dimensional "gelation" system studied here is more complex as it involves the coupling of two different molecules and allows for extended branching.

### 8.1.2 Model system

The condensation reaction studied is displayed in Fig. 8.1. As reactants we use the large aromatic *threespoke*-molecules and 1,6-diaminohexane. The *threespoke*-compound was chosen in these experiments because it is known to react with octylamines on Au(111) under UHV conditions and contains a molecular geometry which allows for a formation of extended two-dimensional networks. The chain length of the diamines is short enough to exclude interlinks within spokes on the same *threespoke*-molecule, but long enough still to be visible with the STM.

In Fig. 8.2 STM images of the reactants adsorbed onto the Au(111) surface are shown for reminder. As discussed in Chapter 4 the *threespoke*-molecules form four different structures on the Au(111) surface, and are visualized as Y-shaped entities with bright protrusions at the ends, attributed to the t-butyl groups. In the structure shown in



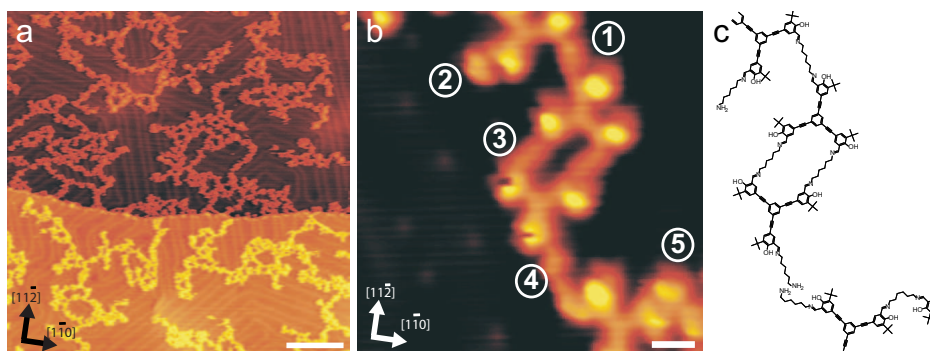


Figure 8.3: On-surface polycondensation: (a) Large-scale STM image (sample voltage  $-1.4$  V, tunnel current  $-0.66$  nA, bar size 20 nm). (b) High-resolution STM image revealing the local bonding pattern. The numbers refer to bonding geometries discussed in the text (sample voltage 1.5 V, tunnel current 0.34 nA, bar size 1 nm). (c) Model of the structure in (b).

Fig. 1a the *threespoke*-compounds form a hexagonal pattern. The 1,6-diaminohexanes form lamella structures on the surface. The lamella structures could only be imaged for sample temperatures below  $\sim 120$  K due to a high diffusivity of the molecules at higher temperatures.

## 8.2 Threespoke-compound and 1,6-diaminohexane

Upon co-deposition of the reactants and annealing above 400 K, open polymeric structures are formed on the surface, as seen on the large-scale STM image in Fig. 8.3a. These polymeric structures are clearly different from the dense-packed structures formed by the reactants (Fig. 8.2). At this annealing temperature we expect that non-reacted amines have desorbed and the herringbone reconstruction of the underlying Au(111) surface is revealed around the polymer.

### 8.2.1 Bonding pattern

From high-resolution STM images (see Fig. 8.3b) the local bonding pattern of the polymer can be analyzed. *Threespoke*-molecules with the characteristic Y-shape, are linked together by alkyl chains, imaged as interlinking rods. All aromatic spokes bear exactly one alkyl chain and the alkyls always extend from the side of the phenyl ring opposite to the bright t-butyl group, as expected for the reaction product. Various structural elements can be identified as seen in Fig. 8.3b. Two spokes belonging to different *threespoke*-compounds can be connected directly with either one alkyl chain (1,5), or with two alkyl chains in a characteristic double bonded motif (3). The alkyl linkers can be straight as in (1,3) or compressed/bent as in (5), leading to a brighter appearance in the STM image which we attribute to a gauche defect. Alkyl chains connected to



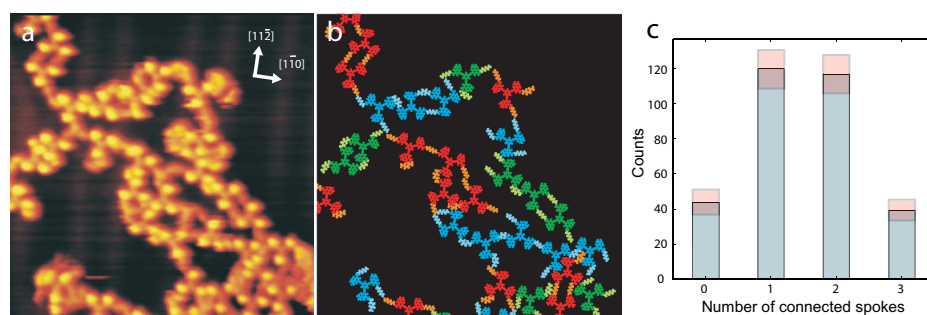


Figure 8.4: Connectivity after preparation A (see text): (a) STM image (size  $210 \times 210 \text{ \AA}^2$ ). (b) Colour-coding of the image in (a) showing individual oligomers in different colours. (c) Histogram with the number of spokes on a *threespoke*-molecule connected directly to a neighboring *threespoke*-molecule by an amine. The light red boxes indicate the uncertainty.

an aromatic spoke at only one end are also observed (2,4). If the unbound end of a single-linked amine meets other single-linked amines they are observed to pair head-to-head (4). This is seen as rod-like features with twice the length of a single diamine. Alkyls that contain an unbound amino end which is not joined to another amino group are mobile at the imaging temperature and imaged as smeared out features (2).

All interlinks between *threespoke*-molecules and amino groups are attributed to covalent imine bonds in agreement with the similar surface born reaction, discussed in Chapter 7. In contrast, we propose that hydrogen bonds are formed at the connection point between two amino groups paired head to head as in (4). (From the studies of octylamine on Au(111), covalent C-N-C bond formation is another option.)

From images as the one in Fig. 2b we conclude that (i) oligomers held together by covalent bonds are formed, (ii) all spokes of the *threespoke*-molecules are saturated with amines, but (iii) some amines have a free end and (iv) the network is thus only partly connected by covalent imine bonds.

## 8.2.2 Connectivity

To investigate if order and connectivity in the polymer can be controlled, the polymer was formed by two different preparation procedures, termed A and B. In both preparation procedures *threespoke*-molecules were dosed onto the Au(111) sample held at room temperature resulting, in a coverage below 0.3 ML as estimated by STM.

In preparation procedure A (Fig. 8.4) the sample with *threespoke*-molecules was cooled to a temperature of 120-160 K. At this temperature the *threespoke*-molecules form large ordered islands. The cold sample was then exposed to a background ( $\sim 1 \times 10^{-7}$  mBar) of 1,6-diaminohexane until multilayers of amines were formed on the surface. Upon annealing to room temperature oligomers embedded in a matrix of amines (monolayer regime) were observed (not shown). A further annealing to 450 K resulted in desorption of unreacted amines.

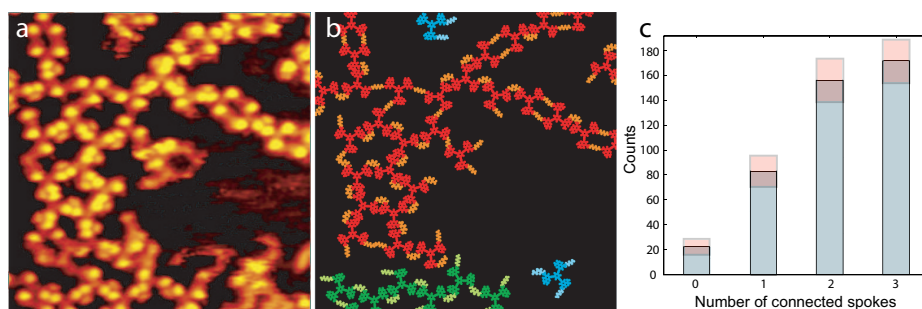


Figure 8.5: Connectivity after preparation B (see text): (a) STM image (size  $210 \times 210 \text{ \AA}^2$ ). (b) Colour-coding of the image in (a) showing individual polymers in different colours. (c) Histogram with the number of spokes on a *threespoke*-molecule connected directly to a neighboring *threespoke*-molecule by an amine. The light red boxes indicate the uncertainty.

In preparation procedure B (Fig. 8.5) the sample containing *threespoke*-molecules was heated to 400 K and exposed to a low pressure ( $5 \times 10^{-9}$  mBar) of diamines for  $\sim 30$  min.

### Comparison

At a first glance the STM images of Fig. 8.4a and 8.5a look similar. However, a careful analysis of the bonding pattern shows otherwise. In Fig. 8.4b (8.5b) models of the molecular structures in Fig. 8.4a (8.5a) are shown. In the models each macromolecule formed from *threespoke*-molecules connected covalently by diamines is colour-coded individually. Preparation procedure A favours the formation of small oligomers (the largest macromolecules found contain 7 *threespoke*-compounds linked with 14 alkyl units) whereas real polymers are formed by preparation procedure B (the largest polymers extend out of the STM images with sub-molecular resolution and contain more than 50 interlinked *threespoke*-molecules).

To characterize the degree of covalent interlinking we investigate the bonding pattern at the sub-molecular scale. In the histograms of Figs. 8.4c and 8.5c the number of *threespoke*-molecules are plotted with either 0, 1, 2 or 3 molecular spokes linked directly (i.e. by a single alkyl chain) to a spoke of a neighboring *threespoke*-molecule. Each histogram is based on a series of STM images obtained in three independent experiments following either preparation A (Fig. 8.4c) or B (Fig. 8.5c). Within statistical uncertainty no differences were observed for experiments with the same preparation.

The network formed by preparation procedure B exhibits a significantly higher degree of interlinkage as expressed by the higher proportion of molecules with 3 connected spokes. From the histograms we can determine a parameter,  $P$ , defined as the average number of spokes on a given *threespoke*-molecule connected directly via only one alkyl chain to a spoke of a neighboring *threespoke*-molecule.  $P$  thus describes the connectivity in the polymer. For preparation procedure A (B) we find  $P = 0.49 \pm 0.03$

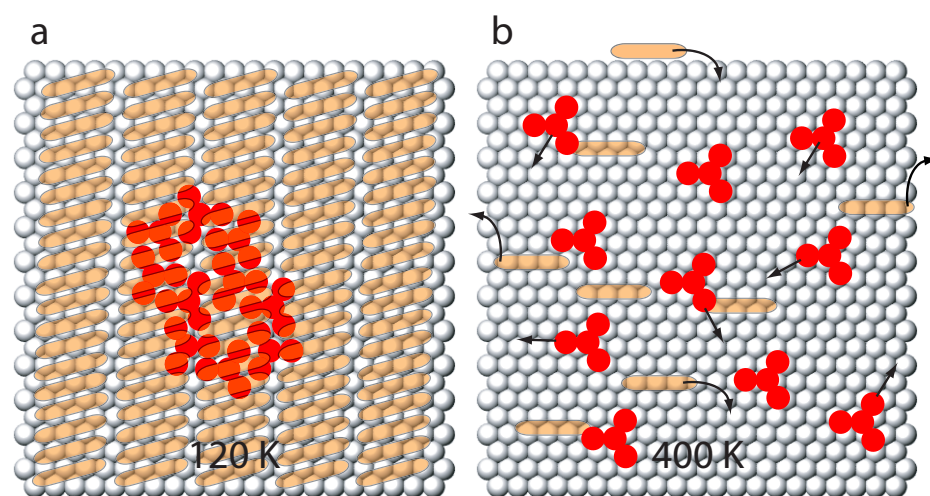


Figure 8.6: Preparation procedures: (a) High flux, low mobility and quenching in preparation A. (b) Low flux, reversibility and mobility in preparation B.

( $P = 0.70 \pm 0.03$ ). Consequently, in preparation A only 1 out of 2 spokes become interlinked, whereas 2 out of 3 spokes are interlinked after preparation B.

### Discussion

The results clearly demonstrate that the growth of the polymer depends on the kinetics and thermodynamics during reaction. In preparation A (see Fig. 8.6a) an extremely high diamine flux during reaction was realized by saturating the condensed *threespoke*-islands with multilayers of diamines and subsequent annealing above the reaction temperature. Furthermore, since reaction will happen at the lowest possible temperature the mobility of the *threespoke*-molecules is expected to be hindered by the island formation. In this kinetic scenario reaction thus happens immediately (when the reaction temperature has been reached) between a close-lying diamine and *threespoke* endgroup which leads to a high chance of saturation with free amino-ends.

On the contrary, in preparation B (see Fig. 8.6b) the sample containing *threespoke*-molecules was heated to 400 K during deposition and reaction with diamines. We expect that free diamines only have a limited lifetime on the Au(111) surface at this temperature which together with the low flux ( $p = 5 \times 10^{-9}$  mBar) of diamines impinging on the surface results in a lower instant amine coverage during reaction. Furthermore, the high temperature implies that the *threespoke*-molecules are free to diffuse and have a high conformational flexibility. The high mobility and conformational freedom in combination with the low flux allows for a gradual build-up of structures, because the chance has increased that two partly saturated *threespoke*-molecules reach each other and interconnect before full saturation. In this case the growth thus happens closer to thermodynamic equilibrium which ensures the observed high degree of connecti-

ty. Furthermore, free amino-groups can undergo a nucleophilic attack to the carbon in already formed imino-groups<sup>2</sup> and thereby release the original imine-bond under the formation of a new imine-bond to the attacking amino-group. The reaction is therefore expected to be partly reversible during this preparation which is expected to enhance the connectivity and order further.

The correlation between the connectivity and the sol-gel transition<sup>3</sup> has achieved high interest in the study of gels [238]. In the simple classical Flory-Stockmayer model which assumes all bonds to be independent and does not account for the possibility of forming e.g. closed loops [251–254], a critical value,  $P_c$ , for the connectivity can be determined, above which infinite interlinked networks are formed. In the model the critical value is  $P_c = 1/(z - 1)$ , where  $z$  is the number of branching arms. In real gels the sol-gel transition is normally found for connectivities close to  $P_c$ . It should be noted that even above the gelation point where infinite polymeric networks can be formed, a large amount of the polymer material is expected to exist as non-infinite polymers or oligomers.

In the polycondensation reactions studied here  $z = 3$  which gives a Flory-Stockmayer limit of  $P_c = 1/2$ . The degree of connectivity in polymer B is thus well above the critical value and the formation of large polymers or even infinite polymeric networks should be achievable. (A decreased mobility of large polymers along with the restriction to two dimensions probably causes limitations in the size of covalently interlinked networks.) In contrast the connectivity in polymer A is at the threshold, and we therefore should only expect a small fraction of larger oligomers on the surface, as observed in the STM images.

### 8.2.3 Ring and chain formation

The high connectivity in polymer B implies that we locally observe areas with either chain or network formation (see Figs. 8.7 and 8.8). The images in Figs. 8.7 and 8.8 are obtained in an imaging mode where the aromatic system of the *threespoke*-molecules is clearly visualized whereas the interlinking alkyls are not observed.

#### Chain and porous domains

In Fig. 8.7 a domain dominated by chain-like polymeric wires is seen. The chain segments are built up of the characteristic double-bonded *threespoke* dimers with straight alkyl chains (recall Fig. 8.3b). The remaining spoke is connected to a free spoke on the adjacent dimer. The alkyl chain interlinking two dimers often contain a gauche defect allowing the two interlinked spokes to be parallel (see also Fig. 8.5). Sometimes one end of a chain reacts with the other end resulting in ring-closure, as seen in the top-left corner of Fig. 8.7a.

In the networks the *threespoke*-molecules constitute branching points with each *threespoke*-molecule connected covalently to three *threespoke* neighbours (Fig. 8.8).

<sup>2</sup>The reaction mechanism is similar to the condensation between aldehydes and amines.

<sup>3</sup>The sol-gel transition is the transition from the liquid sol state consisting of small oligomers to the solid gel state containing macroscopic polymeric networks.

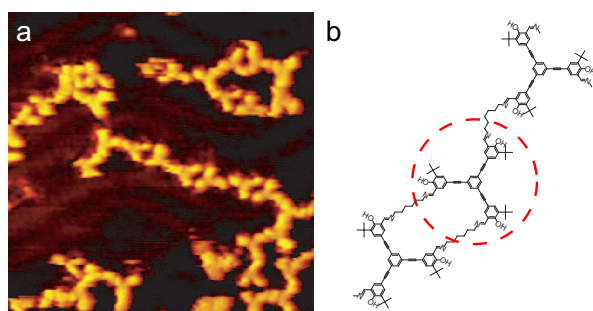


Figure 8.7: Chain domain: (a) STM image (size  $250 \times 250 \text{ \AA}^2$ ). (b) Schematic drawing of a chaining *threespoke*-molecule.

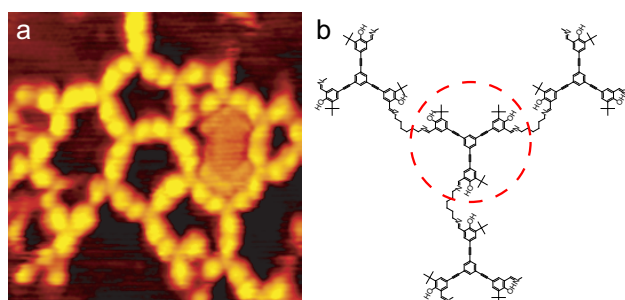


Figure 8.8: Porous network domain: (a) STM image (size  $150 \times 150 \text{ \AA}^2$ ). (b) Schematic drawing of a branching *threespoke*-molecule.

The interlinking alkyl chains mostly contain gauche defects. By repeated interlinkage covalently connected pores result, as seen in Fig. 8.8a.

Areas with a network structure are more abundant than areas with chain formation. This is also reflected in the number of *threespoke*-molecules forming branching points (26%) compared to *threespoke*-compounds acting as non-terminating chain segments (13%). The remaining *threespoke*-molecules (60%) contain at least one non-interlinked spoke and lead thus to disorder or domain termination.

### Pore sizes

In the networks we observe pores of different sizes. In Fig. 8.9 high-resolution images of the most abundant pores are seen with a diameter ranging from approximately 3 nm to 10 nm. In the histogram in Fig. 8.10a the abundance of pores built up of up to eight *threespoke*-molecules is plotted. Molecular ring structures with more members are also observed, but are omitted in the histogram since they occur rarely and often extend out of the STM images. Molecular rings formed by four to six interlinked *threespoke*-molecules are favoured.

We expect the ring-size selection to result from competing kinetic and thermody-



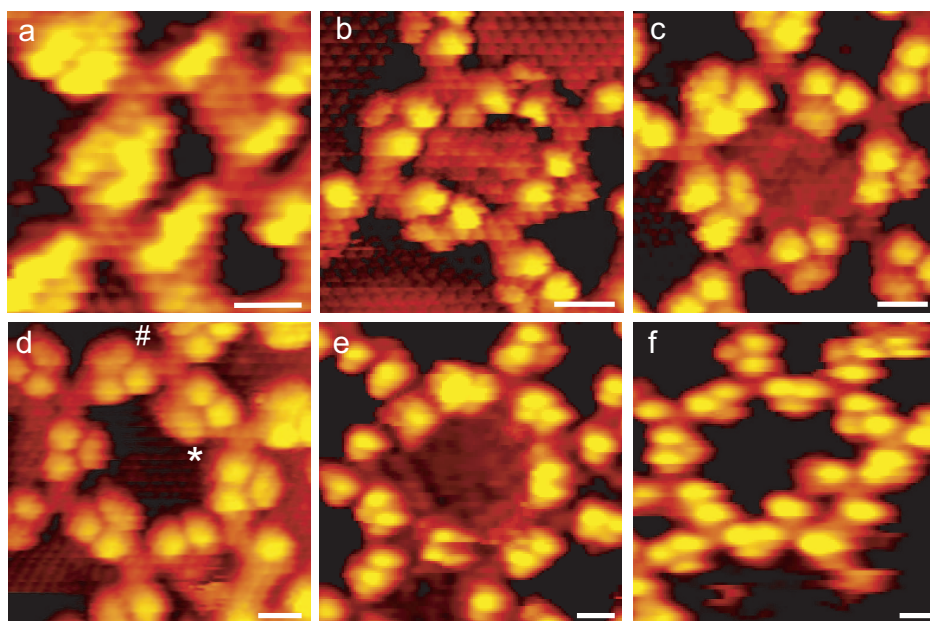


Figure 8.9: Network pore sizes: STM images of (a) three, (b) four, (c) five, (d) six, (e) seven, and (f) eight-membered molecular pores (scale bar 1 nm). The \* (#) on (d) mark alkyl linkers placed inside (outside) the pore.

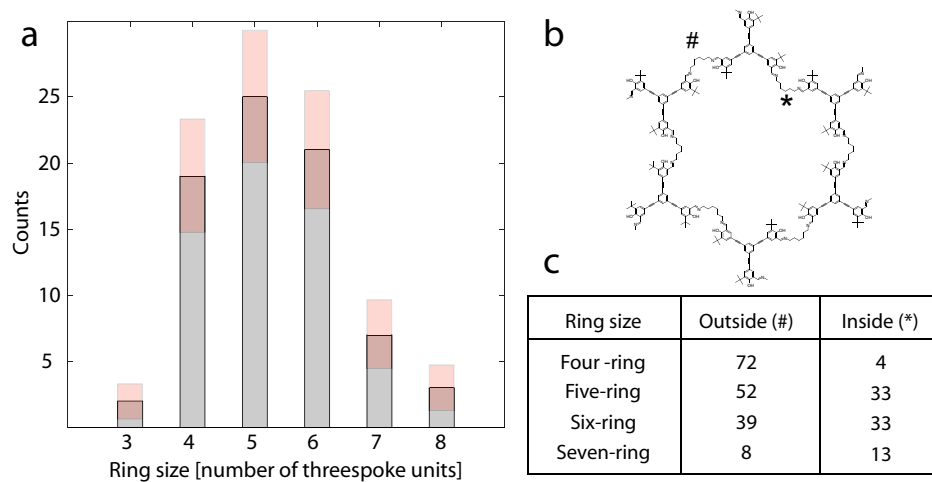


Figure 8.10: Distribution of pore sizes and alkyl chain positions: (a) Histogram with the distribution of ring sizes. (b) Schematic model of the six-membered pore in Fig. 8.9 with the \* (#) marking alkyl chains place inside (outside). (c) Number of interlinking alkyls with a position outside (#) or inside (\*) the pores.

namic factors: (i) the fast process of intramolecular ring-closure compared to the process of adding additional *threespoke*-molecules, (ii) strain reduction by reducing disfavoured bonding angles. Since the polycondensation is reversible in the presence of free diamines, we expect the low abundance of three-membered rings to be caused by a high strain in that configuration which is released upon reopening and addition of more *threespoke* units. (Fig. 8.9a). In contrast, the low abundance of pores containing more than six members is assumed to be disfavoured by ring closure.

Strain is also observed to affect the local bonding pattern of the pores. As pointed out previously the alkyls interlinking *threespoke*-molecules forming branched structures are mostly bent (contain a gauche defect). In Fig. 8.10b a schematic drawing of the 6-membered pore in Fig. 8.9d is drawn. As seen the interlinking alkyls can either be positioned at the inner pore wall (★) or to the outer pore wall (‡), as indicated in Fig. 8.9d and 8.10b. In the table of Fig. 8.10c the distribution of interlinking alkyls placed on the outside (‡) and inside (★) of the pores as a function of pore size is given. In a six-membered pore all pairwise interlinked trialdehyde spokes can be parallel (see. Fig. 8.10b) whereas the internal angle between interlinked spokes must be concave (convex) for the smaller (larger) pores. To realize a concave (convex) angle it is preferable to place the linker on the outside (inside) of the pore since this leads to the least bending in the alkyl chain. Thus four-membered and five-membered pores reduce the strain by placing the alkyls on the outside. This is very pronounced for the four-membered rings where external alkyl chains were only observed at interconnections participating in two neighboring four or five-membered pores. The six-membered pores are nearly free of bending strain and the position is thus arbitrary. For the seven-membered pores there seems (poor statistics) to be a tendency of placing the alkyls on the inside.

In the pores we occasionally observe a trapping of small molecular species (see e.g. Fig. 8.8a and Fig 8.9c,e) which we speculate to be diamines that due to the confinement in the pores have not desorbed.

#### 8.2.4 Conclusion

In conclusion we have formed a two-dimensional polymeric network on the Au(111) surface. By optimizing the reaction conditions extended monomolecular high covalently interlinked networks were formed with connectivities approaching 70%. Such large surface polymers would be difficult to deposit and flatten on the surface by other means. We expect covalently connected polymers as the ones studied here to be severely more thermally and chemically stable than self-assembled networks. We thus foresee covalently bound networks to be more promising candidates for real applications in the field of advanced thin films than self-assembled nanostructures mediated by non-covalent interactions, despite the high focus given to self-assembly in recent years.

Furthermore, we found that the polymeric networks locally exhibit porous domains. Such covalently bound porous networks could due to their high stability be of use in the field of molecular sensors or as stable organic templates for e.g. cell adhesion studies.





## CHAPTER 9

---

### Summary and outlook

---

In this thesis a number of adsorption studies of organic molecules have been presented. The work can be divided into two main topics. The focus of the first part of the thesis was on dynamical processes such as diffusion and conformational changes of adsorbed molecules whereas the second part dealt with organic reactions between adsorbed molecules. The main technique used for the investigations was scanning tunneling microscopy (STM). Beside STM measurements evidence was obtained by spectroscopic measurements and density functional theory calculations.

In Chapter 3 the adsorption and diffusion behaviour of azobenzene on Cu(110) was analyzed. The main finding was that the diffusivity of azobenzene on Cu(110) depends on the specific adsorption site, with molecules in the meta-stable configurations being more diffusive than molecules occupying low-energy sites.

In the thesis special emphasis was laid on the adsorption of a class of oligo-phenylene-ethynylenes with varying geometry of the molecular backbone, discussed in Chapters 4 and 5. On the Au(111) surface the molecules were observed to form large ordered domains. Three of the family members adsorbed flat-lying, whereas the last member unexpectedly obtained an upright-standing configuration. The flat-adsorbing compounds adopted different surface conformations some of which were chiral. For the majority of these adsorption structures, chirality was also expressed in the molecular tiling pattern, and the two levels of chirality displayed a high degree of correlation. The main finding of the study was that the formation and chiral ordering of the self-assembled structures resulted from dynamic interchanges between a diffusing lattice gas and the nucleated islands, as well as from a chiral switching process in which molecules switch their conformation by an intramolecular rotation around a molecular spoke. This enabled them to accommodate to the tiling pattern of the surrounding molecular structures

and thereby reach the state of highest binding energy. Since the energy landscape often favoured chiral molecular conformations, the observed switching caused a degree of chiral amplification in the molecular layers.

The observed accommodation procedure is effective as it reduces the mass transport compared to segregation procedures in which molecules reaching the islands only incorporate if they have the right conformation. In future studies the formation of global homochiral domains may be realized by seeding the surface with chiral template compounds or by adsorbing the molecules on a chiral template surface. At present such chiral seeding compounds are under synthesis in the organic synthesis group of Assoc. Prof. Kurt V. Gothelf. The potential ability to form such homochiral surface layers is of high interest to the field of heterogeneous asymmetric catalysis and even with respect to the understanding of the chiral asymmetry observed in nature. Since oligo-phenylene-ethynylenes are conducting molecules, I expect the compound with an upright-standing adsorption configuration to be an excellent candidate for future single molecule conduction measurements.

In Chapter 6 the adsorption of aliphatic amines on Au(111) was investigated. It was found that octylamines undergo a chemical change to trioctylamine upon thermal activation. I hope that future density functional theory calculations will shed light on this unexpected surface born reaction.

In Chapters 7 and 8 covalent reaction was applied to interlink co-adsorbed aldehydes and amines in the submonolayer regime on the Au(111) surface. In Chapter 7 covalent interlinking of the reactants was confirmed by comparing the sub-molecular STM signature and the NEXAFS characteristics of monomeric reaction products formed *in-situ* and *ex-situ*. A solvent-free reaction path accounting for the observed imineformation was proposed based on ab-initio density functional theory calculations. Furthermore, it was found that the reaction outcome could depend on the preparation procedure, and that conformational order in the structures could be enhanced if the reactants were pre-assembled prior to reaction. In Chapter 8 highly interconnected polymeric networks were formed. By STM the local bonding pattern was investigated, with focus on connectivity, branching points, and ring or chain formation. We found that the connectivity of the polymeric network could be manipulated by controlling the kinetics during the preparation procedure, and that polymers with a high connectivity contained domains with chain or pore formations. The size distribution of the formed pores was correlated with molecular geometry and strain.

The covalently bound molecular networks investigated clearly lacked long-range order. In my view, the synthesis of covalently connected self-organized surface structures with a high structural order is a great future challenge in the field of bottom-up surface architectures. To realize the goal one can attempt different approaches. (i) The use of more rigid reactants should reduce the number of possible bonding patterns and thereby result in an increased order. Some conformational flexibility might however be required in order not to hinder reaction. (ii) Longer reaction times and higher temperatures might allow for an increased reversibility during reaction, and thereby result in the growth of more thermodynamic structures. (iii) A different attempt could rely on a combination of supramolecular and covalent chemistry. If well-ordered structures mediated by non-covalent interactions are pre-assembled and subsequently interlinked by covalent bonds,

ordered polymeric networks are foreseen. In solution such attempts have been applied to form desired macromolecules by a combination of metal complexation and covalent imineformation [232]. The high order observed in Chapter 7 when the monomeric reaction products were preassembled before reaction suggest that this procedure can be transferred directly to chemistry on surfaces.



## CHAPTER 10

---

### Dansk resumé

---

Nanoteknologi er den videnskabelige disciplin, der beskæftiger sig med fysiske, kemiske og biologiske processer på atomernes og molekylernes længdeskala (0.1-100nm). Det ultimative mål indenfor nanoteknologien er at undersøge, kontrollere og udvikle nye nanomaterialer og komponenter, som kan anvendes i den fremtidige teknologiske udvikling.

Denne afhandling er opdelt i to hovedområder. I den første del udforskes selvsamlede strukturer, der dannes, når et enkelt lag af molekyler deponeres på en metaloverflade. En selvsamlet struktur skabes, når molekyler påvirker hinanden med ikke-kovalente kræfter (f.eks. hydrogen bindinger eller Van der Waals vekselvirkninger) og derved spontant samler sig i en velordnet struktur. Den teknik, der primært anvendes til studierne, er skannetunnel mikroskopi (STM), som gør det muligt at afbilde molekyler med submolekylær opløsning. I figur 10.1 ses STM afbildningen af tre organiske molekyler med hhv. lineær, v-formet og trebenet geometri, der alle danner ordnede selvsamlede netværk efter deponering på en guldoverflade.

Hvis man vil forstå og med tiden kontrollere de strukturer, der dannes ved selvsamling, er det vigtigt at opnå en højere forståelse for molekylernes indbyrdes vekselvirkning. I denne afhandling er fire molekyler med ens kemisk sammensætning, men forskellig geometri blevet undersøgt. Tre af de geometriske varianter satte sig på overfladen (adsorberede) i en fladtliggende adsorptionsgeometri for at opnå størst mulig vekselvirkning mellem det molekylære skelet og metaloverfladen (figur 10.1). Dette ses normalt for store organiske molekyler. En enkelt variant antog i modsætning en opretstående konfiguration. Dette skyldes stærke vekselvirkninger internt i molekylet.

I opbygningen af molekylære netværk spiller molekylernes dynamiske egenskaber en stor rolle. Et af afhandlingens hovedresultater er, at molekylerne i figur 10.1 kan

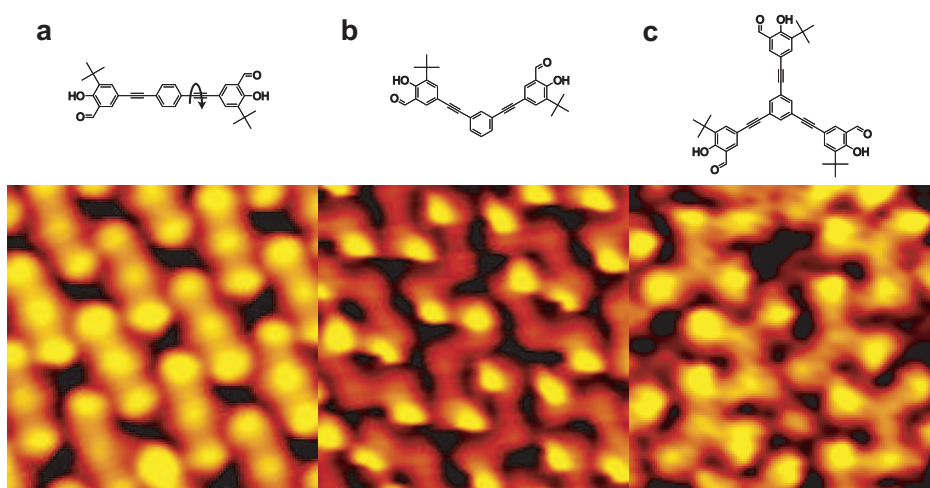


Figure 10.1: STM billeder af tre molekyler med hhv. (a) lineær (b) v-formet og (c) trebenet geometri.

ændre deres molekyllære geometri efter adsorption ved at udføre en rotation omkring en molekyllær arm. Dette er markeret med en pil i figuren. Pga. den stærke vekselvirkning mellem det molekyllære skelet og metaloverfladen har man hidtil troet, at sådanne konformationelle ændringer var umulige. Denne nye erkendelse har åbnet op for en helt ny forståelse for, hvorfor nogle molekyler effektivt samles i ordnede strukturer, hvor alle molekylerne har ens konfiguration.

Da molekyllær selvsamling er baseret på ikke-kovalente bindinger mellem de molekyllære byggesten, er de strukturer, der dannes ofte relativt ustabile og opløses f.eks. ved opvarmning. Denne ustabilitet kan reduceres, hvis de molekyllære netværk kædes sammen med rigtige kemiske, kovalente bindinger i stedet for de svagere ikke-kovalente bindinger. En kemiker vil kalde dette polymerisering. I modsætning til selvsamling er dannelsen af polymere netværk i to dimensioner kun studeret i et meget begrænset omfang.

I anden halvdel af afhandlingen studeres kemiske reaktioner mellem organiske molekyler, som deponeres sammen. Først vises det, at det er muligt at koble et molekyle med en amingruppe sammen med et molekyle med en aldehydgruppe efter deponering på en guldoverflade under ultrahøjt vakuum. Denne reaktion kaldes på fagsprog imindannelse. At reaktionen forløber vises ved at sammenligne reaktionsprodukter, der dannes ved reaktion på overfladen i vakuumkammeret, med de samme produkter syntetiseret ved normal organisk syntese i et kemilaboratorium.

Dernæst tages skridtet helt ud, og en rent to-dimensionel polymer dannet direkte på guldoverfladen demonstreres. På figur 10.2 ses STM billeder af en sådan polymer dannet ved reaktion af det trebenede molekyle i figur 10.1c og en diamin. Fra storskala billedet i figur 10.2a ses det tydeligt, at polymeren er spredt ud over overfladen. Med højtopløst STM undersøges polymeren lokalt og bindingsmønstre helt ned til det enkelte

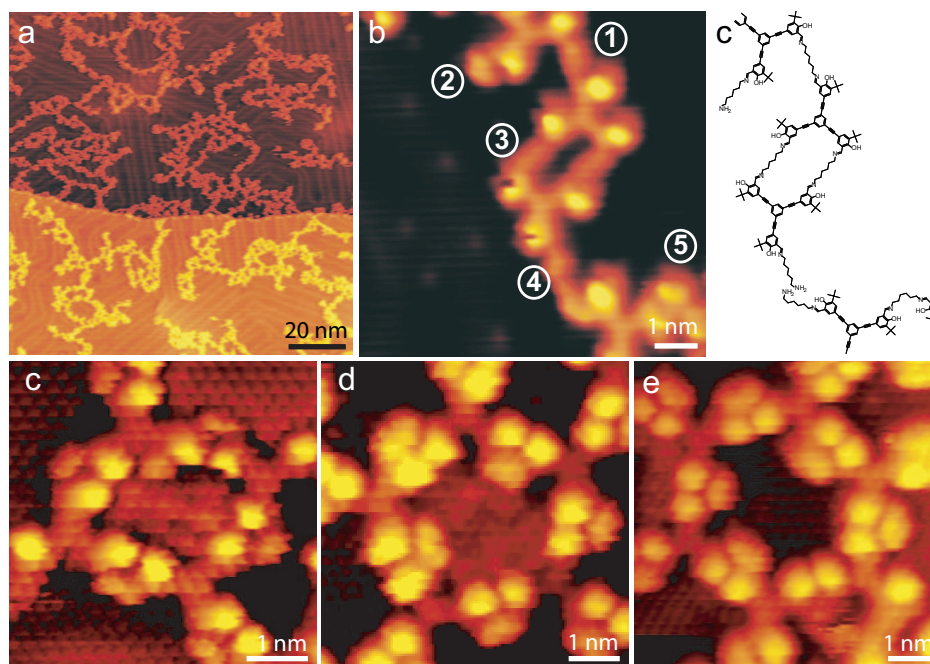


Figure 10.2: STM billeder af en to-dimensionel polymer på en guldoverflade. (a) Storskala billede, hvor det ses, at polymeren er spredt ud over overfladen. (b) Højt-opløst billede af polymeren, der viser forskellige bindingsmønstre. (c-e) Molekylære ringe observeret lokalt i polymeren.

led studeres (se figur 10.2b). Numrene på figuren markerer forskellige bindingsmotiver. Endelig vises det, at forskellige preparationsmetoder fører til polymerer med varierende grad af sammenhæng, og at polymerer med en høj grad af sammenhæng lokalt indeholder områder bestående af kovalent forbundne porer. Eksempler på sådanne porer opbygget af hhv. fire, fem eller seks sammenkædede trebenede molekyler er vist i figur 10.2c-e. Tilsvarende studier af lokale strukturer i polymerer syntetiseret i væskefasen er ikke mulige, da man til det formål kun har analysemetoder, der giver information om det gennemsnitlige bindingsmønster.





---

## Bibliography

---

- [1] G. Binnig, H. Rohrer, C. Gerber and E. Weibel. *7x7 Reconstruction on Si(111) Resolved in Real Space*. Physical Review Letters, **50**(2):120–123, 1983.
- [2] M. F. Crommie, C. P. Lutz and D. M. Eigler. *Imaging Standing Waves in a 2-Dimensional Electron-Gas*. Nature, **363**(6429):524–527, 1993.
- [3] B. Q. Xu and N. J. J. Tao. *Measurement of single-molecule resistance by repeated formation of molecular junctions*. Science, **301**(5637):1221–1223, 2003.
- [4] E. Ganz, S. K. Theiss, I. S. Hwang and J. Golovchenko. *Direct Measurement of Diffusion by Hot Tunneling Microscopy - Activation-Energy, Anisotropy, and Long Jumps*. Physical Review Letters, **68**(10):1567–1570, 1992.
- [5] R. J. Driscoll, M. G. Youngquist and J. D. Baldeschwieler. *Atomic-Scale Imaging of DNA Using Scanning Tunneling Microscopy*. Nature, **346**(6281):294–296, 1990.
- [6] S. W. Hla, L. Bartels, G. Meyer and K. H. Rieder. *Inducing all steps of a chemical reaction with the scanning tunneling microscope tip: Towards single molecule engineering*. Physical Review Letters, **85**(13):2777–2780, 2000.
- [7] G. Whitesides and B. Grzybowski. *Self-Assembly at All Scales*. Science, **295**:2418–2421, 2002.
- [8] G. M. Whitesides, J. P. Mathias and C. T. Seto. *Molecular Self-Assembly and Nanochemistry - a Chemical Strategy for the Synthesis of Nanostructures*. Science, **254**(5036):1312–1319, 1991.
- [9] J. A. Theobald, N. S. Oxtoby, M. A. Phillips, N. R. Champness and P. H. Beton. *Controlling molecular deposition and layer structure with supramolecular surface assemblies*. Nature, **424**:1029–1031, 2003.
- [10] T. Yokoyama, S. Yokoyama, T. Kamikado, Y. Okuno and S. Mashiko. *Selective assembly on a surface of supramolecular aggregates with controlled size and shape*. Nature, **413**:619–621, 2001.
- [11] J. Weckesser, A. D. Vita, J. V. Barth, C. Cai and K. Kern. *Mesoscopic Correlation of Supramolecular Chirality in One-Dimensional Hydrogen-Bonded Assemblies*. Physical Review Letters, **87**(9):096101, 2001.
- [12] A. Kühnle, T. R. Linderoth, B. Hammer and F. Besenbacher. *Chiral recognition in dimerization of adsorbed cysteine observed by scanning tunnelling microscopy*. Nature, **415**:891–893, 2002.
- [13] R. Fasel, M. Parschau and K. H. Ernst. *Amplification of chirality in two-dimensional enantiomorphous lattices*. Nature, **439**(7075):449–452, 2006.
- [14] P. S. Peercy. *The drive to miniaturization*. Nature, **406**(6799):1023–1026, 2000.
- [15] T. Ito and S. Okazaki. *Pushing the limits of lithography*. Nature, **406**(6799):1027–1031, 2000.
- [16] J. V. Barth, G. Costantini and K. Kern. *Engineering atomic and molecular nanostructures at surfaces*. Nature, **437**(7059):671–679, 2005.
- [17] P. B. Messersmith and M. Textor. *Nanomaterials - Enzymes on nanotubes thwart fouling*. Nature Nanotechnology, **2**(3):138–139, 2007.

- [18] F. Davis and S. P. J. Higson. *Structured thin films as functional components within biosensors*. Biosensors and Bioelectronics, **21**(1):1–20, 2005.
- [19] C. J. Baddeley. *Fundamental investigations of enantioselective heterogeneous catalysis*. Topics in Catalysis, **25**(1-4):17–28, 2003.
- [20] C. D. Pentecost, K. S. Chichak, A. J. Peters, G. W. V. Cave, S. J. Cantrill and J. F. Stoddart. *A molecular Solomon link*. Angewandte Chemie-International Edition, **46**(1-2):218–222, 2007.
- [21] J. A. Miwa, S. Weigelt, H. Gersen, F. Besenbacher, F. Rosei and T. R. Linderöth. *Azobenzene on Cu(110): Adsorption Site-Dependent Diffusion*. Journal of the American Chemical Society, **128**(10):3164–3165, 2006.
- [22] C. Busse, S. Weigelt, L. Petersen, E. Lægsgaard, F. Besenbacher, T. R. Linderöth, A. H. Thomsen, M. Nielsen and K. V. Gothelf. *Chiral ordering and conformational dynamics for a class of oligo-phenylene-ethynylenes on Au(111)*. Journal of Physical Chemistry B, **111**(21):5850–5860, 2007.
- [23] S. Weigelt, C. Busse, L. Petersen, E. Rauls, B. Hammer, K. V. Gothelf, F. Besenbacher and T. R. Linderöth. *Chiral switching by spontaneous conformational change in adsorbed organic molecules*. Nature Materials, **5**(2):112–117, 2006.
- [24] S. Weigelt, C. Busse, M. Nielsen, K. V. Gothelf, F. Besenbacher and T. R. Linderöth. *Influence of Molecular Geometry on Adsorption Orientation for Oligo-phenylene-ethynylenes on Au(111)*. Submitted.
- [25] S. De Feyter and F. C. De Schryver. *Two-dimensional supramolecular self-assembly probed by scanning tunneling microscopy*. Chemical Society Reviews, **32**(3):139–150, 2003.
- [26] F. Rosei, M. Schunack, Y. Naitoh, P. Jiang, A. Gourdon, E. Lægsgaard, I. Stensgaard, C. Joachim and F. Besenbacher. *Properties of large organic molecules on metal surfaces*. Progress in Surface Science, **71**(5-8):95–146, 2003.
- [27] S. Barlow and R. Raval. *Complex organic molecules at metal surfaces: bonding, organisation and chirality*. Surface Science Reports, **50**:201–341, 2003.
- [28] J. Weckesser, J. V. Barth, C. Z. Cai, B. Muller and K. Kern. *Binding and ordering of large organic molecules on an anisotropic metal surface: PVBA on Pd(110)*. Surface Science, **431**(1-3):168–173, 1999.
- [29] J. V. Barth, J. Weckesser, C. Z. Cai, P. Günter, L. Bürgi, O. Jeandupeux and K. Kern. *Building supramolecular nanostructures at surfaces by hydrogen bonding*. Angewandte Chemie-International Edition, **39**(7):1230–1234, 2000.
- [30] J. I. Pascual, J. V. Barth, G. Ceballos, G. Trimarchi, A. De Vita, K. Kern and H. P. Rust. *Mesoscopic chiral reshaping of the Ag(110) surface induced by the organic molecule PVBA*. Journal of Chemical Physics, **120**(24):11367–11370, 2004.
- [31] G. E. Poirier and E. D. Pylant. *The self-assembly mechanism of alkanethiols on Au(111)*. Science, **272**(5265):1145–1148, 1996.
- [32] A. A. Dhirani, R. W. Zehner, R. P. Hsung, P. Guyot-Sionnest and L. R. Sita. *Self-assembly of conjugated molecular rods: A high-resolution STM study*. Journal of the American Chemical Society, **118**(13):3319–3320, 1996.
- [33] D. B. Dougherty, J. Lee and J. T. Yates. *Role of conformation in the electronic properties of chemisorbed pyridine on Cu(110): An STM/STS study*. Journal of Physical Chemistry B, **110**(24):11991–11996, 2006.
- [34] A. Dmitriev, N. Lin, J. Weckesser, J. V. Barth and K. Kern. *Supramolecular assemblies of trimesic acid on a Cu(100) surface*. Journal of Physical Chemistry B, **106**(27):6907–6912, 2002.
- [35] Q. Chen and N. Richardson. *Enantiomeric interactions between nucleic acid bases and amino acids on solid surfaces*. Nature Materials, **2**:324–328, 2003.
- [36] M. Stöhr, M. Wahl, C. H. Galka, T. Riehm, T. A. Jung and L. H. Gade. *Controlling molecular assembly in two dimensions: The concentration dependence of thermally induced 2D aggregation of molecules on a metal surface*. Angewandte Chemie-International Edition, **44**(45):7394–7398, 2005.

- [37] G. Pawin, K. L. Wong, K. Y. Kwon and L. Bartels. *A homomolecular porous network at a Cu(111) surface*. Science, **313**(5789):961–962, 2006.
- [38] R. Otero, M. Schock, L. M. Molina, E. Lægsgaard, I. Stensgaard, B. Hammer and F. Besenbacher. *Guanine quartet networks stabilized by cooperative hydrogen bonds*. Angewandte Chemie-International Edition, **44**(15):2270–2275, 2005.
- [39] J. Ma, B. L. Rogers, M. J. Humphry, D. J. Ring, G. Goretzki, N. R. Champness and P. H. Beton. *Dianhydride-amine hydrogen bonded perylene tetracarboxylic dianhydride and tetraaminobenzene rows*. Journal of Physical Chemistry B, **110**(25):12207–12210, 2006.
- [40] W. Mamdough, M. D. Dong, S. L. Xu, E. Rauls and F. Besenbacher. *Supramolecular nanopatterns self-assembled by adenine-hymine quartets at the liquid/solid interface*. Journal of the American Chemical Society, **128**(40):13305–13311, 2006.
- [41] M. Schock, R. Otero, S. Stojkovic, F. Hummelink, A. Gourdon, E. Lægsgaard, I. Stensgaard, C. Joachim and F. Besenbacher. *Chiral close-packing of achiral star-shaped molecules on solid surfaces*. Journal of Physical Chemistry B, **110**(26):12835–12838, 2006.
- [42] M. de Wild, S. Berner, H. Suzuki, H. Yanagi, D. Schlettwein, S. Ivan, A. Barattoff, H. J. Guentherodt and T. A. Jung. *A novel route to molecular self-assembly: Self-intermixed monolayer phases*. Chemphyschem, **3**(10):881–885, 2002.
- [43] A. Marchenko, Z. X. Xie, J. Cousty and L. P. Van. *Structures of self-assembled monolayer of alkanes adsorbed on Au(111) surfaces*. Surface and Interface Analysis, **30**(1):167–169, 2000.
- [44] L. Gross, F. Moresco, P. Ruffieux, A. Gourdon, C. Joachim and K. H. Rieder. *Tailoring molecular self-organization by chemical synthesis: Hexaphenylbenzene, hexa-peri-hexabenzocoronene, and derivatives on Cu(111)*. Physical Review B, **71**(16), 2005. 165428.
- [45] J. C. Swarbrick, J. Ma, J. A. Theobald, N. S. Oxtoby, J. N. O'Shea, N. R. Champness and P. H. Beton. *Square, hexagonal, and row phases of PTCDA and PTCDI on Ag/Si(111) –  $\sqrt{3} \times \sqrt{3}R30^\circ$* . Journal of Physical Chemistry B, **109**(24):12167–12174, 2005.
- [46] A. Dmitriev, H. Spillmann, N. Lin, J. V. Barth and K. Kern. *Modular assembly of two-dimensional metal-organic coordination networks at a metal surface*. Angewandte Chemie-International Edition, **42**(23):2670–2673, 2003.
- [47] T. Classen, G. Fratesi, G. Costantini, S. Fabris, F. L. Stadler, C. Kim, S. de Gironcoli, S. Baroni and K. Kern. *Templated growth of metal-organic coordination chains at surfaces*. Angewandte Chemie-International Edition, **44**(38):6142–6145, 2005.
- [48] S. Stepanow, N. Lin, D. Payer, U. Schlickum, F. Klappenberger, G. Zoppellaro, M. Ruben, H. Brune, J. V. Barth and K. Kern. *Surface-assisted assembly of 2D metal-organic networks that exhibit unusual threefold coordination symmetry*. Angewandte Chemie-International Edition, **46**(5):710–713, 2007.
- [49] N. Lin, A. Dmitriev, J. Weckesser, J. V. Barth and K. Kern. *Real-Time Single-Molecule Imaging of the Formation and Dynamics of Coordination Compounds*. Angewandte Chemie - International Edition, **41**(24):4779–4783, 2002.
- [50] A. Dally. *Thalidomide: was the tragedy preventable?* Lancet, **351**(9110):1197–1199, 1998.
- [51] V. Humblot, S. Haq, C. Muryn and R. Raval. *(R,R)-tartaric acid on Ni(110): the dynamic nature of chiral adsorption motifs*. Journal of Catalysis, **228**(1):130–140, 2004.
- [52] J. M. Bonello, F. J. Williams and R. M. Lambert. *Aspects of enantioselective heterogeneous catalysis: structure and reactivity of (S)-(-)-1-(1-naphthyl)ethylamine on Pt(111)*. Journal of the American Chemical Society, **125**(9):2723–2729, 2003.
- [53] K. H. Ernst. *Supramolecular surface chirality*. Topics in Current Chemistry, **265**:209–252, 2006.
- [54] C. F. McFadden, P. S. Cremer and A. J. Gellman. *Adsorption of Chiral Alcohols on “Chiral” Metal Surfaces*. Langmuir, **12**:2483–2487, 1996.
- [55] G. Lopinski, D. Moffatt, D. Wayner and R. Wolkow. *Determination of the absolute chirality of individual adsorbed molecules using the scanning tunneling microscope*. Nature, **392**:909–911, 1998.
- [56] H. Fang, L. C. Giancarlo and G. W. Flynn. *Direct Determination of the Chirality of Organic Molecules by Scanning Tunneling Microscopy*. Journal of Physical Chemistry B, **102**:7311–7315, 1998.

- [57] A. Schiffrin, A. Riemann, W. Auwarter, Y. Pennec, A. Weber-Bargioni, D. Cvetko, A. Cossaro, M. Al-berto and J. V. Barth. *Zwitterionic self-assembly of L-methionine nanogratings on the Ag(111) surface*. Proceedings of the National Academy of Sciences of the United States of America, **104**(13):5279–5284, 2007.
- [58] S. M. Barlow, S. Louafi, D. Le Roux, J. Williams, C. Muryn, S. Haq and R. Raval. *Supramolecular assembly of strongly chemisorbed size-and shape-defined chiral clusters: S- and R-alanine on Cu(110)*. Langmuir, **20**(17):7171–7176, 2004.
- [59] M. O. Lorenzo, C. J. Baddeley, C. Muryn and R. Raval. *Extended surface chirality from supramolecular assemblies of adsorbed chiral molecules*. Nature, **404**:376–379, 2000.
- [60] A. M. Lakhani, D. J. DeWitt, N. M. Sant’Agata and T. P. Pearl. *Persistence of chirality for a weakly bound adsorbate: (R,R)- and (S,S)-tartaric acid/Ag(111)*. Journal of Physical Chemistry C, **111**(15):5750–5755, 2007.
- [61] M. Parschau, S. Römer and K. H. Ernst. *Induction of homochirality in achiral enantiomorphous monolayers*. Journal of the American Chemical Society, **126**(47):15398–15399, 2004.
- [62] M. C. Blum, E. Cavar, M. Pivetta, F. Patthey and W. D. Schneider. *Conservation of chirality in a hierarchical supramolecular self-assembled structure with pentagonal symmetry*. Angewandte Chemie-International Edition, **44**(33):5334–5337, 2005.
- [63] F. Charra and J. Cousty. *Surface-induced chirality in a self-assembled monolayer of discotic liquid crystal*. Physical Review Letters, **80**(8):1682–1685, 1998.
- [64] X. H. Qiu, C. Wang, Q. D. Zeng, B. Xu, S. X. Yin, H. N. Wang, S. D. Xu and C. L. Bai. *Alkane-assisted adsorption and assembly of phthalocyanines and porphyrins*. Journal of the American Chemical Society, **122**(23):5550–5556, 2000.
- [65] M. Böhrringer, K. Morgenstern, W. D. Schneider and R. Berndt. *Separation of a racemic mixture of two-dimensional molecular clusters by scanning tunneling microscopy*. Angewandte Chemie-International Edition, **38**(6):821–823, 1999.
- [66] M. Böhrringer, W.-D. Schneider and R. Berndt. *Real Space Observation of a Chiral Phase Transition in a Two-Dimensional Organic Layer*. Angewandte Chemie - International Edition, **39**:792–795, 2000.
- [67] J. M. Bonello, F. J. Williams, A. K. Santra and R. M. Lambert. *Fundamental aspects of enantioselective heterogeneous catalysis: the surface chemistry of methyl pyruvate on Pt(111)*. Journal of Physical Chemistry B, **104**(41):9696–9703, 2000.
- [68] C. B. France and B. A. Parkinson. *Naphtho[2,3-a]pyrene forms chiral domains on Au(111)*. Journal of the American Chemical Society, **125**(42):12712–12713, 2003.
- [69] A. Kühnle, T. R. Linderoth and F. Besenbacher. *Enantiospecific adsorption of cysteine at chiral kink sites on Au(110)-(1 × 2)*. Journal of the American Chemical Society, **128**(4):1076–1077, 2006.
- [70] R. Fasel, M. Parschau and K.-H. Ernst. *Chirality Transfer from Single Molecules into Self-Assembled Monolayers*. Angewandte Chemie - International Edition, **42**:5177–5181, 2003.
- [71] F. Vidal, E. Delvigne, S. Stepanow, N. Lin, J. V. Barth and K. Kern. *Chiral phase transition in two-dimensional supramolecular assemblies of prochiral molecules*. Journal of the American Chemical Society, **127**(28):10101–10106, 2005.
- [72] S. Stepanow, N. Lin, F. Vidal, A. Landa, M. Ruben, J. V. Barth and K. Kern. *Programming supramolecular assembly and chirality in two-dimensional dicarboxylate networks on a Cu(100) surface*. Nano Letters, **5**(5):901–904, 2005.
- [73] M. Böhrringer, K. Morgenstern, W. D. Schneider, R. Berndt, F. Mauri, A. De Vita and R. Car. *Two-dimensional self-assembly of supramolecular clusters and chains*. Physical Review Letters, **83**(2):324–327, 1999.
- [74] A. Kühnle, T. R. Linderoth and F. Besenbacher. *Self-assembly of monodispersed, chiral nanoclusters of cysteine on the Au(110)-(1 × 2) surface*. Journal of the American Chemical Society, **125**(48):14680–14681, 2003.

- [75] S. De Feyter, A. Gesquiere, K. Wurst, D. B. Amabilino, J. Veciana and F. C. De Schryver. *Homo- and heterochiral supramolecular tapes from achiral, enantiopure, and racemic promesogenic formamides: Expression of molecular chirality in two and three dimensions*. *Angewandte Chemie-International Edition*, **40**(17):3217, 2001.
- [76] T. Huang, Z. P. Hu, A. D. Zhao, H. Q. Wang, B. Wang, J. L. Yang and J. G. Hou. *Quasi chiral phase separation in a two-dimensional orientationally disordered system: 6-nitrospiropyran on Au(111)*. *Journal of the American Chemical Society*, **129**(13):3857–3862, 2007.
- [77] N. Richardson. *Two-dimensional crystals: Through the looking glass*. *Nature Materials*, **5**(2):91–92, 2006.
- [78] A. P. Cote, A. I. Benin, N. W. Ockwig, M. O’Keeffe, A. J. Matzger and O. M. Yaghi. *Porous, crystalline, covalent organic frameworks*. *Science*, **310**(5751):1166–1170, 2005.
- [79] O. Endo, H. Ootsubo, N. Toda, M. Suhara, H. Ozaki and Y. Mazaki. *Phase transition of a single sheet of sashlike polydiacetylene atomic sash on a solid surface*. *Journal of the American Chemical Society*, **126**(32):9894–9895, 2004.
- [80] G. S. McCarty and P. S. Weiss. *Formation and manipulation of protopolymer chains*. *Journal of the American Chemical Society*, **126**(51):16772–16776, 2004.
- [81] J. R. Salem, F. O. Sequeda, J. Duran, W. Y. Lee and R. M. Yang. *Solventless Polyimide Films by Vapor-Deposition*. *Journal of Vacuum Science and Technology a-Vacuum Surfaces and Films*, **4**(3):369–374, 1986. Part 1.
- [82] S. F. Alvarado, W. Riess, M. Jandke and P. Stroehriegel. *STM investigation of vapor-deposition polymerization*. *Organic Electronics*, **2**(2):75–82, 2001.
- [83] S. Haq and N. V. Richardson. *Organic beam epitaxy using controlled PMDA-ODA coupling reactions on Cu110*. *Journal of Physical Chemistry B*, **103**(25):5256–5265, 1999.
- [84] C. Neuber, M. Bate, R. Giesa and H. W. Schmidt. *Combinatorial methods for the optimization of the vapor deposition of polyimide monomers and their polymerization*. *Journal of Materials Chemistry*, **16**(34):3466–3477, 2006.
- [85] J. M. Bonello, R. M. Lambert, N. Kunzle and A. Baiker. *Platinum-catalyzed enantioselective hydrogenation of alpha-ketoesters: An unprecedented surface reaction of methyl pyruvate*. *Journal of the American Chemical Society*, **122**(40):9864–9865, 2000.
- [86] B. C. Stipe, M. A. Rezaei, W. Ho, S. Gao, M. Persson and B. I. Lundqvist. *Single-molecule dissociation by tunneling electrons*. *Physical Review Letters*, **78**(23):4410–4413, 1997.
- [87] P. A. Sloan and R. E. Palmer. *Two-electron dissociation of single molecules by atomic manipulation at room temperature*. *Nature*, **434**(7031):367–371, 2005.
- [88] J. R. Hahn and W. Ho. *Oxidation of a single carbon monoxide molecule manipulated and induced with a scanning tunneling microscope*. *Physical Review Letters*, **87**16(16), 2001. 166102.
- [89] M. Ohara, Y. Kim and M. Kawai. *Controlling the reaction and motion of a single molecule by vibrational excitation*. *Chemical Physics Letters*, **426**(4-6):357–360, 2006.
- [90] S. D. Feyter and F. C. D. Schryver. *Two-dimensional supramolecular self-assembly probed by scanning tunneling microscopy*. *Chemical Society Reviews*, **32**(3):139–150, 2003.
- [91] P. C. M. Grim, S. De Feyter, A. Gesquiere, P. Vanoppen, M. Rucker, S. Valiyaveetil, G. Moessner, K. Mullen and F. C. De Schryver. *Submolecularly resolved polymerization of diacetylene molecules on the graphite surface observed with scanning tunneling microscopy*. *Angewandte Chemie-International Edition*, **36**(23):2601–2603, 1997.
- [92] A. Miura, S. De Feyter, M. M. S. Abdel-Mottaleb, A. Gesquiere, P. C. M. Grim, G. Mössner, M. Sieffert, M. Klapper, K. Mullen and F. C. De Schryver. *Light- and STM-tip-induced formation of one-dimensional and two-dimensional organic nanostructures*. *Langmuir*, **19**(16):6474–6482, 2003.
- [93] O. Endo, N. Toda, H. Ozaki and Y. Mazaki. *Domain structure of 17,19-hexatriacontadiyne monolayers formed on graphite (0001) surfaces studied by UHV-STM*. *Surface Science*, **545**(1-2):41–46, 2003.
- [94] Y. Okawa and M. Aono. *Materials science - Nanoscale control of chain polymerization*. *Nature*, **409**(6821):683–684, 2001.

- [95] Y. Okawa and M. Aono. *Real-space imaging of chain polymerization initiated by a scanning tunneling microscope tip*. Topics in Catalysis, **19**(2):187–192, 2002.
- [96] Y. Okawa and M. Aono. *Nanoscale wiring by controlled chain polymerization*. Surface Science, **514**(1-3):41–47, 2002.
- [97] M. Akai-Kasaya, K. Shimizu, Y. Watanabe, A. Saito, M. Aono and Y. Kuwahara. *Electronic structure of a polydiacetylene nanowire fabricated on highly ordered pyrolytic graphite*. Physical Review Letters, **91**(25), 2003. 255501.
- [98] K. Takami, J. Mizuno, M. Akai-Kasaya, A. Saito, M. Aono and Y. Kuwahara. *Conductivity measurement of polydiacetylene thin films by double-tip scanning tunneling microscopy*. Journal of Physical Chemistry B, **108**(42):16353–16356, 2004.
- [99] M. M. S. Abdel-Mottaleb, S. De Feyter, A. Gesquiere, M. Sieffert, M. Klapper, K. Mullen and F. C. De Schryver. *Photodimerization of cinnamate derivatives studied by STM*. Nano Letters, **1**(7):353–359, 2001.
- [100] Y. B. Zhao, D. M. Poirier, R. J. Pechman and J. H. Weaver. *Electron-Stimulated Polymerization of Solid C<sub>60</sub>*. Applied Physics Letters, **64**(5):577–579, 1994.
- [101] Y. Nakamura, Y. Mera and K. Maeda. *In situ scanning tunneling microscopic study of polymerization of C-60 clusters induced by electron injection from the probe tips*. Applied Physics Letters, **77**(18):2834–2836, 2000.
- [102] R. Nouchi, K. Masunari, T. Ohta, Y. Kubozono and Y. Iwasa. *Ring of C<sub>60</sub> polymers formed by electron or hole injection from a scanning tunneling microscope tip*. Physical Review Letters, **97**(19), 2006. 196101.
- [103] H. Sakaguchi, H. Matsumura and H. Gong. *Electrochemical epitaxial polymerization of single-molecular wires*. Nature Materials, **3**(8):551–557, 2004.
- [104] H. Sakaguchi, H. Matsumura, H. Gong and A. M. Abouelwafa. *Direct visualization of the formation of single-molecule conjugated copolymers*. Science, **310**(5750):1002–1006, 2005.
- [105] B. S. Swartzentruber, A. P. Smith and H. Jonsson. *Experimental and theoretical study of the rotation of Si Ad-dimers on the Si(100) surface*. Physical Review Letters, **77**(12):2518–2521, 1996.
- [106] L. J. Lauhon and W. Ho. *Single molecule thermal rotation and diffusion: Acetylene on Cu(001)*. Journal of Chemical Physics, **111**(13):5633–5636, 1999.
- [107] J. V. Barth. *Transport of adsorbates at metal surfaces: From thermal migration to hot precursors*. Surface Science Reports, **40**(3-5):75–149, 2000.
- [108] Z. Y. Zhang and M. G. Lagally. *Atomistic processes in the early stages of thin-film growth*. Science, **276**(5311):377–383, 1997.
- [109] A. Zangwill. *Physics at surfaces*. Cambridge University Press, 1988.
- [110] S. Arrhenius. *Über die Reaktionsgeschwindigkeit bei der Inversion von Rohrzucker durch Säuren*. Zeitschrift fuer Physikalische Chemie, **4**:226, 1889.
- [111] T. R. Linderoth, S. Hørch, E. Lægsgaard, I. Stensgaard and F. Besenbacher. *Surface Diffusion of Pt on Pt(110): Arrhenius Behavior of Long Jumps*. Physical Review Letters, **78**:4978–4981, 1997.
- [112] T. R. Linderoth, S. Hørch, L. Petersen, S. Helveg, E. Lægsgaard, I. Stensgaard and F. Besenbacher. *Novel mechanism for diffusion of one-dimensional clusters: Pt/Pt(110) – (1 × 2)*. Physical Review Letters, **82**(7):1494–1497, 1999.
- [113] M. Schunack, T. R. Linderoth, F. Rosei, E. Lægsgaard, I. Stensgaard and F. Besenbacher. *Long Jumps in the Surface Diffusion of Large Molecules*. Physical Review Letters, **88**:156102, 2002.
- [114] R. Otero, F. Hümmelink, F. Sato, S. B. Legoas, P. Thosttrup, E. Lægsgaard, I. Stensgaard, D. S. Galvao and F. Besenbacher. *Lock-and-key effect in the surface diffusion of large organic molecules probed by STM*. Nature Materials, **3**(11):779–782, 2004.
- [115] H. Yanagi, H. Mukai, K. Ikuta, T. Shibutani, T. Kamikado, S. Yokoyama and S. Mashiko. *Molecularly resolved dynamics for two-dimensional nucleation of supramolecular assembly*. Nano Letters, **2**(6):601–604, 2002.



- [116] S. Berner, M. Brunner, L. Ramoino, H. Suzuki, H. J. Güntherodt and T. A. Jung. *Time evolution analysis of a 2D solid-gas equilibrium: a model system for molecular adsorption and diffusion*. Chemical Physics Letters, **348**(3-4):175–181, 2001.
- [117] J. C. Dunphy, M. Rose, S. Behler, D. F. Ogletree, M. Salmeron and P. Sautet. *Acetylene structure and dynamics on Pd(111)*. Physical Review B, **57**(20):R12705–R12708, 1998.
- [118] J. Weckesser, J. V. Barth and K. Kern. *Direct observation of surface diffusion of large organic molecules at metal surfaces: PVBA on Pd(110)*. Journal of Chemical Physics, **110**(11):5351–5354, 1999.
- [119] J. Weckesser, J. V. Barth and K. Kern. *Mobility and bonding transition of C<sub>60</sub> on Pd(110)*. Physical Review B, **64**(16):art. no.–161403, 2001. 161403.
- [120] Y. Shirai, A. J. Osgood, Y. M. Zhao, K. F. Kelly and J. M. Tour. *Directional control in thermally driven single-molecule nanocars*. Nano Letters, **5**(11):2330–2334, 2005.
- [121] J. K. Gimzewski, C. Joachim, R. R. Schlittler, V. Langlais, H. Tang and I. Johannsen. *Rotation of a Single Molecule Within a Supramolecular Bearing*. Science, **281**:531–533, 1998.
- [122] M. Stöhr, T. Wagner, M. Gabriel, B. Weyers and R. Möller. *Direct observation of hindered eccentric rotation of an individual molecule: Cu-phthalocyanine on C<sub>60</sub>*. Physical Review B, **65**(3):033404, 2001.
- [123] M. Fendrich, T. Wagner, M. Stöhr and R. Möller. *Hindered rotation of a copper phthalocyanine molecule on C<sub>60</sub>: Experiments and molecular mechanics calculations*. Physical Review B, **73**(11), 2006. 115433.
- [124] M. Wahl, M. Stohr, H. Spillmann, T. A. Jung and L. H. Gade. *Rotation-libration in a hierarchic supramolecular rotor-stator system: Arrhenius activation and retardation by local interaction*. Chemical Communications, (13):1349–1351, 2007.
- [125] H. Yanagi, K. Ikuta, H. Mukai and T. Shibusani. *STM-induced flip-flop switching of adsorbed subphthalocyanine molecular arrays*. Nano Letters, **2**(9):951–955, 2002.
- [126] B. C. Stipe, M. A. Rezaei and W. Ho. *Coupling of vibrational excitation to the rotational motion of a single adsorbed molecule*. Physical Review Letters, **81**(6):1263–1266, 1998.
- [127] F. Chiaravalloti, L. Gross, K. H. Rieder, S. M. Stojkovic, A. Gourdon, C. Joachim and F. Moresco. *A rack-and-pinion device at the molecular scale*. Nature Materials, **6**(1):30–33, 2007.
- [128] T. A. Jung, R. R. Schlittler and J. K. Gimzewski. *Conformational identification of individual adsorbed molecules with the STM*. Nature, **386**(6626):696–698, 1997.
- [129] H. Suzuki, H. Miki, S. Yokoyama and S. Mashiko. *Identifying subphthalocyanine molecule isomers by using a scanning tunneling microscope*. Journal of Physical Chemistry B, **107**(15):3659–3662, 2003.
- [130] F. Moresco, G. Meyer, K.-H. Rieder, H. Tang, A. Gourdon and C. Joachim. *Conformational Changes of Single Molecules Induced by Scanning Tunneling Microscopy Manipulation: A Route to Molecular Switching*. Physical Review Letters, **86**(4):672–675, 2001.
- [131] C. Loppacher, M. Guggisberg, O. Pfeiffer, E. Meyer, M. Bammerlin, R. Lüthi, R. Schlittler, J. K. Gimzewski, H. Tang and C. Joachim. *Direct Determination of the Energy Required to Operate a Single Molecule Switch*. Physical Review Letters, **90**(6):066107, 2003.
- [132] X. H. Qiu, G. V. Nazin and W. Ho. *Mechanisms of reversible conformational transitions in a single molecule*. Physical Review Letters, **93**(19), 2004. 196806.
- [133] J. Henzl, M. Mehlhorn, H. Gawronski, K. H. Rieder and K. Morgenstern. *Reversible cis-trans isomerization of a single azobenzene molecule*. Angewandte Chemie-International Edition, **45**(4):603–606, 2006.
- [134] M. Alemani, M. V. Peters, S. Hecht, K. H. Rieder, F. Moresco and L. Grill. *Electric field-induced isomerization of azobenzene by STM*. Journal of the American Chemical Society, **128**(45):14446–14447, 2006.
- [135] B. Y. Choi, S. J. Kahng, S. Kim, H. Kim, H. W. Kim, Y. J. Song, J. Ihm and Y. Kuk. *Conformational molecular switch of the azobenzene molecule: A scanning tunneling microscopy study*. Physical Review Letters, **96**(15), 2006. 156106.

- [136] L. Grill, K. H. Rieder, F. Moresco, G. Rapenne, S. Stojkovic, X. Bouju and C. Joachim. *Rolling a single molecular wheel at the atomic scale*. Nature Nanotechnology, **2**(2):95–98, 2007.
- [137] M. Schunack, F. Rosei, Y. Naitoh, P. Jiang, A. Gourdon, E. Lægsgaard, I. Stensgaard, C. Joachim and F. Besenbacher. *Adsorption behavior of Lander molecules on Cu(110) studied by scanning tunneling microscopy*. Journal of Chemical Physics, **117**(13):6259–6265, 2002.
- [138] D. Bonifazi, H. Spillmann, A. Kiebele, M. de Wild, P. Seiler, F. Y. Cheng, H. J. Guntherodt, T. Jung and F. Diederich. *Supramolecular patterned surfaces driven by cooperative assembly of C<sub>60</sub> and porphyrins on metal substrates*. Angewandte Chemie-International Edition, **43**(36):4759–4763, 2004.
- [139] G. Binnig, H. Rohrer, C. Gerber and E. Weibel. *Surface Studies by Scanning Tunneling Microscopy*. Physical Review Letters, **49**(1):57–61, 1982.
- [140] F. Besenbacher. *Scanning tunnelling microscopy studies of metal surfaces*. Reports on Progress in Physics, **59**(12):1737–1802, 1996.
- [141] C. J. Chen. *Introduction to Scanning Tunneling Microscopy*. Oxford University Press, 2. edition, 2007.
- [142] J. Tersoff and D. R. Hamann. *Theory and Application for the Scanning Tunneling Microscope*. Physical Review Letters, **50**(25):1998–2001, 1983.
- [143] J. Tersoff and D. R. Hamann. *Theory of the Scanning Tunneling Microscope*. Physical Review B, **31**(2):805–813, 1985.
- [144] J. Bardeen. *Tunnelling from a Many-Particle Point of View*. Physical Review Letters, **6**(2):57–59, 1961.
- [145] N. D. Lang. *Theory of Single-Atom Imaging in the Scanning Tunneling Microscope*. Physical Review Letters, **56**(11):1164–1167, 1986.
- [146] B. Hammer and J. K. Nørskov. *Theoretical surface science and catalysis - Calculations and concepts*. Advances in Catalysis, **45**:71–129, 2000.
- [147] P. H. Lippel, R. J. Wilson, M. D. Miller, C. Wöll and S. Chiang. *High-Resolution Imaging of Copper-Phthalocyanine by Scanning-Tunneling Microscopy*. Physical Review Letters, **62**(2):171–174, 1989.
- [148] R. Strohmaier, J. Petersen, B. Gompf and W. Eisenmenger. *A systematic STM study of planar aromatic molecules on inorganic substrates - I. Submolecular image contrast*. Surface Science, **418**(1):91–104, 1998.
- [149] T. Hashizume, K. Motai, X. D. Wang, H. Shinohara, Y. Saito, Y. Maruyama, K. Ohno, Y. Kawazoe, Y. Nishina, H. W. Pickering, Y. Kuk and T. Sakurai. *Intramolecular Structures of C<sub>60</sub> Molecules Adsorbed on the Cu(111) – (1 × 1) Surface*. Physical Review Letters, **71**(18):2959–2962, 1993.
- [150] V. M. Hallmark and S. Chiang. *Predicting Stm Images of Molecular Adsorbates*. Surface Science, **329**(3):255–268, 1995.
- [151] H. Ouyang, R. A. Marcus and B. Kallebring. *Scanning-Tunneling-Microscopy Theory for an Adsorbate - Application to Adenine Adsorbed on a Graphite Surface*. Journal of Chemical Physics, **100**(10):7814–7824, 1994.
- [152] P. Sautet and C. Joachim. *Calculation of the Benzene on Rhodium Stm Images*. Chemical Physics Letters, **185**(1-2):23–30, 1991.
- [153] J. Repp, G. Meyer, S. M. Stojkovic, A. Gourdon and C. Joachim. *Molecules on insulating films: Scanning-tunneling microscopy imaging of individual molecular orbitals*. Physical Review Letters, **94**(2), 2005. 026803.
- [154] E. Lægsgaard. [www.phys.au.dk/spm/stminstru.shtm](http://www.phys.au.dk/spm/stminstru.shtm), 2007.
- [155] E. Lægsgaard, F. Besenbacher, K. Mortensen and I. Stensgaard. *A fully automated, ‘thimble-size’ scanning tunnelling microscope*. Journal of Microscopy, **152**(3):663–669, 1988. Paper only.
- [156] D. P. Woodruff and T. A. Delchar. *Modern techniques of surface science*. Cambridge University Press, 1. edition, 1986.
- [157] P. Hofmann. *Lecture Notes in Surface Science*. Århus University, 2.1 edition, 2002.
- [158] J. Schnadt. *Studies of Model Nanostructured Materials*. PhD thesis, Uppsala, 2002.



- [159] J. Stöhr. *NEXAFS Spectroscopy*. Springer-Verlag, 1992.
- [160] P. Hohenberg and W. Kohn. *Inhomogeneous Electron Gas*. Physical Review B, **136**(3B):B864–B871, 1964.
- [161] W. Kohn and L. J. Sham. *Self-Consistent Equations Including Exchange and Correlation Effects*. Physical Review, **140**(4A):1133–1138, 1965.
- [162] B. Hammer, L. B. Hansen and J. K. Nørskov. *Improved adsorption energetics within density-functional theory using revised Perdew-Burke-Ernzerhof functionals*. Physical Review B, **59**(11):7413–7421, 1999.
- [163] S. R. Bahn and K. W. Jacobsen. *An object-oriented scripting interface to a legacy electronic structure code*. Computing in Science and Engineering, **4**(3):56–66, 2002.
- [164] C. Zhang, M. H. Du, H. P. Cheng, X. G. Zhang, A. E. Roitberg and J. L. Krause. *Coherent electron transport through an azobenzene molecule: A light-driven molecular switch*. Physical Review Letters, **92**(15), 2004. 158301.
- [165] G. Zimmerman, L. Y. Chow and U. J. Paik. *The Photochemical Isomerization of Azobenzene*. Journal of the American Chemical Society, **80**(14):3528–3531, 1958.
- [166] J. Clayden, N. Greeves, S. Warren and P. Wothers. *Organic Chemistry*. Oxford University Press, 2001.
- [167] R. Micheletto, M. Yokokawa, M. Schroeder, D. Hobara, Y. Ding and T. Kakiuchi. *Real time observation of trans-cis isomerization on azobenzene SAM induced by optical near field enhancement*. Applied Surface Science, **228**(1-4):265–270, 2004.
- [168] T. Ikeda and O. Tsutsumi. *Optical Switching and Image Storage by Means of Azobenzene Liquid-Crystal Films*. Science, **268**(5219):1873–1875, 1995.
- [169] Z. F. Liu, K. Hashimoto and A. Fujishima. *Photoelectrochemical Information-Storage Using an Azobenzene Derivative*. Nature, **347**(6294):658–660, 1990.
- [170] A. Natansohn, P. Rochon, M. S. Ho and C. Barrett. *Azo Polymers for Reversible Optical Storage .6. Poly[4-[2-(Methacryloyloxy)Ethyl]Azobenzene]*. Macromolecules, **28**(12):4179–4183, 1995.
- [171] T. Ishikawa, T. Noro and T. Shoda. *Theoretical study on the photoisomerization of azobenzene*. Journal of Chemical Physics, **115**(16):7503–7512, 2001.
- [172] S. Monti, G. Orlandi and P. Palmieri. *Features of the Photochemically Active State Surfaces of Azobenzene*. Chemical Physics, **71**(1):87–99, 1982.
- [173] T. Hugel, N. B. Holland, A. Cattani, L. Moroder, M. Seitz and H. E. Gaub. *Single-Molecule Optomechanical Cycle*. Science, **296**:1103, 2002.
- [174] K. H. Jung, S. B. Jung, H. K. Shin, C. Kim and Y. S. Kwon. *Observation and electrical properties of functionalized dendrimer monolayers by using SPMs*. Synthetic Metals, **152**(1-3):285–288, 2005.
- [175] J. Fritz, O. Probst, S. Dey, S. Grafstrom, J. Kowalski and R. Neumann. *Scanning-Tunneling-Microscopy Studies of Diazo Dye Monolayers on HOPG*. Surface Science, **329**(3):L613–L618, 1995.
- [176] T. Umemoto, K. Ishikawa, H. Takezoe, A. Fukuda, T. Sasaki and T. Ikeda. *Photoisomerization Observed by Means of Scanning-Tunneling-Microscopy*. Japanese Journal of Applied Physics Part 2-Letters, **32**(7A):L936–L939, 1993.
- [177] P. Vanoppen, P. C. M. Grim, M. Rucker, S. DeFeyter, G. Mössner, S. Valiyaveetil, K. Mullen and F. C. DeSchryver. *Solvent codeposition and cis-trans isomerization of isophthalic acid derivatives studied by STM*. Journal of Physical Chemistry, **100**(50):19636–19641, 1996.
- [178] C. L. Feng, Y. J. Zhang, J. Jin, Y. L. Song, L. Y. Xie, G. R. Qu, L. Jiang and D. B. Zhu. *Completely interfacial photoisomerization of 4-hydroxy-3'-trifluoromethyl-azobenzene studied by STM on HOPG*. Surface Science, **513**(1):111–118, 2002.
- [179] L. P. Xu and L. J. Wan. *STM investigation of the photoisomerization of an azobis-(benzo-15-crown-5) molecule and its self-assembly on Au(111)*. Journal of Physical Chemistry B, **110**(7):3185–3188, 2006.
- [180] S. Yasuda, T. Nakamura, M. Matsumoto and H. Shigekawa. *Phase switching of a single isomeric molecule and associated characteristic rectification*. Journal of the American Chemical Society, **125**(52):16430–16433, 2003.

- [181] A. Kirakosian, M. J. Comstock, J. W. Cho and M. F. Crommie. *Molecular commensurability with a surface reconstruction: STM study of azobenzene on Au(111)*. Physical Review B, **71**(11), 2005. 113409.
- [182] M. J. Comstock, J. W. Cho, A. Kirakosian and M. F. Crommie. *Manipulation of azobenzene molecules on Au(111) using scanning tunneling microscopy*. Physical Review B, **72**(15), 2005. 153414.
- [183] M. Schunack. *Scanning Tunneling Microscopy Studies of Organic Molecules on Metal Surfaces*. PhD thesis, University of Aarhus, 2002.
- [184] P. Atkins and J. de Paula. *Atkins' physical chemistry*. Oxford University Press, 7 edition, 2002.
- [185] F. Rosei, M. Schunack, P. Jiang, A. Gourdon, E. Lægsgaard, I. Stensgaard, C. Joachim and F. Besenbacher. *Organic Molecules Acting as Templates on Metal Surfaces*. Science, **296**(5566):328–331, 2002.
- [186] Z. J. Donhauser, B. A. Mantooth, K. F. Kelly, L. A. Bumm, J. D. Monnell, J. J. Stapleton, D. W. Price, A. M. Rawlett, D. L. Allara, J. M. Tour and P. S. Weiss. *Conductance switching in single molecules through conformational changes*. Science, **292**(5525):2303–2307, 2001.
- [187] J. Reichert, R. Ochs, D. Beckmann, H. B. Weber, M. Mayor and H. v. Löhneysen. *Driving Current through Single Organic Molecules*. Physical Review Letters, **88**(17):176804, 2002.
- [188] J. Chen, M. A. Reed, A. M. Rawlett and J. M. Tour. *Large On-Off Ratios and Negative Differential Resistance in a Molecular Electronic Device*. Science, **286**(5444):1550–1552, 1999.
- [189] L. A. Bumm, J. J. Arnold, M. T. Cygan, T. D. Dunbar, T. P. Burgin, L. Jones, D. L. Allara, J. M. Tour and P. S. Weiss. *Are single molecular wires conducting?* Science, **271**(5256):1705–1707, 1996.
- [190] P. Samori, V. Francke, V. Enkelmann, K. Mullen and J. P. Rabe. *Synthesis and Solid State Structures of Functionalized Phenyleneethynylene Trimers in 2D and 3D*. Chemical Materials, **15**(5):1032–1039, 2003.
- [191] Z. C. Mu, X. Y. Yang, Z. Q. Wang and X. Zhang. *Influence of substituents on two-dimensional ordering of oligo(phenylene-ethynylene)s - A scanning tunneling microscopy study*. Langmuir, **20**(20):8892–8896, 2004.
- [192] K. V. Gothelf, R. S. Brown, A. Thomsen and M. Nielsen, 2004.
- [193] M. Nielsen, A. H. Thomsen, T. R. Jensen, H. J. Jakobsen, J. Skibsted and K. V. Gothelf. *Formation and structure of conjugated salen-cross-linked polymers and their application in asymmetric heterogeneous catalysis*. European Journal of Organic Chemistry, (2):342–347, 2005.
- [194] K. V. Gothelf, A. Thomsen, M. Nielsen, E. Clo and R. S. Brown. *Modular DNA-programmed assembly of linear and branched conjugated nanostructures*. Journal of the American Chemical Society, **126**(4):1044–1046, 2004.
- [195] M. Nielsen, A. H. Thomsen, E. Clo, F. Kirpekar and K. V. Gothelf. *Synthesis of linear and tripoidal oligo(phenylene ethynylene)-based building blocks for application in modular DNA-programmed assembly*. Journal of Organic Chemistry, **69**(7):2240–2250, 2004.
- [196] S. Weigelt, C. Busse, C. Bombis, M. M. Knudsen, K. V. Gothelf, T. Strunskus, C. Wöll, M. Dahlbom, B. Hammer, E. Lægsgaard, F. Besenbacher and T. R. Linderoth. *Covalently bound molecular nanostructures by organic chemistry in two dimensions*. Submitted.
- [197] J. V. Barth, H. Brune, G. Ertl and R. J. Behm. *Scanning Tunneling Microscopy Observations on the Reconstructed Au(111) Surface - Atomic-Structure, Long-Range Superstructure, Rotational Domains, and Surface-Defects*. Physical Review B, **42**(15):9307–9318, 1990.
- [198] R. J. Needs, M. J. Godfrey and M. Mansfield. *Theory of Surface Stress and Surface Reconstruction*. Surface Science, **242**(1-3):215–221, 1991.
- [199] H. Suzuki, H. Miki, S. Yokoyama and S. Mashiko. *Segregation of molecular overlayers with different structures on a metal surface*. Thin Solid Films, **438**:97–100, 2003.
- [200] C. Bombis, S. Weigelt, C. Busse, M. Nørgaard, M. M. Knudsen, K. V. Gothelf, E. Rauls, B. Hammer, F. Besenbacher and T. R. Linderoth. *Molecular nanostructures formed by a class of oligo-phenylene-ethynylenes with systematic variation of chemical endgroups*. In manuscript, 2007.

- [201] T. Frauenheim, G. Seifert, M. Elstner, Z. Hajnal, G. Jungnickel, D. Porezag, S. Suhai and R. Scholz. *A self-consistent charge density-functional based tight-binding method for predictive materials simulations in physics, chemistry and biology*. Physica Status Solidi B-Basic Research, **217**(1):41–62, 2000.
- [202] S. Lukas, G. Witte and C. Wöll. *Novel mechanism for molecular self-assembly on metal substrates: Unidirectional rows of pentacene on Cu(110) produced by a substrate-mediated repulsion*. Physical Review Letters, **88**(2), 2002. 028301.
- [203] T. Ishida, W. Mizutani, U. Akiba, K. Umemura, A. Inoue, N. Choi, M. Fujihira and H. Tokumoto. *Lateral electrical conduction in organic monolayer*. Journal of Physical Chemistry B, **103**(10):1686–1690, 1999.
- [204] M. Pickholtz and S. Stafstrom. *Theoretical investigation of the role of pi-pi interactions for the stability of phenylene ethynylene aggregates*. Chemical Physics, **270**(2):245–251, 2001.
- [205] C. A. Hunter, K. R. Lawson, J. Perkins and C. J. Urch. *Aromatic interactions*. Journal of the Chemical Society-Perkin Transactions 2, (5):651–669, 2001.
- [206] J. C. Nelson, J. G. Saven, J. S. Moore and P. G. Wolynes. *Solvophobicity driven folding of nonbiological oligomers*. Science, **277**(5333):1793–1796, 1997.
- [207] P. R. Davies and J. M. Keel. *The reaction of carbon dioxide with amines at a Cu(211) surface*. Surface Science, **469**(2-3):204–213, 2000.
- [208] Y. F. Y. Yao. *Chemisorption of Amines and Its Effect on Subsequent Oxidation of Iron Surfaces*. Journal of Physical Chemistry, **68**(1):101–105, 1964.
- [209] J. J. Chen and N. Winograd. *The Adsorption and Decomposition of Methylamine on Pd(111)*. Surface Science, **326**(3):285–300, 1995.
- [210] S. Y. Hwang, E. G. Seebauer and L. D. Schmidt. *Decomposition of CH<sub>3</sub>NH<sub>2</sub> on Pt(111)*. Surface Science, **188**(1-2):219–234, 1987.
- [211] P. A. Thomas and R. I. Masel. *Summary Abstract: Methylamine adsorption and decomposition on (5 × 20) and (1 × 1) Pt(100)*. Journal of Vacuum Science and Technology A: Vacuum, Surfaces, and Films, **5**(4):1106–1108, 1987.
- [212] I. Chorkendorff, J. N. Russell and J. T. Yates. *Surface-Reaction Pathways of Methylamine on the Ni(111) Surface*. Journal of Chemical Physics, **86**(8):4692–4700, 1987.
- [213] F. Maseri, A. Peremans, J. Darville and J. M. Gilles. *An IRAS/TDS study of the adsorption of CH<sub>3</sub>NH<sub>2</sub> on Cu(110)*. Journal of Electron Spectroscopy and Related Phenomena, **54-55**:1059–1064, 1990.
- [214] P. R. Davies and J. M. Keel. *Intermolecular migration of methyl groups at a Cu(211) surface*. Catalysis Letters, **58**(2-3):99–102, 1999.
- [215] A. G. Baca, M. A. Schulz and D. A. Shirley. *Electron-Energy Loss Spectroscopy (EELS) of CH<sub>3</sub>NH<sub>2</sub> Adsorbed on Ni(100), Ni(111), Cr(100), and Cr(111)*. Journal of Chemical Physics, **83**(11):6001–6008, 1985.
- [216] D. H. Kang, B. Chatterjee, E. Hecceg and M. Trenary. *Adsorption and decomposition of trimethylamine on Pt(111): formation of dimethylaminocarbyne (CN(CH<sub>3</sub>)<sub>2</sub>)*. Surface Science, **540**(1):23–38, 2003.
- [217] X. Cao and R. J. Hamers. *Molecular and dissociative bonding of amines with the Si(111) – (7 × 7) surface*. Surface Science, **523**(3):241–251, 2003.
- [218] B. J. Eves, C. Fan and G. P. Lopinski. *Sequential reactions with amine-terminated monolayers and isolated molecules on H/Si(111)*. Small, **2**(11):1379–84, 2006.
- [219] C. L. Claypool, F. Faglioni, W. A. Goddard, H. B. Gray, N. S. Lewis and R. A. Marcus. *Source of image contrast in STM images of functionalized alkanes on graphite: A systematic functional group approach*. Journal of Physical Chemistry B, **101**(31):5978–5995, 1997.
- [220] S. M. Wetterer, D. J. Lavrich, T. Cummings, S. L. Bernasek and G. Scoles. *Energetics and kinetics of the physisorption of hydrocarbons on Au(111)*. Journal of Physical Chemistry B, **102**(46):9266–9275, 1998.

- [221] H. M. Zhang, Z. X. Xie, B. W. Mao and X. Xu. *Self-assembly of normal alkanes on the Au(111) surfaces*. Chemistry-a European Journal, **10**(6):1415–1422, 2004.
- [222] H. M. Zhang, J. W. Yan, Z. X. Xie, B. W. Mao and X. Xu. *Self-assembly of alkanols on Au(111) surfaces*. Chemistry-a European Journal, **12**(15):4006–4013, 2006.
- [223] H. Kondoh, C. Kodama, H. Sumida and H. Nozoye. *Molecular processes of adsorption and desorption of alkanethiol monolayers on Au(111)*. Journal of Chemical Physics, **111**(3):1175–1184, 1999.
- [224] G. A. Jeffrey. *An introduction to hydrogen bonding*. Oxford University Press, New York, 1997.
- [225] K. Weiss, J. Weckesser and C. Wöll. *An X-ray absorption study of saturated hydrocarbons physisorbed on metal surfaces*. Journal of Molecular Structure-Theochem, **458**(1-2):143–150, 1999.
- [226] R. N. S. Sodhi and C. E. Brion. *Inner Shell Electron-Energy Loss Spectra of the Methyl Amines and Ammonia*. Journal of Electron Spectroscopy and Related Phenomena, **36**(2):187–201, 1985.
- [227] J. Li, R. F. Li and G. C. Wang. *A systematic density functional theory study of the C-N bond cleavage of methylamine on metals*. Journal of Physical Chemistry B, **110**(29):14300–14303, 2006.
- [228] E. H. Cordes and W. P. Jencks. *On Mechanism of Schiff Base Formation and Hydrolysis*. Journal of the American Chemical Society, **84**(5):832, 1962.
- [229] J. M. Berg, J. L. Tymoczko and L. Stryer. *Biochemistry*. W. H. Freeman and Company, 5 edition, 2002.
- [230] M. Grigoras and C. O. Catanescu. *Imine Oligomers and Polymers*. Polymer Reviews, **44**(2):131 – 173, 2004.
- [231] S. J. Cantrill, S. J. Rowan and J. F. Stoddart. *Rotaxane formation under thermodynamic control*. Organic Letters, **1**(9):1363–1366, 1999.
- [232] C. D. Pentecost, A. J. Peters, K. S. Chichak, G. W. V. Cave, S. J. Cantrill and J. F. Stoddart. *Chiral borromeates*. Angewandte Chemie-International Edition, **45**(25):4099–4104, 2006.
- [233] X. D. Wang, K. Ogino, K. Tanaka and H. Usui. *Novel polyimine as electroluminescent material prepared by vapor deposition polymerization*. Thin Solid Films, **438**:75–79, 2003.
- [234] A. B. Sherrill, V. S. Lusvardi, J. Eng, J. G. G. Chen and M. A. Barteau. *NEXAFS investigation of benzaldehyde reductive coupling to form stilbene on reduced surfaces of TiO<sub>2</sub>(001)*. Catalysis Today, **63**(1):43–51, 2000.
- [235] A. G. Shard, J. D. Whittle, A. J. Beck, P. N. Brookes, N. A. Bullett, R. A. Talib, A. Mistry, D. Barton and S. L. McArthur. *A NEXAFS examination of unsaturation in plasma polymers of allylamine and propylamine*. Journal of Physical Chemistry B, **108**(33):12472–12480, 2004.
- [236] N. E. Hall and B. J. Smith. *High-level ab initio molecular orbital calculations of imine formation*. Journal of Physical Chemistry A, **102**(25):4930–4938, 1998.
- [237] Y. H. Mariam and L. Chantranupong. *DFT computational studies of intramolecular hydrogen-bonding interactions in a model system for 5-iminodaunomycin*. Journal of Molecular Structure-Theochem, **529**:83–97, 2000.
- [238] R. A. L. Jones. *Soft Condensed Matter*. 1. edition, 2002.
- [239] Z. B. Guan, P. M. Cotts, E. F. McCord and S. J. McLain. *Chain walking: A new strategy to control polymer topology*. Science, **283**(5410):2059–2062, 1999.
- [240] K. Sugiura, H. Tanaka, T. Matsumoto, T. Kawai and Y. Sakata. *A Mandala-patterned Bandanna-shaped porphyrin oligomer, C<sub>1244</sub>H<sub>1350</sub>N<sub>84</sub>Ni<sub>20</sub>O<sub>88</sub>, having a unique size and geometry*. Chemistry Letters, (11):1193–1194, 1999.
- [241] H. Kasai, H. Tanaka, S. Okada, H. Oikawa, T. Kawai and H. Nakanishi. *STM observation of single molecular chains of pi-conjugated polymers*. Chemistry Letters, (7):696–697, 2002.
- [242] H. Tanaka and T. Kawai. *Visualization of detailed structures within DNA*. Surface Science, **539**(1-3):L531–L536, 2003.
- [243] N. Aratani, A. Takagi, Y. Yanagawa, T. Matsumoto, T. Kawai, Z. S. Yoon, D. Kim and A. Osuka. *Giant meso-meso-linked porphyrin arrays of micrometer molecular length and their fabrication*. Chemistry-a European Journal, **11**(11):3389–3404, 2005.

- [244] N. Bampos, C. N. Woodburn, M. E. Welland and J. K. M. Sanders. *STM images of individual porphyrin molecules on Cu(100) and Cu(111) surfaces*. *Angewandte Chemie-International Edition*, **38**(18):2780–2783, 1999.
- [245] P. Samori, V. Francke, K. Mullen and J. P. Rabe. *Self-assembly of a conjugated polymer: from molecular rods to a nanoribbon architecture with molecular dimensions*. *Chemistry - a European Journal*, **5**(8):2312–2317, 1999.
- [246] E. Mena-Osteritz, A. Meyer, B. M. W. Langeveld-Voss, R. A. J. Janssen, E. W. Meijer and P. Bauerle. *Two-dimensional crystals of poly(3-alkylthiophene)s: Direct visualization of polymer folds in sub-molecular resolution*. *Angewandte Chemie-International Edition*, **39**(15):2680–2684, 2000.
- [247] M. Brun, R. Demadrille, P. Rannou, A. Pron, J. P. Travers and B. Grevin. *Multiscale scanning Tunneling Microscopy Study of self-assembly phenomena in two-dimensional polycrystals of pi-conjugated polymers: The case of regioregular poly (dioctylbithiophene-alt-fluore-none)*. *Advanced Materials*, **16**(23-24):2087, 2004.
- [248] L. Scifo, M. Dubois, M. Brun, P. Rannou, S. Latil, A. Rubio and B. Grevin. *Probing the electronic properties of self-organized poly(3-dodecylthiophene) monolayers by two-dimensional scanning tunneling spectroscopy imaging at the single chain scale*. *Nano Letters*, **6**(8):1711–1718, 2006.
- [249] E. Kasemi, W. Zhuang, J. P. Rabe, K. Fischer, M. Schmidt, M. Colussi, H. Keul, D. Yi, H. Colfen and A. D. Schluter. *Synthesis of an anionically chargeable, high-molar-mass, second-generation dendronized polymer and the observation of branching by scanning force microscopy*. *Journal of the American Chemical Society*, **128**(15):5091–5099, 2006.
- [250] A. Götzhauser, S. Panov, M. Mast, A. Schertel, M. Grünze and C. Wöll. *Growth of Pyromellitic Dianhydride on an Amino-Terminated Surface*. *Surface Science*, **334**(1-3):235–247, 1995.
- [251] P. Flory. *Molecular Size Distribution in Three Dimensional Polymers. I. Geletation*. *Journal of the American Chemical Society*, **63**:3083–3090, 1941.
- [252] P. Flory. *Molecular Size Distribution in Three Dimensional Polymers. II. Trifunctional Branching Units*. *Journal of the American Chemical Society*, **63**:3091–3096, 1941.
- [253] P. Flory. *Molecular Size Distribution in Three Dimensional Polymers. III. Trifunctional Branching Units*. *Journal of the American Chemical Society*, **63**:3096–3100, 1941.
- [254] W. H. Stockmayer. *Theory of Molecular Size Distribution and Gel Formation in Branched-Chain Polymers*. *The Journal of Chemical Physics*, **11**:45–55, 1943.



---

## Acknowledgements

---

During my PhD I had the great pleasure of collaborating with a large number of people from chemistry, surface science, and theoretical physics. It is my great privilege to thank all the warm and brilliant people who have been helpful throughout my PhD studies.

First and foremost, I would like to thank my supervisors Flemming Besenbacher and Trolle R. Linderoth. Trolle R. Linderoth has provided invaluable help and support during most of my time as a PhD student. I would especially like to thank Trolle R. Linderoth for extended discussions of experiments and results and for teaching me how to set the highest standards in drafting papers and communication of scientific results. Flemming Besenbacher maintained view of the greater picture and provided career guidance. Erik Lægsgaard is deeply appreciated for his expert technical support in the laboratory.

In my early days as a new PhD student, I had the great benefit of experimental training by Lars Petersen, Roberto Otero and Carsten Busse. Later on Christian Bombis joined the group. In addition to acknowledge Carsten Busse and Christian Bombis for their extensive contribution to parts of the work presented in this thesis, I wish to thank them both for their patience and friendship. In 2005 the group was visited by Jill A. Miwa with whom I had the great pleasure to collaborate on the azobenzene project. Furthermore, I would like to thank Carsten Busse and Joachim Schnadt without whom the spectroscopic results would not have been achievable. The contributions of Henkjan Gersen, Thomas Strunskus, Anders K. Tuxen, Rasmus Havelund, Nataliya Kalashnyk, Federico Masini, Cristina Isvoranu, and Evren Ataman are also acknowledged.

The interdisciplinary works presented in this thesis was made possible through the close collaboration with members of Kurt V. Gothelf's synthesis group at the Department of Chemistry. I would especially like to acknowledge Kurt V. Gothelf, Morten Nielsen and Martin M. Knudsen for many fruitful discussions and knowledge transfer. The theoretical calculations presented are owed to collaboration with Bjørk Hammer, Eva Rauls and Mats Dahlbom at the Department of Physics. Their contribution is greatly appreciated. Finally, I would like to thank Mona, Jesper, Martin, Georg, Mads, Kristian, Anne Gry and Liv without whom my PhD years would have been less happy, and Jeanette Dandanell and Annette G. Riisberg for proof reading the thesis.